Efficient Zonal Method Based Comprehensive Modeling and Real-Time Simulation of More Electric Aircraft

by

Zhen Huang

A thesis submitted in partial fulfillment of the requirements for the degree of

Doctor of Philosophy
in
Energy Systems

Department of Electrical and Computer Engineering
University of Alberta

©Zhen Huang, 2020

Abstract

More electric aircraft (MEA) is deemed as next generation aircraft to help simplify system structure, improve reliability and save fuel. A comprehensive real-time simulation model of MEA can benefit the on-going development of the involved technology, and thus is of significance for MEA researchers and designers. The complete MEA model is a high-complexity system and contains multi-domain (electrical, pneumatic, hydraulic, and mechanical) components, which makes it very challenging for analyzing. Therefore, some special modeling techniques and computational strategies have to be created to simplify the solution process.

This thesis aims at realizing comprehensive modeling and real-time simulation of MEA by utilization of the efficient zonal method (EZM). Thus the accomplished works can be mainly divided into two parts: the design of EZM modeling methodology and the construction of the real-time MEA model.

The EZM is originated by an attempt to model nonlinearities, especially the switching transients, in power electronic circuit simulation. It is further found that the voltage/current relation of a circuit can be expressed in an antisymmetric matrix form. The proving process of this feature is provided and summarized into a circuit lemma. This feature is the foundation of EZM as it provides a way to find current relation through manipulation of voltage relation, a far less difficult task to accomplish.

Based on this feature, the EZM modeling methodology for circuit simulation is designed where the computation is divided into two interleaved processes: advancing system variables according to components' characteristics and taking into acount the network response. In this way, the processing of components' characteristics and circuit topology are decoupled and can be dealt with separately.

The resulting computational complexity reduces to nearly linear with the circuit scale—a significant reduction compared with traditional modeling methods.

The comprehensive MEA model was then constructed based on the modeling methodology of EZM. The Boeing®-787 on board power system is selected as the framework where various components including the pneumatic, hydraulic and mechanical modules are modeled and integrated into the system. Due to the fact that EZM can be viewed as the application of explicit numerical integration methods for solving circuit differential equations and explicit methods usually have relatively small numerical stability regions, the eigenvalue distribution of the assembled system is also analyzed for time-step selection scheme.

The constructed MEA model was emulated on field programmable gate array (FPGA) and high fidelity real-time simulation was realized. Emulation results from FPGA board and commercial software under several test scenarios coincide with each other to a very high degree, which showcases the efficacy of EZM with respect to computational efficiency and ability to accommodate multi-domain models. High agreement on transients waveforms suggests that this EZM based comprehensive MEA model could be a helpful tool for the modeling and design of MEA power system. The proposed circuit lemma and the corresponding EZM are even worth being promoted to model other complex systems that contain large-scale circuit.

Preface

The contents of this thesis is based on original work by Zhen Huang. As detailed below, material from some chapters of the thesis has been published as journal articles under the supervision of Dr. Venkata Dinavahi in concept formation and by providing comments and corrections to the article manuscript.

Chapter 2 includes contents that are published in the following paper:

- Z. Huang and V. Dinavahi, "A fast and stable method for modeling generalized nonlinearities in power electronic circuit simulation and its real-time implementation," *IEEE Trans. Power Electron.*, vol. 34, no. 4, pp. 3124-3138, April 2019.

Chapter 3 contains contents from the following papers:

- Z. Huang and V. Dinavahi, "An efficient hierarchical zonal method for large-scale circuit simulation and its real-time application on more electric aircraft microgrid," *IEEE Trans. Ind. Electron.*, vol. 66, no. 7, pp. 5778-5786, July 2019.
- Z. Huang, C. Tang, and V. Dinavahi, "Unified solver based real-time multi-domain simulation of aircraft electro-mechanical-actuator," *IEEE Trans. Energy Convers.,*, vol. 34, no. 4, pp. 2148-2157, Dec. 2019.

Chapter 4 is based on the following paper that is currently under peer review:

- Z. Huang, R. Zhu, C. Tang, and V. Dinavahi, "A fast time-step selection method for explicit solver based simulation of high frequency low loss circuit and its application on EMI filter", *submitted to IEEE Trans. Power Electron., under review.*

Chapter 5 contains contents from the following paper:

- Z. Huang, T. Duan, C. Tang, and V. Dinavahi, "Modular assembly and real-time hardware emulation of on-the-move multi-domain multi-machine system on more electric aircraft", *accepted by IEEE Trans. Ind. Electron., in publication process.*

To my mother

for your unconditional love
and to my wife and sister
who always supports me.

Acknowledgements

I would like to express my sincere appreciation to my supervisor *Prof. Venkata Dinavahi* for his support, encouragement, and inspiring guidance through my study at the University of Alberta. His passion towards research is a tremendous impetus to me.

In the meantime, I wish to deliver thanks to members of the RTX-Lab, who worked together with me and helped me during my research. I feel so warmed to be here and work with these nice persons. Peng Liu, Ruimin Zhu, Zhuoxuan Shen, Tong Duan, Ning Lin, Tian Liang, these names mean a lot to me. We are not only colleagues, but become very good friends during my stay in this lab.

Many thanks to my friends and former colleagues, for providing me with the latest industrial information in this domain, and the support whenever I need it.

I want to express my gratitude to my mother as it is beyond any descriptive words, and towards my wife and sister, for the greatest support and encouragement during the hard times.

Table of Contents

List of Tables

List of Figures

List of Acronyms

AC	Alternating Current
ACM	Air Cycle Machine
APU	Auxiliary Power Unit
ATRU	Auto Transformer Rectifier Unit
DAE	Differential Algebraic Equation
DAC	Digital-to-Analog Converter
DC	Direct Current
E-ECS	Electrially-driven Environmental Control System
EHSA	Electro-Hydrostatic Actuator
EMA	Electro-Mechanical Actuator
EMI	Electromagnetic interference
EMT	Electromagnetic transient
EZM	Efficient Zonal Method
FPGA	Field Programmable Gate Array
GPU	Graphics Processing Unit
HFLL	High Frequency Low Loss
HIL	Hardware-in-the-loop
HVDC	High-voltage Direct Current
IGBT	Insulated-Gate Bipolar Transistor
KCL	Kirchhoff's Current Law
KVL	Kirchhoff's Voltage Law
LIM	Latency Insertion Method
LPTN	Lumped Parameter Thermal Network
LPV	Linear Parameter Varying
LTE	Local Error Truncation
LUT	Look-Up Table
MEA	More Electric Aircraft
MMC	Modular Multi-level Converter
NPC	Neutral Point Clamped
PBW	Power-by-Wire
PI	Proportional Integral
PMSM	Permanent Magnet Synchronous Machine
RK4	4th-order Runge Kutta
SG	Synchronous Generator

SM	Submodule
SVPWM	Space Vector Pulse Width Modulation
TLM	Transmission Line Modeling
TR	Trapezoidal Rule
VHDL	Very-high-speed-integrated-circuit
WIPS	Wing Ice Protection System

1 Introduction

1.1 Research Background

More electric aircraft has become the consensus in both industry and academia as next generation aviation technology since this concept first arose in the 1990s. The MEA concept means using electric systems in applications that have traditionally been powered by hydraulic, mechanical, or pneumatic power [1]. The wide-use of versatile electric energy makes next-generation aircraft to be quieter, more fuel efficient and maintenance easier. A comprehensive real-time simulation model of MEA can benefit for the on-going development of the involved technology, thus is of significance for MEA researchers and designers. However, modeling and simulation, especially real-time hardware simulation of the power system on more electric aircraft poses challenge to most state-of-the-art simulation tools and theories due to its high complexity and computational burden.

This section reviews the state-of-the-art of more electric aircraft and circuit modeling methods.

1.1.1 State-of-the-Art of More Electrical Aircraft

An aircraft typically needs four types of power in operation, i.e. pneumatic, hydraulic, mechanical and electrical power, as shown in Fig. 1.1. Pneumatic system on an aircraft includes the environmental control system (ECS) and the wing ice protection system (WIPS). ECS is responsible for maintaining conditioned tem-

perature and air pressure in the cabin while WIPS is equipped for de-icing of the wing. Hydraulic implementation include the actuation of steering and extension/retraction system, for example, the nose-landing-gear and wheel steering system . Mechanical power can be found in the flight control systems (rudders, elevators, ailerons and flaps), etc. Electric energy is overwhelming in low to medium power applications. It is utilized in avionics, on-board lighting and entertainment system, just to name a few.

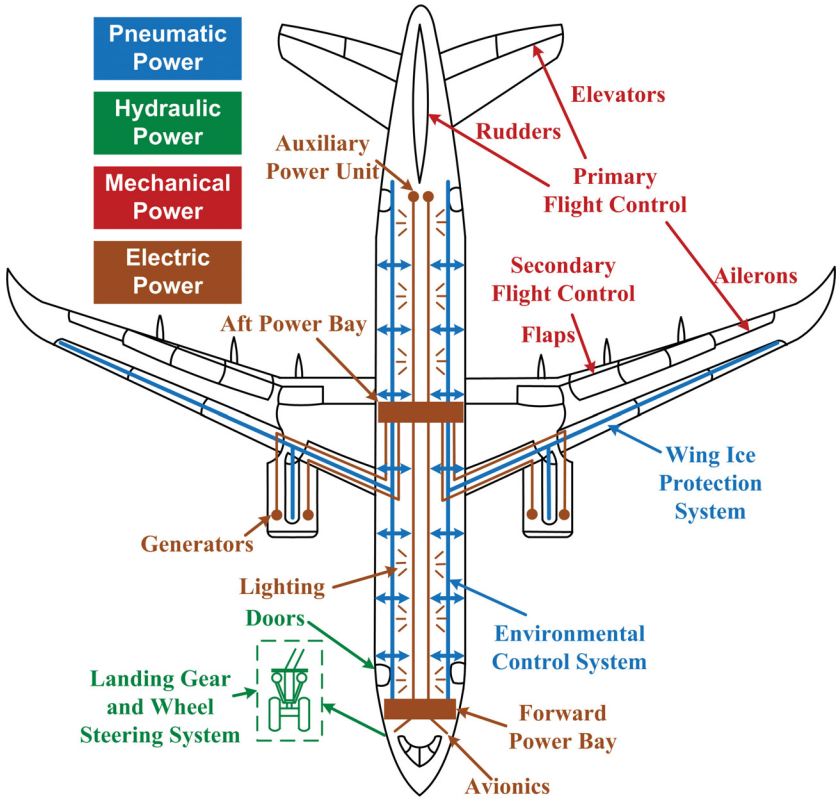

Figure 1.1: Power types on aircraft and their typical applications.

The more electric aircraft, as its name implies, aims at replacing as much parts of the pneumatic, hydraulic and mechanical system with electric system. The potential to expand electric power is continually under investigation and some progress has already been made and reported. Three of the most renowned electrification results are electrically-driven environmental control system (E-ECS), the electro-hydrostatic-actuator (EHSA) and electro-mechanical-actuator (EMA).

The traditional aircraft uses extracted bleed air from the engine for environmental control purpose while the electrically-driven ECS intakes ambient air as input and reaps energy savings over using engine bleed air as it does not require a pressure reduction valve and, as the temperature of the pre-compressor is less than

engine bleed air, thus requiring less pre-cooling [2]. The Boeing®-787 is equipped with a large-scale electric power system to eliminate the traditional pneumatic system and bleed manifold, which is called "No-Bleed Systems" by the company. In the Boeing®-787, a set of compressors utilizing electric power is used to regulate the temperature and pressure in the cabin, eliminating the pneumatic system and air ducts from the engine [3]. In the E-ECS architecture, there is no need to regulate down the supplied compressed air. Instead, the compressed air is produced by adjustable speed motor compressors at the required pressure without significant energy waste. That results in significant improvements in engine fuel consumption [4].

Hydraulic actuators are used for delivering high actuation forces and high power density due to their simple construction and low cost [5]. However, conventional hydraulic actuation systems employ valves to conduct and control the fluid flow produced by a motor-pump group running at constant speed. This working principle penalizes efficiency. Moreover, the significant number of required components has a negative impact on costs, complexity, and overall dimensions. [6]. As a result, the new electro-hydrostatic-actuator concept is conceived and developed. The EHSA system uses a hydraulic pump to transfer the rotational motion of electric motor to the actuator output in which the inefficient servo valve is eliminated. The EHSA is based on the principle of closed-circuit hydrostatic transmission, so that there are no requirements for oil reservoir and electro-hydraulic servo-valves [7]- [8]. The EHSA combines the benefits of conventional hydraulic systems and direct-drive electrical actuators, namely, high torque/mass ratio and modularity [9], as well as high energy efficiency, due to the fact that the pump works only on a movement demand and the actuating power is transferred by electricity (Power by Wire) instead of by the oil in the pipes (Power by Pipe) [10].

The EMA is an appealing candidate for flight control on MEA because of its benefits such as a decrease in maintenance effort and weight, and an increase in efficiency [11] and the potential advantage of more flexible flight control by introducing distributed actuation system architecture [12]. An electro-mechanical-actuator is generally constituted of power electronic module, electric motor, gearbox and ball screw. It is a device where the rotational energy produced by variable speed electrical motor is mechanically converted to energy at the aircraft control surface via a high efficient mechanical transmission. The EMA is controlled by the power electronic module and the associated electrical motor. The motor speed reversal allows the screw to move forth and back according to the position demand. The

force supplied by the screw to the surface is controlled by the motor currents [13]. Although EMA behaves not as good as hydraulic system with respect to fault-tolerant performance, which hinders the massive use of EMAs in flight control actuators [14], it is anticipated that this barrier may be broken in the future with the development of power electronics technology with enhanced reliability.

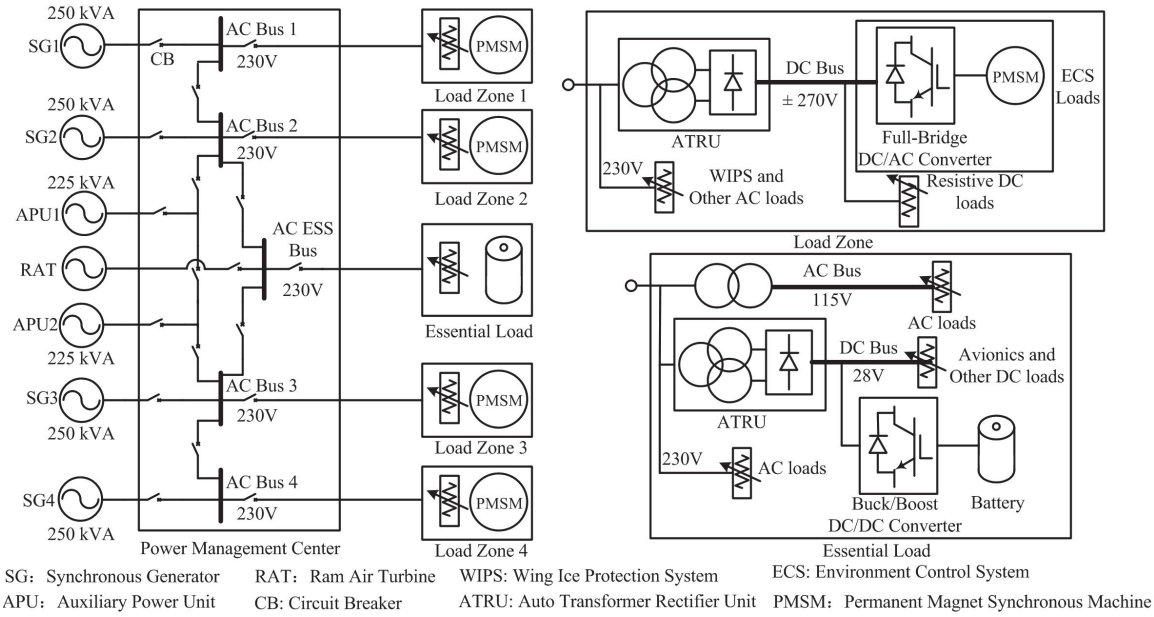

Figure 1.2: Structure of Boeing®-787 electrical system.

Apart from the aforementioned multi-domain parts, the electrical part on a MEA itself is a large complex system which includes complete subsections (generation, transmission and distribution) of a typical power system. Fig. 1.2 shows the architecture of Boeing®-787 on-board power system. As can be seen that there are four synchronous generators as well as two auxiliary power units and one ram air turbine in the generation part. The four generators each powers one variable frequency AC bus for electric power distribution. To enhance the reliability of the power grid, these AC buses are interconnected by circuit breakers that are controlled by power management center so that they can back-up each other during faulty period. Accordingly, loads on the aircraft are also partitioned into four zones that receive energy from the corresponding four AC buses. Located in each load zone, there exists auto transformer rectifier unit (ATRU) to transform AC power into DC power and the loads are connected on the AC or DC bus. The electric power is transferred into pneumatic, hydraulic and mechanical power through the motor drive system. In addition to the normal load, there are some essential loads

that cannot afford to lose power because of their extreme important impact on aircraft safety, for example, the avionics. Such loads are connected to an essential bus that is equipped with energy storage system. In case of power loss, the energy storage system starts working to ensure quick recovery of power on essential bus.

It can be seen that the MEA on-board power system is a very large-scale high-complexity electric circuit that contains massive components and multi-domain parts, which makes it very challenging for analyzing.

1.1.2 State-of-the-Art of Conventional Circuit Modeling Methods

Circuit simulation is essential in most of the electric system's design and validation process as it can serve as a powerful tool to reflect the electric system's behavior and properties [15]- [16]. Up to now, there are basically two categories of mature algorithms in modern circuit simulation area: the nodal analysis method [17]- [20] (also known as resistive companion method, Dommel algorithm, etc) and state-space method [21]- [26](also known as state-variable method). The simulation program typically selects one algorithm and develops the system matrix according to the method's corresponding modeling rule. These two methods have been validated by various circuits and both evolved mature software. Representative of nodal analysis method is PSCAD/EMTDC® [27] and the state-space method is MATLAB/Simulink® [28].

However, both these algorithms become computational inefficient when the circuit's scale becomes large. The reason is evident: the size of system matrix increases along with the circuit's scale. This problem is especially severe for the nodal analysis method because it requires matrix division in every time-step. The computational complexity of direct matrix inversion is $O(N^3)$; even when an advanced solver such as Gaussian elimination method is used, the complexity can only be reduced to $O(N^3/3)$, still in order 3 of the matrix size. As for the state-space method, the complexity depends on the discretization method. If the Forward Euler method is adopted, it requires only one matrix multiplication in every time-step and the computational complexity is $O(N^2)$. But Forward Euler method behaves poorly with respect of numerical stability. In most cases, some advanced algorithms, like Heun, or the Runge-Kutta method, have to be adopted. However, as long as the discretization method is in explicit form, the complexity will still be in order 2 of the matrix size, and once an implicit method, such as Backward Euler and Trapezoidal Rule, is chosen, the complexity will increase to order 3.

There have been various attempts to reduce the computational complexity of

the circuit solution. The most natural guideline is circuit decoupling. Two successful methods have been created in the literature and implemented in many applications: latency insertion method (LIM) [29]- [31] and transmission line modeling (TLM) method [32]- [33]. The basic idea of these methods is similar. They take advantage of the inductive and capacitive elements in the network to create latency between two subsystems so as to decouple them. The difference is that LIM requires inductive element along every branch and capacitive element between every node with ground while TLM only introduces latency in several parts of the network. Thus, LIM realizes fully decoupling of the circuit network and the computational complexity reduces to linear, at the expense of modifying the circuit model because there are seldom cases when the circuit meets the requirement of LIM originally. TLM is usually used to decouple the system when solving nonlinearities or the two subsystems already have some decoupling nature such as parallel connection by a large capacitance. Therefore, TLM can be deemed as partial decoupling of the network and traditional methods are utilized within the decoupled subsystem.

Although these two decoupling methods are successful in many applications, they still have limitations. One common deficiency is the difficulty of selecting an appropriate value of latency, especially when this latency is inserted virtually, i.e., it does not exist in the real system. If the latency is too small (which means smaller time-step), it may lose the advantage of computational efficiency. On the other hand, if the latency is too large, it may suffer from numerical instability or may distort the original circuit's transients. There is no standard way or formula for choosing the latency in literature and it is often done manually, i.e., by trial and error iteration.

1.2 Motivation and Objectives of This Work

Considering the aforementioned insufficiency, simulation of large-scale circuits still poses a challenge. Some special modeling techniques and computational strategies have to be created to simplify the solving process.

Typically speaking, the behavior of a circuit is determined by two factors—the circuit topology and the component's characteristics. However, the traditional modeling methods often mix these two factors into one system matrix, i.e., whenever there is a change in the circuit topology or the component's characteristics, the system matrix has to be reformed. But in most cases the circuit topology remains

unaltered in the simulation and the component's characteristics are the main stimulus of the transients. This is especially true for the power electronic circuits, which are common in MEA system.

This thesis aims at presenting a method that is able to de-couple the circuit topology and component's characteristics in modeling process and deal with them separately. This method will be referred to as Efficient Zonal Method (EZM) henceforth. Under EZM, matrix inversion is only required when analyzing the topology. It is very easy to compute and suitable for computer programing. The resulting computational complexity reduces to nearly linear with the circuit scale—a significant reduction compared with traditional modeling methods. These features make EZM very suitable for large-scale circuit simulation.

The EZM is based on a newly found circuit lemma that indicates the relationship of circuit branch voltages and currents in a very neat manner. The proving process of this lemma is also provided. By utilization of this new lemma, circuit de-coupling can be conducted down to the lowest component level. Every component in the circuit can be viewed as independent voltage or current source. Matrix operation is only required when analyzing circuit topology and it's very efficient on computer because topology matrix entries only have three possible values: 0 or 1 or -1.

By employment of EZM, the comprehensive modeling of MEA system becomes relatively easy and efficient in computation because the whole system can be dealt with in a divide and conquer manner.

The constructed comprehensive simulation model mainly focuses on system-level performance analysis and design considering the computation ability of the hardware. However, apparatus-level simulation is also achievable if sophisticated component models and more advanced computation hardwares are available. This model is helpful for the design and testing of MEA and provides great facility for industrial and academic engineers to analyze MEA system. The EZM is even worth being promoted to model other complex systems that contain large-scale circuit. The proposed new circuit lemma and the corresponding EZM are significant advance in theory for simplifying circuit modeling and simulation.

1.3 Contributions of the Thesis

The main contributions of this thesis can be summarized as following:

- A Fast and stable method for modeling generalized nonlinearities in power

electronic circuit simulation
Nonlinearities have been the major obstructions that limit the computational efficiency in power electronic circuit simulation for a long time. Yet there is no standard way for dealing with them. This thesis presents a new method that makes the handling of nonlinearities fast and stable. In the proposed method, nonlinearities are transformed into a uniform representation—a constant resistor in parallel with a companion current source, thus making the system admittance matrix constant for fixed time-step simulation. To solve for the corresponding companion current source, nonlinearities are treated as either current or voltage sources and a diagonal time-varying matrix equation is developed. Three methods are proposed for solving the matrix equation—precomputed inversion or factorization, modified Gaussian elimination, and updating inverse using the Sherman–Morrison formula—that can fit different system sizes and applications. The proposed method is validated by two common power electronic converter topologies, both in offline and real-time simulation. Offline tests show that the proposed method achieved the same accuracy with the mature simulation software while being more than ten times faster. The same test cases are also implemented into field programmable gate arrays based real-time simulation experiments for verification.

- The EZM modeling methodology for large-scale circuit simulation
  Large-scale circuit simulation poses a challenge to most simulation tools because of its high computational complexity. This thesis presents an efficient method, which decouples the circuit topology and components' characteristics in computation so as to make it suitable for large-scale circuit simulation. The proposed method is based on a circuit lemma, which indicates the relationship of branch voltages and currents. The proving process of this lemma is provided in this thesis. The working principle of the proposed method is elaborated and its numerical stability is also analyzed. This method achieves nearly linear computational complexity and is very suitable for hierarchical and zonal computation. The proposed method is verified by real-time application on the more electric aircraft microgrid. Hardware-in-the-loop testing of this study case on Xilinx Virtex Ultrascale+ field programmable gate array (FPGA) board is achieved and the results are compared with PSCAD/EMTDC. The resulting waveforms from these two simulation tools show very good agreement on both normal and fault operation

test scenarios, which demonstrates that the proposed method has very good performance on computational accuracy and efficiency

- Unified solver based real-time multi-domain simulation of aircraft electro-mechanical-actuator
  Electro-mechanical-actuator is the key component to convert electrical power into mechanical power for flight control in next-generation aircrafts. Multi-domain simulation of EMA can benefit its on-going evolution process. This thesis presents the real-time multi-domain modeling and simulation of an EMA as elevator for flight control by utilization of EZM. Several key issue concerning the computational efficiency and successful implementation of this solver are provided and its relationship with state-space model is also elaborated. Analysis shows that EZM could be a competitive candidate for multi-domain simulation because of its high computational efficiency and relatively less modeling effort. Electrical, mechacnical, and thermal parts of the EMA are modeled and simulated interactively based on EZM modeling methodology. The multi-domain model is implemented on FPGA board and executes in real-time. Simulation results from FPGA board and commerical softwares under several test senarios coincide with each other in very high degree, which showcases the efficacy of EZM with respect to computational efficiency and ability to accomodate multi-domain models. The proposed model and solver are useful for hardware-in-the-loop (HIL) design and testing of EMA.

- A fast time-step selection method for explicit solver based simulation of high frequency low loss circuit and its application on EMI filter
  Electromagnetic interference (EMI) modeling and prediction are essential for most power electronics apparatuses. This thesis aims at finding a fast method to select time-step for explicit solver based simulation of high frequency low loss (HFLL) circuits like the EMI filter. The state-space model of HFLL circuit is constructed and its eigenvalues are proved to be locating on the imaginary axis. Both the non-degenerate and degenerate circuit cases are discussed. During the analysis, a circuit lemma is summarized on how to transform degenerate circuit into nondegenerate circuit and the corresponding inversion of its coefficient matrix is derived based on Sherman-Morrison's formula. Then the Laguerre-Samuelson's inequality is employed to find the upper bound of HFLL circuit's eigenvalues. This process only requires two

matrix multiplications and traces of the matrix operation results, thus keeping the computational complexity retaining in $O(N^2)$. A typical EMI filter is constructed and its equivalent circuit including the parasitic effects is extracted from ANSYS. This filter is simulated in application between a DC/AC converter and the grid using the 4th-order Runge-Kutta (RK4) solver with a time-step selected by the proposed method (other numerical integration methods are also possible as long as they are in explicit form). Numerical test shows that the spectrum results are very close to those obtained by experiment while being much more efficient than traditional methods, which demonstrates that this timestep selection method could benefit the analysis and time-domain simulation of HFLL circuits.

- Modular assembly and real-time hardware emulation of on-the-move multi-domain multi-machine system on more electric aircraft
  Multi-domain and multi-machine are two significant features of the on-the-move powertrains on more electric aircraft. To successfully simulate the dynamic behaviors of MEA, not only the multi-disciplinary characteristics should be incorporated, but their interfacing issue should be considered. This thesis presents a modular assembly methodology to model the multi-domain multi-machine system on MEA and achieves real-time emulation on field programmable gate array (FPGA) hardware. The various domain (pneumatic, hydraulic, mechanical) parts are viewed as modules and interfaced with the electric domain through machine drive system. State-space model of the multi-machine drive system is developed accordingly and the eigenvalue distribution is analyzed. Practical eigenvalues bounds (both real and imaginary part) are derived to facilitate the parallel computation. An 100-machine drive system is then constructed and a Monte-Carlo test is performed to validate the effectiveness of the eigenvalue bounds. High fidelity real-time emulation of the MEA multi-domain multi-machine is realized on FPGA. Pneumatic, hydraulic and mechanical characteristic waveforms are exhibited along with their comparisons from Matlab/Simulink®. High agreement on these transients waveforms suggests that this modular assembly approach could be a helpful scheme for the modeling and design of MEA powertrains.

1.4 Thesis Outline

This thesis consists of seven chapters and is organized as follows:

- **Chapter 1: Introduction** - This chapter discusses the background of this research. The state-of-the-art of more electric aircraft and conventional circuit modeling methods are reviewed. The motivation and objectives of the thesis are specified and the main contributions are listed.

- **Chapter 2: The Origination of EZM: An Idea for Modeling Nonlinearities** - This chapter discusses how the EZM is originated. In specific, an idea for modeling nonlinearities, especially the switching device transient in power electronic circuit simulation, is presented. This idea can be applied to prove the voltage-current relation used in EZM modeling process.

- **Chapter 3: Modeling Methodology and Mathematic Analysis of EZM** - This chapter discusses the modeling methodology of EZM. The working principle and main properties of EZM are presented. The relation between EZM model and state-space model is also analyzed.

- **Chapter 4: A Fast Time-step Selection Approach for EZM** - This chapter discusses a time-step selection approach for EZM. This approach is based on the idea of identifying the upper bound of the system eigenvalues and then selecting the time-step to make the upper bound locating in the numerical integration method's stability region.

- **Chapter 5: EZM Based Modular Assembly Modeling of More Electric Aircraft** - This chapter discusses how EZM can be used to model the more electric aircraft in modular assembly way. The multi-domain multi-machine system on more electric aircraft which contains multiple pneumatic, hydraulic, mechanical and electric modules are modeled. The eigenvalues of the system is also analyzed to provide information on performance evaluation.

- **Chapter 6: Real-Time Simulation Performance and Results of the EZM Based MEA Model** - This chapter discusses the real-time simulation results of the EZM based MEA model. The normal and fault operation test scenario as well as the transient behavior of E-ECS, EHSA and EMA modules are presented. Waveforms from commercial simulation softwares under the same test condition are also provided for accuracy and efficiency comparison.

- **Chapter 7: Conclusions and Future Work** - This chapter discusses the conclusions and possible future work of this research.

2

The Origination of EZM: An Idea for Modeling Nonlinearities

2.1 Introduction

Modern power electronic systems need more powerful simulation tools to meet the demands of speed and accuracy as the system complexity increases accordingly. Some systems, such as the modular multilevel converter (MMC), contain hundreds of components, including both linear (capacitors, inductors) and nonlinear (semiconductor switches) components in one circuit instance. The large number of switching elements in the MMC introduces a challenge for modeling the converter on electromagnetic transient (EMT) simulation programs [34]. The linear components can be dealt with properly using numerical integration methods such as Backward Euler or the Trapezoidal method, while the nonlinear components, still pose the bottleneck of simulation performance.

Nonlinearities bring uncertainties into the system admittance matrix for nodal analysis and should be taken care of differently according to their characteristics [17]. Basically, there are two ways to deal with nonlinearities: iterative and non-iterative. The iterative methods combine the linear network equations with nonlinear characteristic equations and try to find a solution that satisfies them both. Some iterative algorithms, such as the Newton-Raphson method, are utilized to search for the solution. The iterative solution (if it exists) is always theoretic ac-

curate (i.e., no approximations are made). One example of an iterative model is the zinc-oxide arrester model in the EMTP [35] and the on-line monitoring program in [36], which use an analytic equation to model its behavior. Other examples can be found in the works of [37]- [40]. However, there are mainly two drawbacks to iterative methods. First, there is no theoretical guarantee that the iteration solution can be found; in some cases the iteration methods do not converge. Second, the iterative search is usually time-consuming for a required accuracy because the convergence speed varies case-by-case. Thus, iterative approaches are typically employed in high accuracy and non-time-critical applications, usually off-line simulation for a limited system size. Some simulation tools, such as SaberRD®, Pspice® and PAN academic circuit simulator (described in [41]), belong to this category.

Non-iterative methods usually sacrifice some accuracy to trade for simulation speed so that they can be utilized in time-critical applications such as real-time simulation or to handle larger systems. There are numerous effective schemes to simplify nonlinearities. Many of them are designed based on the specific nonlinearity's characteristics, and therefore can not be promoted as general methods. Among these approaches, two of the most commonly used are: (1) current-source representation with time lag Δt; and (2) piecewise linear representations [35]. The first approach is easy to understand and implement. At simulation time t, all variables are known at $t - \Delta t$ (here a fixed time-step method is assumed); thus they can be used to calculate the current flow of nonlinear element at time $t - \Delta t$ and inject it as a current source at time t. Some very complicated or large-inertia nonlinear elements are implemented using this way, such as electric machines in PSCAD/EMTDC® [27] and the work in [42]. However, under this principle, any sudden change in voltage causes a current response only in the next time-step. Thus, for the previous time-step, the machine looks like an open-circuit and spurious spikes may appear in the machine terminal voltage [43]. In order to alleviate this phenomenon, some modifications have to be made. In [43], a resistance is placed in parallel with the machine to reduce the spurious spikes and an additional compensated current source is added to offset the current introduced by this resistance. The current-source representation with time lag Δt runs fast in simulation and is accurate provided that the time step is small enough. This condition, however, is not difficult to meet as the digital processor performance has increased dramatically over the years.

The piecewise linear approach divides the nonlinear element characteristics into several working sections and models it as a linear component with different

parameters to fit its characteristic in each section. Typical example of this method is the simple switch model in PSCAD/EMTDC®. During on state, it acts as a very small resistance while in off state a very large resistance [27]. Other piecewise linear model applications can be found in the works of [44]- [49]. This approach can achieve a reasonable accuracy while retaining an elegant mathematic form. However, the varying parameters will alter the system admittance matrix and each time it is changed, the triangularization or inversion process has to be re-conducted, thus lowering the simulation speed. If there are lots of nonlinear elements in system, such as the MMC, the execution rate can be extremely low, therefore, making this approach impractical. There are some efforts to make the switch model equal for both on and off states [50]- [51] so as to make the admittance matrix constant. However, such methods either induce inaccurate power losses or require complicated revising calculations, and cannot be promoted to model other nonlinearities. [52] presents a method to simulate the piecewise linear elements using constant admittance matrix and maintains speed advantage over general-purpose simulation tools; however, the equivalent resistor's value and the computation of companion current source of piecewise linear elements are not addressed fully.

These two approaches have covered the most scope of non-iterative nonlinear element modeling, yet they can not replace one another. For components like electric machines, it is very difficult to find their equivalent linear circuits because their characteristics change continually with rotor position, angular velocity, magnetic flux saturation etc. On the other hand, components like switches are not suitable for current source representations with time lag Δt, because during on state they behave more like a voltage source (i.e., zero terminal voltage with almost arbitrary current). Due to the limitation of these two modeling methods, they have to coexist in one simulation; however, the different mathematic representations make the solution process complex and lower the execution efficiency.

Some other methods decouple the nonlinear components manually so that they can be dealt with independently [29]- [30]. These include the latency insertion method (LIM) and transmission line modeling (TLM) method. Such methods introduce artificial latency into a system (by inserting small inductive or capacitive elements) so as to permit a complete (approximate) decoupling of the system equations [30]. The side-effect is that the inserted inductive or capacitive elements may distort the original component's behavior when its time constant is very small. Therefore, sometimes it is very difficult to choose the appropriate latency or transmission line parameters.

In this chapter, a generalized method for modeling nonlinear elements in power electronic circuit simulation is presented. This method can deal with any form of nonlinear characteristic using a uniform mathematic representation, thus making the admittance matrix constant. By proper selecting of the equivalent resistor, the time-varying part of the matrix to solve nonlinear elements is restricted only on diagonals. Three methods to solve the diagonal time-varying matrix equations are presented correspondingly. These properties can significantly reduce the execution burden of the simulation program. In addition, the system is decoupled naturally and only when there are real inductances or capacitances, thus high accuracy is retained. Besides, the method does not have instability risk because it is inherently stable. Off-line and real-time simulation results of two typical power electronic circuits—MMC and neutral point clamped (NPC) topologies, are provided and compared with the existing simulation softwares both at system-level and device-level. This chapter is organized as following: Sec.2.1 and Sec.2.3 introduce the uniform representation of nonlinear element and the classification of nonlinear behaviors; Sec. 2.4 elaborates the solution process of nonlinear elements' companion current source; Sec. 2.5 and Sec. 2.6 present the off-line and real-time simulation validation results and Sec. 2.7 gives the conclusion.

2.2 Uniform Representation of Nonlinear Elements

Most of the circuit simulation programs choose node voltages as the unknown variables and use nodal analysis to develop a set of linear equations by applying Kirchhoff's Current Law (KCL) at every circuit node. In nodal analysis, it is preferable to use the Norton equivalent circuit (a current source in parallel with a resistive branch) to represent the circuit element. Fig. 2.1 shows the Norton equivalent representation of lumped linear inductance and capacitance.

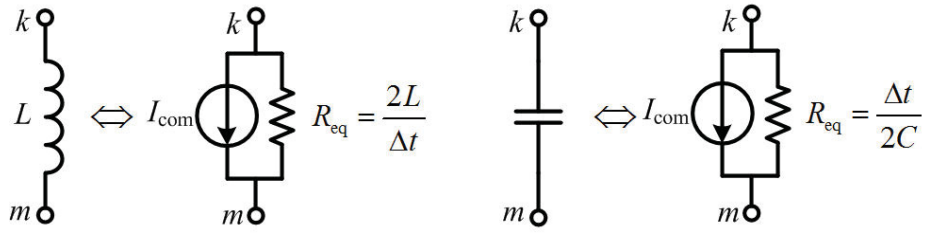

Figure 2.1: Norton equivalent circuit of lumped inductance and capacitance.

The equivalent resistor R_{eq} is obtained using Trapezoidal rule of integration

and it is a constant for a fixed time-step Δt. The companion current source I_{com} is calculated from the past history (the previous time-step variables) [17]. However, when applying this concept to nonlinear elements, usually both R_{eq} and I_{com} are time varying, thus making the analytical solution process complex and the computational complexity of solving a time-vary matrix equation is $O(N^3/3)$. Actually, the potential of I_{com} has not been exploited fully yet. I_{com} can be calculated not only from history variables, but also from current time-step variables. Assume that there is a nonlinear element connecting with external network at node k and m, as shown in Fig. 2.2. No matter what kind of characteristics this nonlinear element possesses, ultimately there exists a solution for terminal voltage $v_{km}(t)$ and branch current $i_{km}(t)$ at simulation time t. From the point view of external network, as long as (2.1) is satisfied, it can not distinguish whether the component between node k and m is a nonlinear element or a constant resistor R_{eq} in parallel with a current source I_{com}.

$$I_{com}\,(t) = i_{km}(t) - \frac{v_{km}(t)}{R_{eq}}. \tag{2.1}$$

As can be seen from Fig. 2.2, the equivalent resistor for the nonlinear element is a constant, just like the linear element in a fixed time-step simulation. Thus the system admittance matrix becomes constant since only the equivalent resistor will appear in the admittance matrix. As a result, the computational complexity for solving node voltages reduces to $O(N^2)$.

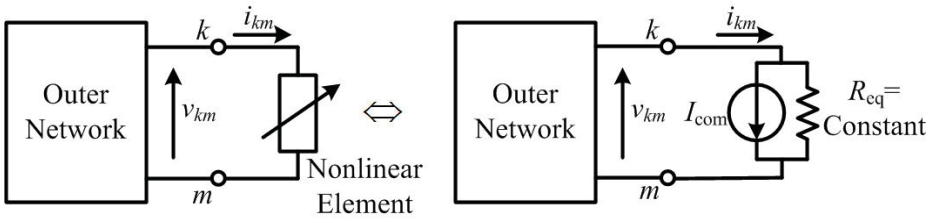

Figure 2.2: Norton equivalent circuit of nonlinear element.

The only problem of applying this representation for nonlinear elements is how to find this $I_{com}(t)$ that satisfies (2.1) since both $v_{km}(t)$ and $i_{km}(t)$ are unknown. Actually, (2.1) is difficult to solve because not only the relationship between $v_{km}(t)$ and $i_{km}(t)$ is nonlinear, but also that the external network may contain multiple nonlinear components. The theoretic accurate solution cannot be found without using iterative methods. In order to save execution time, approximations have to be made like all other non-iterative methods.

2.3 Classification of Nonlinear Behavior

Before introducing the appropriate approximations that should be made to match this uniform representation, the nonlinear behaviors are classified first. Typically speaking, nonlinear behavior can be roughly classified into two categories: current-source-type behavior and voltage-source-type behavior. Some nonlinear elements always behave as one type, but others may transfer types according to their working condition. The classification is done mainly by empirical conventions and can be programed into the model as an attribute for reuse. Table 2.1 lists some conventions of nonlinearities.

Table 2.1: Some conventions of nonlinearities

Voltage-source-type	**Current-source-type**
Batteries, Generators Switches in turn-on transients and steady on-state	PV panels, Motors, Switches in turn-off transients and steady off-state

2.3.1 Current-Source-Type Behavior

Typical current-source-type behaviors include the output characteristics of photovoltaic (PV) panel, an electric machine under load mode, semiconductor switch in turn-off transient and steady off state, etc. What they have in common is that they can be viewed as a current source in the circuit and more importantly, their current can be predicted precisely based on the history (for example the previous time-step) information. Take the semiconductor switch as an example, the turn-off transient characteristics can be obtained experimentally and recorded to develop a turn-off analytical function, as shown in Fig. 2.3(a). Some of the characteristic parameters, like turn-off delay time $t_{\mathrm{d(off)}}$ and fall time t_{f} can be extracted from experimental data. Finally, a per-unit turn-off function can be obtained and used to generate the actual waveforms by scaling with the current amplitude in simulation. The key point of this method is to determine the current value at next time-step by a pre-defined trajectory and this trajectory comes from many experimental measurements to achieve a high precision. This approach has a very good curve-fitting performance and offers reasonable accuracy for current prediction in turn-off transient [42], [53]. As for the steady off state, the switching device can be viewed as a current source whose current is zero. Other elements, like PV panel

and electric machine, do not have a pre-defined trajectory. Their current can be predicted simply because of system inertia. Provided that the time-step is small enough, their current can be updated using previous time-step information and assumed to be consistent over one time-step.

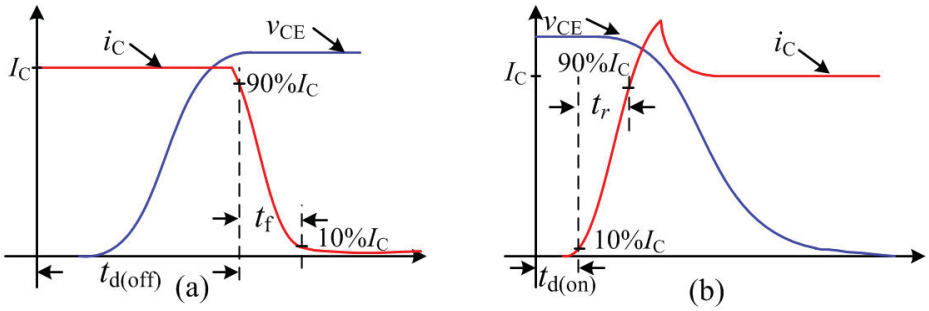

Figure 2.3: Switching transients of semiconductor switches. (a) Turn-off transient; (b) Turn-on transient.

2.3.2 Voltage-Source-Type Behavior

Typical voltage-source-type behaviors include the output characteristics of most kinds of batteries, an electric machine under generator mode, semiconductor switches in turn-on transient and steady on state, etc. What they have in common is that they can be viewed as a voltage source in the circuit and more importantly, their voltage can be predicted precisely based on the history information. For example, the voltage trajectory of a semiconductor switch in turn-on transient can be tested and recorded to develop a per-unit function. When scaled with the voltage amplitude in simulation, it can predict the voltage value at next time-step. Other elements' voltages, like batteries and electric machines, can be predicted because of their system inertia.

One may ask since the voltage and current trajectories of semiconductor switches can be recorded simultaneously in experiments, why under turn-off transient should it be treated as a current source and under turn-on transient as a voltage source? That is because under turn-off transient, the conducting current will decrease from some value to zero, which means the initial and final value of current are known during this period. Then the initial current value can be used as the scaling factor of the per-unit function. While in the same period, the voltage across the switch will increase from almost zero to some value that the program does not know. The voltage per-unit function is useless without an appropriate scaling factor. Actually, the voltage waveform of semiconductor switch under turn-off transient is usually

determined by its complementary device's voltage turn-on trajectory. This can be illustrated in Fig. 2.4. If S_1 is under turn-off transient, then S_2 or its anti-parallel

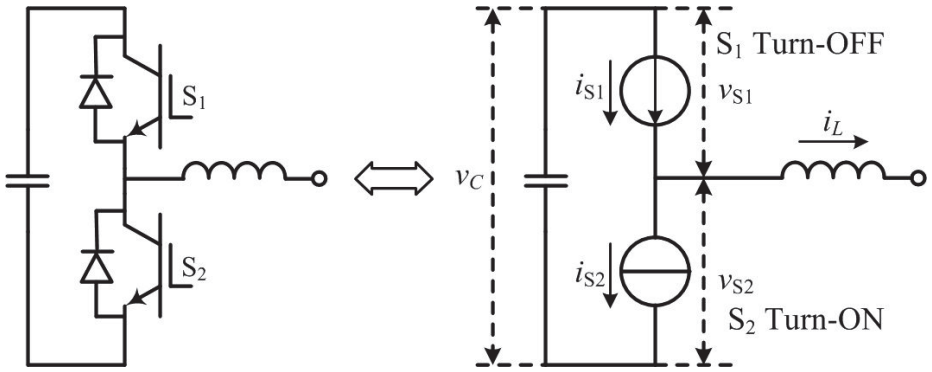

Figure 2.4: Switching transient analysis of two complementary semiconductor switches.

diode will be under turn-on transient. S_1 will act as a current source and S_2 a voltage source. The current of S_2 is determined by the difference of i_L and i_{S1} while the voltage of S_1 is determined by the difference of v_C and v_{S2}.

2.4 Solution Process of Nonlinear Elements' Companion Current Sources

Assume that all the elements in the system to be simulated are represented by their Norton representations, and the equivalent resistor is constant for linear and nonlinear components. Then a set of node voltage equations can be formed by applying KCL, as the matrix equality shown in (3.1):

$$\mathbf{GV} = \mathbf{I}', \tag{2.2}$$

where $\mathbf{G}$ is a constant nodal conductance matrix, $\mathbf{V}$ is the node voltage vector and $\mathbf{I}'$ is the companion current source vector. Note that the members of $\mathbf{I}'$ are not independent companion current sources but their linear combinations. For example, the equivalent circuit of the half-bridge topology in Fig. 2.4 is drawn in Fig. 2.5 and the KCL equation at node ② can be expressed as follows:

$$\begin{aligned} -\frac{1}{R_{S1}}v_1 + \left(\frac{1}{R_{S1}} + \frac{1}{R_{S2}} + \frac{1}{R_L}\right)v_2 - \frac{1}{R_{S2}}v_3 - \frac{1}{R_L}v_4 \\ = I_{S1} - I_{S2} - I_L. \end{aligned} \tag{2.3}$$

The right hand side of (2.3) can be further transformed as a constant vector multiplying the independent companion current source vector $\mathbf{I}$ shown in (2.4).

$$I_{S1} - I_{S2} - I_L = \begin{bmatrix} 1 & -1 & 0 & -1 \end{bmatrix} \begin{bmatrix} I_{S1} \\ I_{S2} \\ I_C \\ I_L \end{bmatrix}. \tag{2.4}$$

Assume that there are N_1 nodes and N_2 independent companion current sources

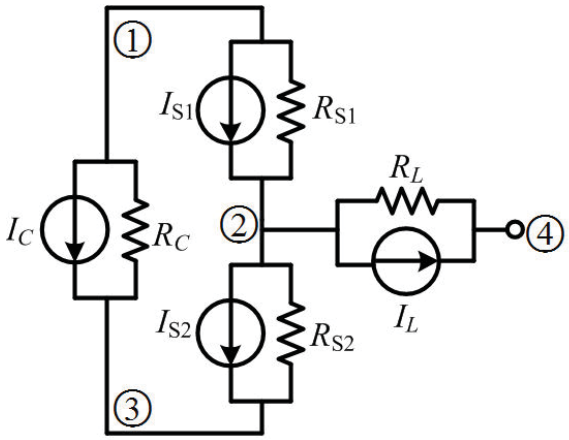

Figure 2.5: Equivalent circuit of half-bridge topology.

in the system, then the matrix equality in (3.1) can be recomposed as following:

$$\mathbf{G}_{N1\times N1}\mathbf{V}_{N1\times 1} = \mathbf{I'}_{N_1\times 1} = \mathbf{T}_{N_1\times N_2}\mathbf{I}_{N_2\times 1}, \tag{2.5}$$

where each row of $\mathbf{T}$ indicates the current source configuration at one node. $\mathbf{T}$ is also constant and its elements are either 0 or 1 or -1. Based on (2.5), the node voltage vector can be expressed as:

$$\mathbf{V}_{N1\times 1} = \mathbf{G}^{-1}_{N1\times N1}\mathbf{T}_{N_1\times N_2}\mathbf{I}_{N_2\times 1} = \mathbf{A}_{N_1\times N_2}\mathbf{I}_{N_2\times 1}, \tag{2.6}$$

where $\mathbf{A}_{N_1\times N_2} = \mathbf{G}^{-1}_{N1\times N1}\mathbf{T}_{N_1\times N_2}$. Note that $\mathbf{A}_{N_1\times N_2}$ is constant as well since both $\mathbf{G}_{N1\times N1}$ and $\mathbf{T}_{N_1\times N_2}$ are constant.

Equation (2.6) reveals an important piece of information: given that all the components in system are represented by constant resistors in parallel with current sources, the node voltage can be expressed as linear combinations of these current sources and more importantly, the coefficients of these current sources are constant. This is also true for any voltage difference between two nodes. For example,

the voltage difference between node k and m at simulation time t can be expressed as

$$v_{km}(t) = \sum_{j=1}^{N_2} \left(A_{k,j} - A_{m,j}\right) I_j(t). \tag{2.7}$$

Furthermore, the branch current between node k and m is given as:

$$\begin{aligned} i_{km}(t) &= \frac{v_{km}(t)}{R_{eq}} + I_l(t) \\ &= \frac{\sum_{j=1}^{N_2} \left(A_{k,j} - A_{m,j}\right) I_j(t)}{R_{eq}} + I_l(t), \end{aligned} \tag{2.8}$$

where l is the index number of I_{com} between node k and m in the system.

As discussed in Sec. III, the nonlinear element will behave like a current or voltage source according to its nature or working condition and its current or voltage value at next time-step can be predicted with reasonable precision. Then either $i_{km}(t)$ or $v_{km}(t)$ in (2.1) can be replaced with the predicted value. This is the approximation that is made to simplify the solution process of nonlinearities' $I_{com}(t)$.

Assume that there are N_3 nonlinear elements or pure voltage/current sources labeled as 1 to N_3 (here pure voltage/current sources and nonlinear elements are categorized into one group since they have no differences from the point view of the simulation program) and N_4 linear elements labeled as $N_3 + 1$ to N_2 in system ($N_4 = N_2 - N_3$). If the simulation program has finished the calculations at time $t - \Delta t$ and is going forward to time t, the companion current source of N_4 linear elements can be computed first based on information at time $t-\Delta t$. The companion current source of the other N_3 elements should be solved based on (2.1). For each of these N_3 elements, if $i_{km}(t)$ is known, then replacing $v_{km}(t)$ with (2.7) to have

$$I_l(t) = i_{km}(t) - \frac{\sum_{j=1}^{N_2} \left(A_{k,j} - A_{m,j}\right) I_j(t)}{R_{eq}}, \tag{2.9}$$

which can be rewritten as:

$$\begin{aligned} &\frac{1}{R_{eq}} \sum_{j=1}^{N_3} \left(A_{k,j} - A_{m,j}\right) I_j(t) + I_l(t) \\ &\qquad = i_{km}(t) - \frac{1}{R_{eq}} \sum_{j=N_3+1}^{N_2} \left(A_{k,j} - A_{m,j}\right) I_j(t). \end{aligned} \tag{2.10}$$

If $v_{km}(t)$ is known, then replacing $i_{km}(t)$ with (2.8) results in:

$$I_l(t) = \frac{\sum_{j=1}^{N_2} \left(A_{k,j} - A_{m,j}\right) I_j(t)}{R_{eq}} + I_l(t) + \frac{v_{km}(t)}{R_{eq}}, \tag{2.11}$$

which can in-turn be rewritten as:

$$\begin{aligned}\sum_{j=1}^{N_3}(A_{k,j}-A_{m,j})I_j(t)\\ = v_{km}(t)-\sum_{j=N_3+1}^{N_2}(A_{k,j}-A_{m,j})\,I_j(t).\end{aligned} \tag{2.12}$$

In Sec. II, the equivalent resistor R_{eq} of nonlinear element is only assumed to be constant but is not assigned any specific value. In this paper all the R_{eq} of nonlinearities are chosen to be 1 so as to make (2.10) and (2.12) to have similar form. As can be seen that if R_{eq}=1, then apart from the additional $I_l(t)$, the left hand side of (2.10) and (2.12) are exactly the same, and their right hand sides are all known items. Therefore, N_3 linear equations are developed and can be written as:

$$\mathbf{M}_{N_3\times N_3}\mathbf{I}_{N_3\times 1}=\mathbf{b}_{N_3\times 1}. \tag{2.13}$$

Each row of $\mathbf{M}_{N_3\times N_3}$ represents a current or voltage equation of one nonlinear element or pure voltage/current source. Coefficients of $\mathbf{M}_{N_3\times N_3}$ can be computed by doing row subtraction of matrix $\mathbf{A}_{N_1\times N_2}$. The only thing that one has to be aware of is that an additional 1 has to be added to the diagonals of $\mathbf{M}_{N_3\times N_3}$ if that row represents a current equation like (2.10). This means that the off-diagonal elements of matrix $\mathbf{M}_{N_3\times N_3}$ are always constant, the only time-varying part is its diagonal part.

As mentioned in Sec. III, some nonlinear elements always behave like either current or voltage source and will not transfer types during simulation. These include PV panel, batteries, some electric machines and pure voltage/current sources, etc. Other nonlinear elements, like semiconductor switches, will consistently transfer types between current and voltage sources. Therefore, $\mathbf{M}_{N_3\times N_3}$ can be partitioned into blocks and (2.13) can be rewritten as:

$$\begin{bmatrix}\mathbf{M}_{11} & \mathbf{M}_{12}\\ \mathbf{M}_{21} & \mathbf{M}_{22}\end{bmatrix}\begin{bmatrix}\mathbf{I}_1\\ \mathbf{I}_2\end{bmatrix}=\begin{bmatrix}\mathbf{b}_1\\ \mathbf{b}_2\end{bmatrix}, \tag{2.14}$$

where the upper equations represent the elements that will change types during simulation and the lower equations represent those that do not. This means $\mathbf{M}_{12}$, $\mathbf{M}_{21}$ and $\mathbf{M}_{22}$ are constant, and only the diagonal of $\mathbf{M}_{11}$ is time-varying. Using lower part of (2.14), $\mathbf{I}_2$ can be expressed as:

$$\mathbf{I}_2=-\mathbf{M}_{22}^{-1}\mathbf{M}_{21}\mathbf{I}_1+\mathbf{M}_{22}^{-1}\mathbf{b}_2. \tag{2.15}$$

Replacing $\mathbf{I}_2$ into the upper part of (2.14) using (2.15) yields the following system equations:

$$\left(\mathbf{M}_{11} - \mathbf{M}_{12}\mathbf{M}_{22}^{-1}\mathbf{M}_{21}\right)\mathbf{I}_1 = \mathbf{b}_1 - \mathbf{M}_{12}\mathbf{M}_{22}^{-1}\mathbf{b}_2. \tag{2.16}$$

Equation (2.16) is the core difficulty of solving the whole system states since this is the only process involving time-varying matrix. For the sake of convenience, in the remaining part of this paper, (2.16) will be denoted as:

$$\mathbf{MI} = \mathbf{b}, \tag{2.17}$$

where $\mathbf{M} = \mathbf{M}_{11} - \mathbf{M}_{12}\mathbf{M}_{22}^{-1}\mathbf{M}_{21}$ has time-varying diagonal and constant off-diagonal elements. $\mathbf{b} = \mathbf{b}_1 - \mathbf{M}_{12}\mathbf{M}_{22}^{-1}\mathbf{b}_2$ is known based on history information.

The following subsections provide three feasible methods for solving (2.17).

2.4.1 Solution by pre-computed inversion or factorization

When the dimension of M is small, it is very convenient to compute all the possible cases of M and store its inversion or factorization in memory. The corresponding computational complexity is constant. It has to be pointed out that this method is not necessarily only restricted to systems with very few elements. Some topologies, like MMC, are also suitable for this method. To demonstrate this, an important property is indicated and proved here—when a very small resistor lies in parallel or a very large resistor in series with the connecting route of two nonlinear elements, then the voltages and currents of these two nonlinear elements are almost decoupled. Since the equivalent resistor of inductor $(2L/\Delta t)$ is usually very large and the equivalent resistor of capacitor $(\Delta t/2C)$ is usually very small, this property is useful in application.

Assume that there is a very small resistor R_C lies in parallel with the route between two nonlinear elements, as shown in Fig. 2.6(a). The remaining part of the route is assembled in a two-port network and described by a $\mathbf{Y}$ matrix shown below:

$$\begin{bmatrix} I_1 \\ I_2 \end{bmatrix} = \begin{bmatrix} y_{11} & y_{12} \\ y_{21} & y_{22} \end{bmatrix} \begin{bmatrix} v_1 \\ v_2 \end{bmatrix}. \tag{2.18}$$

Then the following KCL equations can be developed:

$$\begin{bmatrix} \frac{1}{R_{NL1}} + \frac{1}{R_C} + y_{11} & y_{12} \\ y_{21} & \frac{1}{R_{NL2}} + y_{22} \end{bmatrix} \begin{bmatrix} v_1 \\ v_2 \end{bmatrix} = \begin{bmatrix} -I_{NL1} \\ -I_{NL2} \end{bmatrix}. \tag{2.19}$$

Solving (2.19), v_1, v_2 can be expressed as:

$$\begin{aligned} v_1 &= \frac{1}{\Delta}\left[-\left(\frac{1}{R_{NL2}}+y_{22}\right)I_{NL1}+y_{12}I_{NL2}\right], \\ v_2 &= \frac{1}{\Delta}\left[y_{21}I_{NL1}-\left(\frac{1}{R_{NL1}}+\frac{1}{R_C}+y_{11}\right)I_{NL2}\right], \end{aligned} \tag{2.20}$$

where Δ is the determinant of the matrix in (2.19),

$$\Delta = \left(\frac{1}{R_{NL1}}+\frac{1}{R_C}+y_{11}\right)\left(\frac{1}{R_{NL2}}+y_{22}\right)-y_{12}y_{21}. \tag{2.21}$$

Because R_C is very small, Δ is a very large value. Then the cross-coupling coefficients y_{12}/Δ and y_{21}/Δ in (2.20) are almost zero, which means I_{NL1} has negligible effect on v_2 and I_{NL2} has negligible effect on v_1. Thus, v_1 and v_2 are almost decoupled.

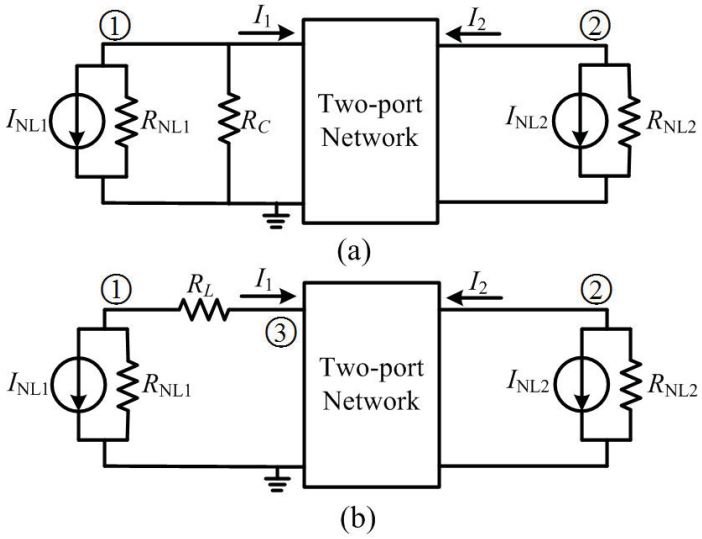

Figure 2.6: Two configurations of decoupling elements.

Similarly, when there is a very large resistor R_L that lies in series with the route between two nonlinear elements, as shown in Fig. 2.6(b). The following equations can be developed:

$$\begin{bmatrix} \frac{1}{R_{NL1}}+\frac{1}{R_L} & 0 & -\frac{1}{R_L} \\ 0 & \frac{1}{R_{NL2}}+y_{22} & y_{21} \\ -\frac{1}{R_L} & y_{12} & \frac{1}{R_L}+y_{11} \end{bmatrix} \begin{bmatrix} v_1 \\ v_2 \\ v_3 \end{bmatrix} = \begin{bmatrix} -I_{NL1} \\ -I_{NL2} \\ 0 \end{bmatrix}. \tag{2.22}$$

The cross-coupling coefficient between v_1 and I_{NL2} is $\frac{y_{12}}{\Delta}\frac{1}{R_L}$, and the cross-coupling coefficient between v_2 and I_{NL1} is $\frac{y_{21}}{\Delta}\frac{1}{R_L}$, where Δ is the determinant of the matrix

in (2.22). Because R_L is very large, Δ is a normal value while $\frac{1}{R_L}$ is almost zero. Thus, v_1 and v_2 are almost decoupled. It can also be concluded that the larger the values of L and C and the smaller the time-step, the higher the decoupling degree will be. This property does indeed coincide with the objective laws in real system—large inductors and capacitors are usually used to add inertia into the system and smaller time-steps will offer better precision. Actually, there are already some efforts in literature using the inductive and capacitive parts to decouple the circuits and they often explained it in physics. This subsection provides a way to explain in mathematics why inductive and capacitive parts can be used to decouple the circuits, and why inductive element should lie in series and capacitive element should lie in parallel with the decoupled sub-circuits.

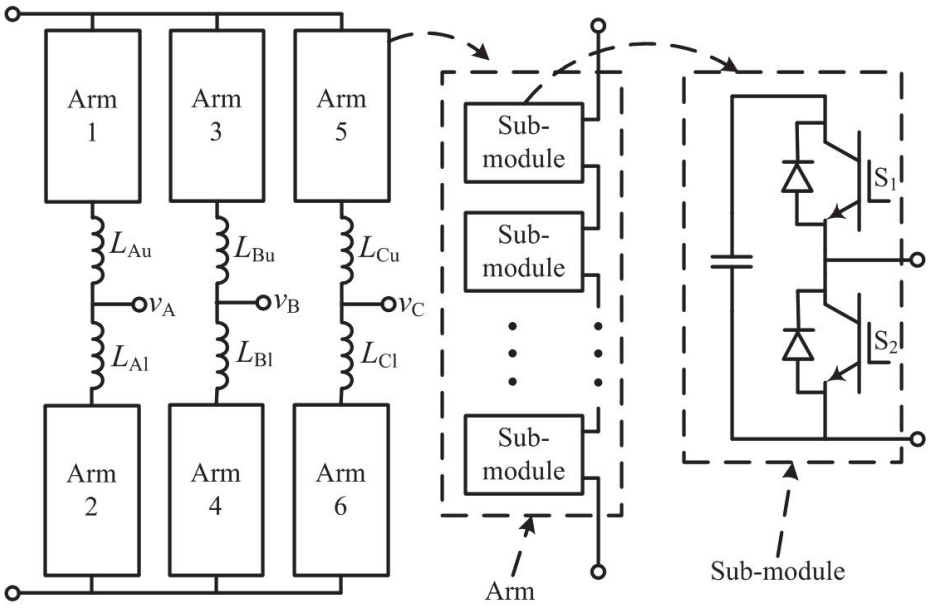

Figure 2.7: Structure of MMC topology.

The MMC topology has a very elegant structure, as shown in Fig. 2.7. A three-phase MMC has 6 arms, each arm has several submodules (SMs) and one arm inductor, and each submodule consists of one capacitor and two switches in a half bridge topology. The arm inductors are used to limit the circulating current within the converter. However, they also provide great facility in simulation. As can be seen in Fig. 2.7, the connecting route of any two submodules lies two series connected arm inductors, which means these submodules are almost decoupled from each other and can be dealt with separately. Since all the submodules in the MMC share the same 2×2 matrix $\mathbf{M}$, then it is very convenient to store its inversion or factorization in memory. This has been validated by the test case in

the subsequent section.

2.4.2 Solution by modified Gaussian elimination

The Gaussian elimination is always a competitive method for solving linear equations. (2.17) is no exception. However, considering that matrix M has constant off-diagonal elements, a modified Gaussian elimination method is provided which can reduce the computational complexity to a great extent. Assume that matrix M has an initial structure shown below:

$$\mathbf{M} = [m_{i,j}]_{N\times N}$$
$$\begin{bmatrix} v_{1,1} & c_{1,2} & c_{1,3} & \cdots & c_{1,N-2} & c_{1,N-1} & c_{1,N} \\ c_{2,1} & v_{2,2} & c_{2,3} & \cdots & c_{2,N-2} & c_{2,N-1} & c_{2,N} \\ c_{3,1} & c_{3,2} & v_{3,3} & \cdots & c_{3,N-2} & c_{3,N-1} & c_{3,N} \\ & \cdots & & & & \cdots & \\ c_{N-2,1} & c_{N-2,2} & c_{N-2,3} & \cdots & v_{N-2,N-2} & c_{N-2,N-1} & c_{N-2,N} \\ c_{N-1,1} & c_{N-1,2} & c_{N-1,3} & \cdots & c_{N-1,N-1} & v_{N-1,N-1} & c_{N-1,N} \\ c_{N,1} & c_{N,2} & c_{N,3} & \cdots & c_{N,N-2} & c_{N,N-1} & v_{N,N} \end{bmatrix}, \tag{2.23}$$

where v represents the variable, which has two possible vaules and c represents the constant. Unlike traditional Gaussian elimination, the first step of the modified method produces zeros in the last column using row 1 elements. After Step 1, matrix M becomes:

$$\mathbf{M}^{(1)} = [m^{(1)}_{i,j}]_{N\times N}$$
$$\begin{bmatrix} v_{1,1} & c_{1,2} & c_{1,3} & \cdots & c_{1,N-2} & c_{1,N-1} & c_{1,N} \\ v^{(1)}_{2,1} & v^{(1)}_{2,2} & c^{(1)}_{2,3} & \cdots & c^{(1)}_{2,N-2} & c^{(1)}_{2,N-1} & 0 \\ v^{(1)}_{3,1} & c^{(1)}_{3,2} & v^{(1)}_{3,3} & \cdots & c^{(1)}_{3,N-2} & c^{(1)}_{3,N-1} & 0 \\ & \cdots & & & & \cdots & \\ v^{(1)}_{N-2,1} & c^{(1)}_{N-2,2} & c^{(1)}_{N-2,3} & \cdots & v^{(1)}_{N-2,N-2} & c^{(1)}_{N-2,N-1} & 0 \\ v^{(1)}_{N-1,1} & c^{(1)}_{N-1,2} & c^{(1)}_{N-1,3} & \cdots & c^{(1)}_{N-1,N-1} & v^{(1)}_{N-1,N-1} & 0 \\ v^{(1)}_{N,1} & v^{(1)}_{N,2} & v^{(1)}_{N,3} & \cdots & v^{(1)}_{N,N-2} & v^{(1)}_{N,N-1} & 0 \end{bmatrix}, \tag{2.24}$$

where $m^{(1)}_{i,j} = m_{i,j} - m_{i,N}m_{1,j}/m_{1,N}$, for $2 \leqslant i \leqslant N$,$1 \leqslant j \leqslant N$. The constants in the first column and the last row become variables because of Step 1 elimination while the other constants are still constants but with another value.

Similarly, Step 2 produces zeros in the second last column using row 2 elements, then matrix $\mathbf{M}^{(1)}$ becomes:

$$\mathbf{M}^{(2)} = [m_{i,j}^{(2)}]_{N\times N}$$
$$\begin{bmatrix} v_{1,1} & c_{1,2} & c_{1,3} & \cdots & c_{1,N-2} & c_{1,N-1} & c_{1,N} \\ v_{2,1}^{(1)} & v_{2,2}^{(1)} & c_{2,3}^{(1)} & \cdots & c_{2,N-2}^{(1)} & c_{2,N-1}^{(1)} & 0 \\ v_{3,1}^{(2)} & v_{3,2}^{(2)} & v_{3,3}^{(2)} & \cdots & c_{3,N-2}^{(2)} & 0 & 0 \\ & \cdots & & & & \cdots & \\ v_{N-2,1}^{(2)} & v_{N-2,2}^{(2)} & c_{N-2,3}^{(2)} & \cdots & v_{N-2,N-2}^{(2)} & 0 & 0 \\ v_{N-1,1}^{(2)} & v_{N-1,2}^{(2)} & v_{N-1,3}^{(2)} & \cdots & v_{N-1,N-1}^{(2)} & 0 & 0 \\ v_{N,1}^{(2)} & v_{N,2}^{(2)} & v_{N,3}^{(2)} & \cdots & v_{N,N-2}^{(2)} & 0 & 0 \end{bmatrix}. \tag{2.25}$$

The constants in second column and second last row become variables while other constants remain constant. After $\lfloor (N+1)/2 \rfloor$ steps, structure of matrix $\mathbf{M}$ will be like the one shown in Fig. 2.8, where $\mathbf{P}$ is a $\lfloor (N+1)/2 \rfloor \times \lfloor (N+1)/2 \rfloor$ variable

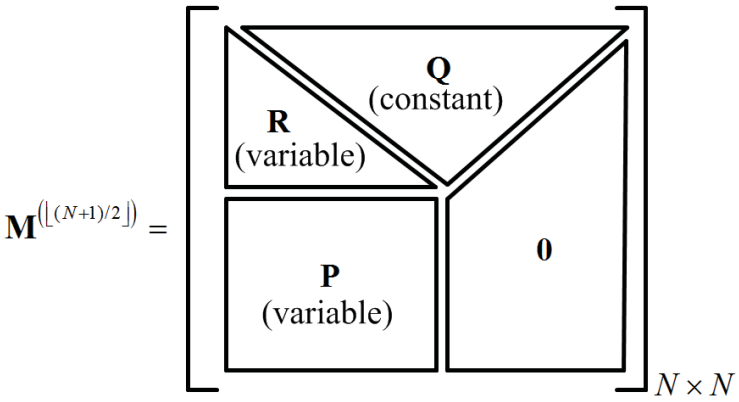

Figure 2.8: Structure of $\mathbf{M}$ after $\lfloor (N+1)/2 \rfloor$ steps.

matrix. Since the right half block of $\mathbf{M}^{(\lfloor (N+1)/2 \rfloor)}$ corresponding to $\mathbf{P}$ is all zeros, solving $\mathbf{P}$ using traditional Gaussian elimination can obtain the first $\lfloor (N+1)/2 \rfloor$ unknowns of $\mathbf{I}$. After this, substituting them into $\mathbf{Q}$ and $\mathbf{R}$, the other unknowns of $\mathbf{I}$ are also obtained. Note that the first $\lfloor (N+1)/2 \rfloor$ steps of the modified Gaussian elimination is quite simple and can be conducted in advance. It can be proven that every element of matrix $\mathbf{P}$ has at most 4 possible values, while element of matrix $\mathbf{R}$ has at most 2 possible values and matrix $\mathbf{Q}$ is constant. So it won't take much memory to store them.

Because the dimension of $\mathbf{P}$ is almost half of $\mathbf{M}$, and Gaussian elimination is a $O(N^3/3)$ problem, if the number of nodes is approximately equal to the number

of nonlinear elements, then the computation load corresponding to matrix $\mathbf{P}$ is approximately $1/8$ of that of traditional method, i.e, solving (3.1) using a time-varying $\mathbf{G}$. Considering that the system may be partitioned into several sub-blocks due to the property discussed in previous section, this number can be even smaller.

2.4.3 Solution by updating inverse using Sherman-Morrison formula

The Sherman-Morrison formula is a useful tool to update the inverse of an original matrix after a rank-1 modification [54]. Assume $\mathbf{u}$ is a column vector and $\mathbf{v}$ is a row vector, then the inverse of matrix $\mathbf{M} + \mathbf{uv}$ can be expressed as:

$$(\mathbf{M} + \mathbf{uv})^{-1} = \mathbf{M}^{-1} - \sigma \mathbf{M}^{-1}\mathbf{uv}\mathbf{M}^{-1}, \tag{2.26}$$

where σ is a scalar and $\sigma = 1/(1 + \mathbf{v}\mathbf{M}^{-1}\mathbf{u})$.

Considering that matrix $\mathbf{M}$ has variables only on diagonal, any two possible variations of $\mathbf{M}$ can be mutually transformed by a series of rank-1 modifications. The computational complexity of calculating the modified inverse $\mathbf{M}_1^{-1}$ from a base matrix $\mathbf{M}_0^{-1}$ is $O(mN^2)$, where m is the number of diagonals of $\mathbf{M}_1$ that differ from those of $\mathbf{M}_0$. If there are enough base matrices that have been computed and pre-stored in memory so that $m \leqslant \lfloor N/3 \rfloor$, then this method will have advantage over traditional Gaussian elimination method. Obviously, more base matrices reduce the computational complexity but require more memory space. It has to be pointed out that the actual diagonal combinations of $\mathbf{M}$ is far less than 2^N, for example, a $\mathbf{M}$ that consists of all voltage equations is most likely to be singular because the power electronic switches cannot all be switched on simultaneously. This will significantly reduce the memory storage demand.

Note that formula (2.26) may cause numerical error when $(1 + \mathbf{v}\mathbf{M}^{-1}\mathbf{u})$ is very small. This happens frequently because the diagonal elements of $\mathbf{M}^{-1}$ are often very close to ± 1. In the author's experience, when choosing the base matrix $\mathbf{M}_0$, it is better to select certain rows and add an additional 1 to the diagonal elements of current equation and subtract an additional 1 from the diagonal elements of voltage equation and leave the additional modified diagonal elements to be the last steps of Sherman-Morrison update process. This will avoid the numerical distortion in most cases.

The above three methods provide three perspectives to solve diagonal time-varying linear equations. However, they each has its own advantages and eligible

applications. When solving a new system, decoupling is always the first consideration. After the decoupling step, a proper method needs to be chosen. Generally speaking, pre-computed inversion or factorization is suitable for small size M; the Sherman-Morrison method is suitable for medium size; and the Gaussian elimination is suitable for large size. In addition, the Gaussian elimination is more suitable for sequential programs (like CPU based program) because of low computational complexity while the Sherman-Morrison method is more suitable for parallel programs (like FPGA based program) because the intermediate quantities do not depend on each other, thus in each process, the N^2 updating values can be calculated simultaneously, which makes the $O(mN^2)$ problem becomes $O(m)$ with respect to computation time.

Another important feature that has to be pointed out is that this method is always numerically stable, no matter what the nonlinearities are and how they connect with each other. This is because the equivalent representation of all the nonlinear elements has an internal resistor. Thus from the system point of view, it looks like to deal with a pure resistor network, the only time-varying part is the companion current source and the system itself does not have any instability risk.

2.5 Off-Line Simulation Validation

The MMC and NPC converters are two commonly used topologies in power electronic industry and will be used as two test cases to validate the proposed simulation method. The output waveforms and computation efficiency are compared with the existing system-level and device-level simulation tools—PSCAD/EMTDC® and SaberRD®.

2.5.1 Off-line simulation results of MMC

The MMC topology is an effective configuration to achieve high voltage and power using moderate switching devices. It is widely used in the high voltage direct current (HVDC) transmission systems around the world. For a long time, simulation of MMC topology behavior was a tough task because it has too many semiconductor switches in one converter. But using the proposed method, this task becomes comparatively easy because all the sub-modules in MMC are decoupled from each other in nature.

A three-phase five-level MMC is constructed and served as the test case and its parameters are listed in appendix Table A.1. The resulting waveforms of this five-

level MMC from PSCAD/EMTDC® and a C-program employing the proposed method are shown in Fig. 2.9. The companion current source of nonlinear elements are solved by pre-computed inversion, as discussed in Sec. 2.4.A. The modulation scheme adopted here is the phase-shift pulse width modulation (PS-PWM) with a displacement angle of 45° between upper and lower arm [55], [56]. As for the capacitor voltage, a combination of averaging and individual proportion-integration (PI) controllers are designed to achieve voltage balancing (see reference [57]). The DC-link voltage is set to soft start from 0 to rated value in 50 ms and the simulation time-step is 500 ns. Differences of these waveforms can barely be observed. Further calculations show that the total harmonic distortion (THD) of line-line voltage between A and B phase ($v_{\mathrm{A-B}}$) are 9.82% (PSCAD/EMTDC® results) and 9.81% (the proposed method results), respectively and THD of the load current of phase A (i_{A}) are both 1.25%. Two capacitor voltages, namely the upper most and lower most submodule of phase A leg (C_{A1} and C_{A8}), are selected to be drawn in Fig. 2.9. The mean square error (MSE) of $v_{C\mathrm{A1}}$ between these two simulation tools is 9.8189×10^{-7} and 9.8398×10^{-7} for $v_{C\mathrm{A8}}$. These values indicate that the output waveforms from PSCAD/EMTDC® and the proposed method based program are very close to each other.

The nonlinear element, i.e., the IGBT, is another major concern of the simulation accuracy. In PSCAD/EMTDC®, IGBT is modeled as a two-state resistance (R_{on} and R_{off}) and the switching on and off waveforms of an IGBT are shown in Fig. 2.10(a). As can be seen, in on state, the voltage across the IGBT's collector and emitter (v_{CE}) is always approximately to zero while in off state, the IGBT's collector current (i_{C}) is always approximately to zero and the switching transition between on/off states is accomplished in one time step. As a comparison, the proposed method based program also applies a simple switch model to imitate the ideal switch, namely treat the switch as a voltage source whose value is zero in on state and a current source whose value is zero in off state and no switching transient is assumed. The resulting waveforms are shown in Fig. 2.10(b). The nonlinear element behaviors from these two simulation tools are also very close and they both resemble the ideal switch.

The computational efficiency may be the most significant difference between these two tools. Execution time test is conducted between PSCAD/EMTDC® and the C-program. Because comparison between a general-purpose software and a specific C-program is not particularly fair, the following efforts have been made to make it fairer: (1) The compile process of the program is not included and only the

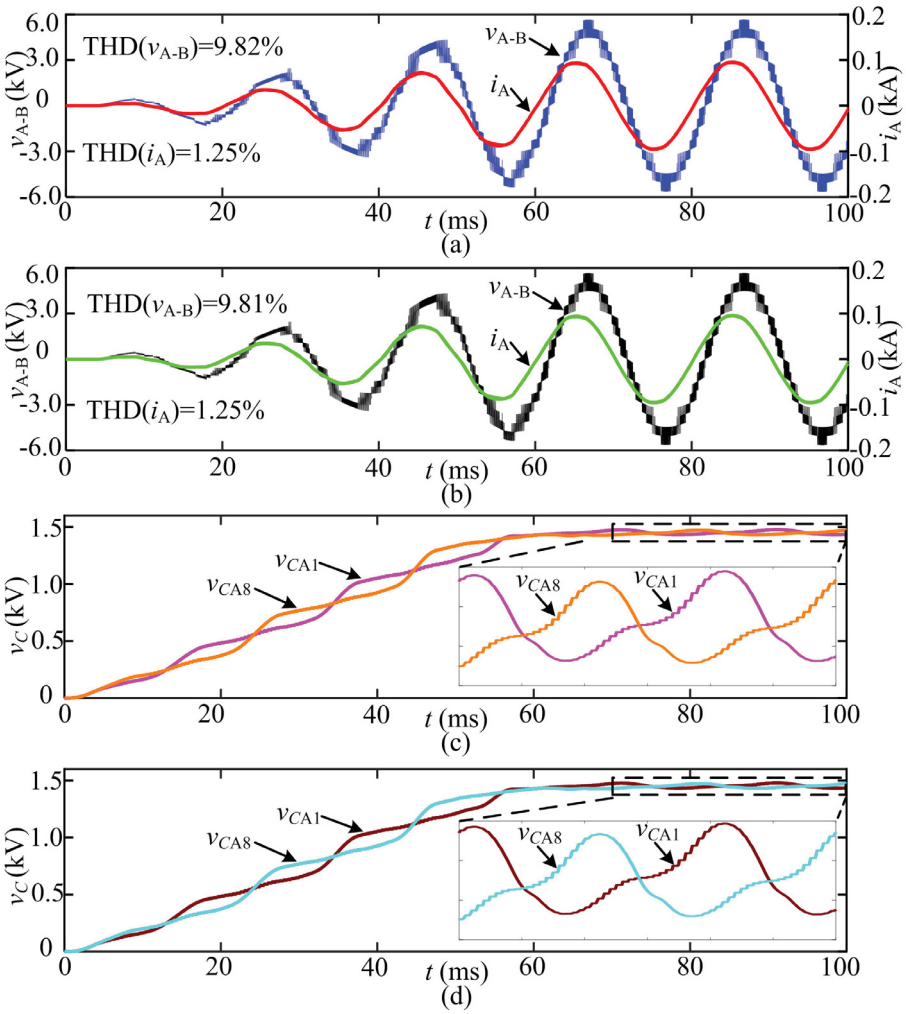

Figure 2.9: Comparison of a five-level MMC simulation waveforms between PSACD/EMTDC® and the proposed method based program. (a) Line-Line voltage ($v_{\mathrm{A-B}}$) and load current (i_{A}) waveforms from PSCAD/EMTDC®. (b) Counterparts of (a) from the proposed method based program. (c) Submodule capacitor voltage (V_{CA1} and V_{CA8}) waveforms from PSCAD/EMTDC®. (d) Counterparts of (c) from the proposed method based program.

execution time is accounted for; (2) When running the PSCAD/EMTDC model, no graphic output is added so as to avoid extra time for drawing figures; (3) The execution time for the C-program is measured in debug mode rather than in release mode. To conduct a 100 ms simulation using time-step of 500 ns on a computer with Intel i7-3770 processor, PSCAD/EMTDC® spends around 34 s while the proposed method based program only costs 3.361 s, which is approximately 10 times faster. This demonstrates that the proposed method has great advantage over traditional method in terms of computational efficiency while maintaining almost the

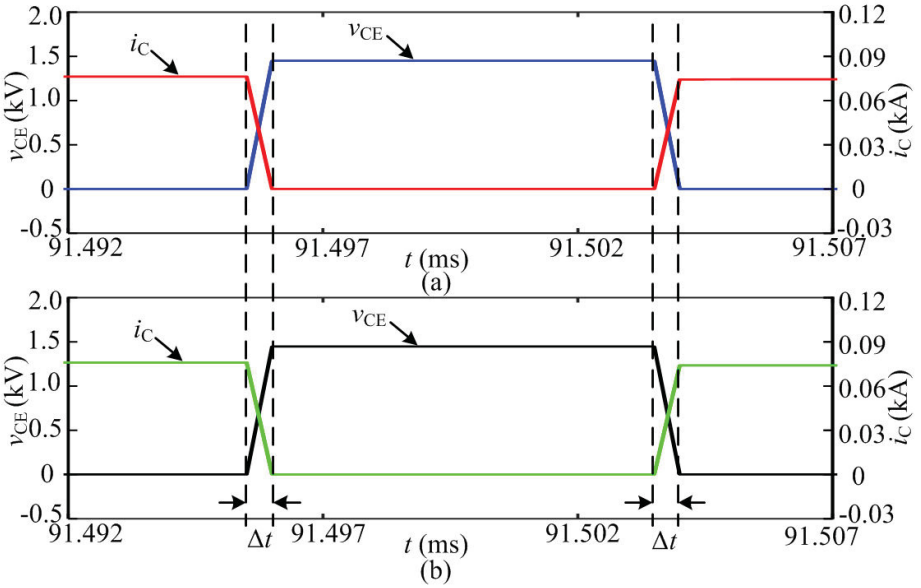

Figure 2.10: Comparison of switching on and off waveforms between PSCAD/EMTDC® and the proposed method based program. (a) PSCAD/EMTDC® results. (b) The proposed method based program results.

same accuracy. As the system includes more nonlinear elements, this advantage will become more significant.

2.5.2 Off-line simulation results of NPC

The NPC topology is another commonly used multi-level converter which is often applied in medium power circumstances and the three-level NPC converter is the most mature one. In this test case, a three-level NPC converter fed permanent magnet synchronous machine (PMSM) drive system is constructed. The configuration of the test setup and its equivalent circuit as well as the control scheme are illustrated in Fig. 2.11.

There are 12 nodes, 3 linear elements (one source and two capacitors) and 19 nonlinear elements (12 IGBTs, 6 diodes and 1 machine) in this system. Because the machine is a three-terminal element, it is represented by three resistors and the corresponding companion current sources. However, the three-phase currents of the machine are not independent, their sum is always zero which means there are only two degrees of freedom, thus one companion current source (I_{MC}) can be set to zero. Then, matrix **A** is 12×23 and **M** is 20×20. Among the 20 nonlinear elements, the IGBTs and diodes will transfer types during simulation while the machine will always be treated as a current source. This means, as in (2.14), **M** can

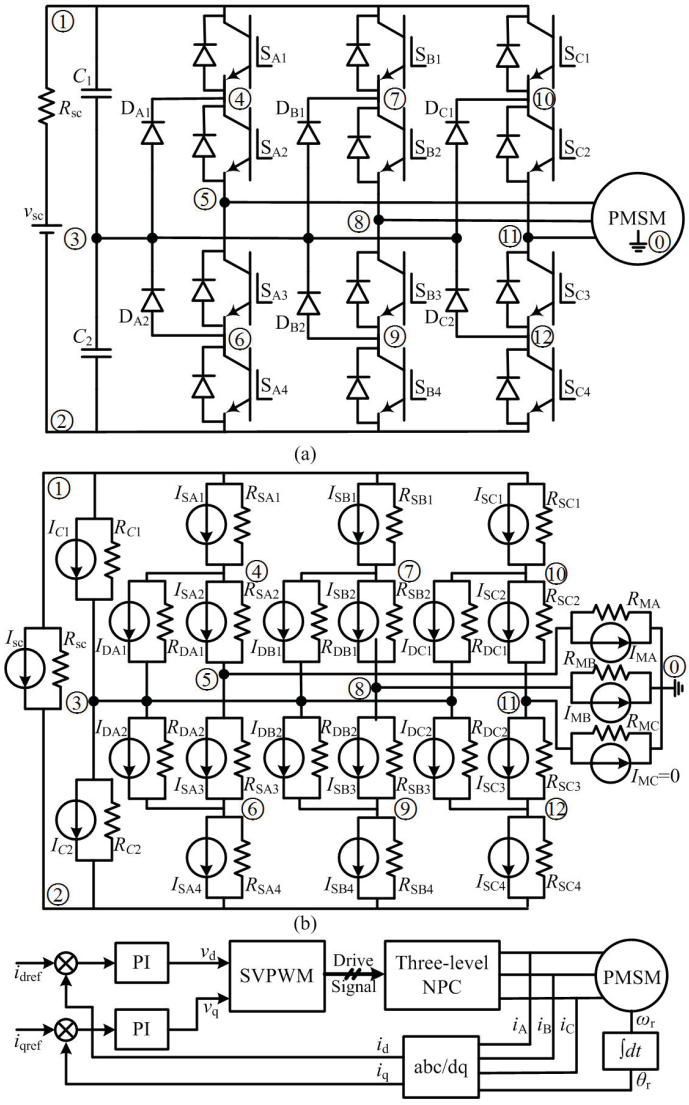

Figure 2.11: Configuration of the three-level NPC converter fed PMSM drive system. (a) Topology structure. (b) The equivalent circuit. (c) The control scheme.

be partitioned into a 18×18 $\mathbf{M_{11}}$ and a 2×2 $\mathbf{M_{22}}$. When applying matrix transformation as shown in (2.16), one would find that the 18×18 diagonal time-varying matrix is transformed into three identical 6×6 decoupling matrices. Each matrix represents one phase leg of the three-level NPC converter. It makes sense because the three-phase legs connect in parallel with the capacitor C_1 and C_2 whose equivalent resistor is very small. As explained in Sec. 2.4, a small resistor will decouple the sub-systems who connect in parallel with it. The decoupling nature of the nonlinear elements significantly reduces the computational burden. In this test case, the time-varying 6×6 matrix equations is solved by the modified Gaussian elimination method discussed in Sec. 2.4.B. Note that node 0 in Fig. 2.11 is a virtual

node which has no physical meaning. It only serves as a reference point and even if the stator windings of PMSM connect in wye type, the potential of node 0 is not equal to that of the neutral point of the wye configuration.

The parameters of the system are listed in appendix Table A.2. The PMSM model applied here is a fifth-order model that has three stator windings and two short-circuited damping windings.

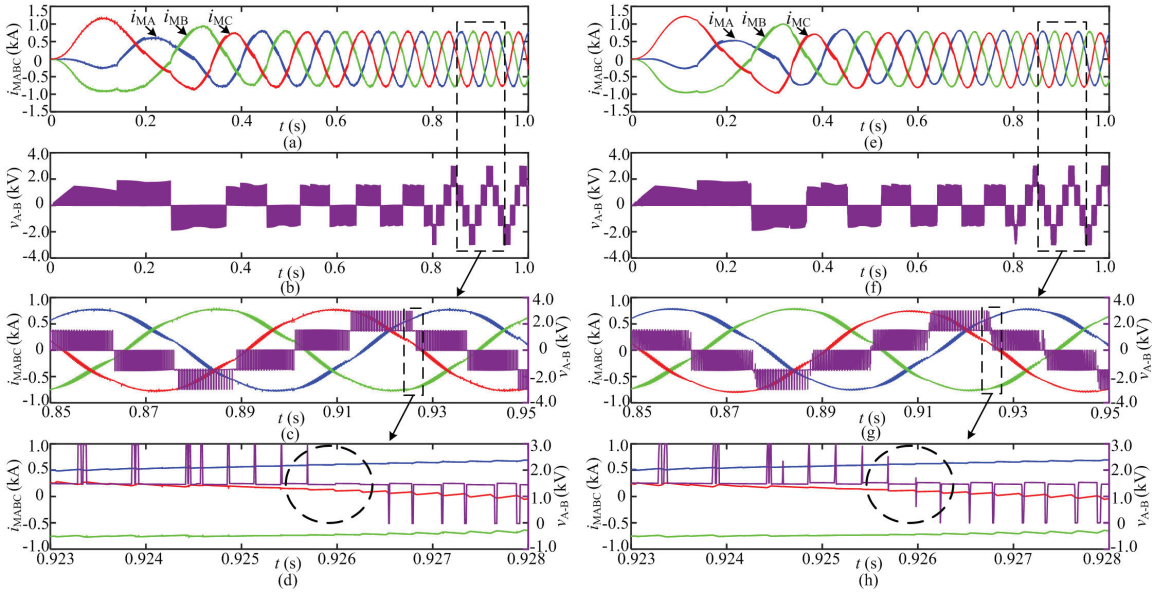

Figure 2.12: Comparison of three-level NPC-fed PMSM drive system start-up waveforms between PSCAD and the proposed method based program. (a) PMSM three phase stator current from PSCAD/EMTDC®. (b) NPC Line-Line voltage between phase A and B from PSCAD/EMTDC®. (c) Magnified waveforms of (a) and (b). (d) Magnified waveforms of (c). (e)-(h) Counterparts of (a)-(d) from the proposed method based program.

The output simulation waveforms of PSCAD/EMTDC® and the proposed method based C-program at the time-step of 200 ns are shown in Fig. 2.12. The machine is set to start-up at half load and the closed-loop space vector pulse width modulation (SVPWM) control strategy is employed where the d-axis current is tuned to zero and q-axis current is tuned to 1 kA. The differences of waveforms from these two simulation tools can hardly be distinguished. Only in very small time-scale scope, one can find the slight discrepancies, as denoted in the Fig. 2.12(d) and (h). This is because in PSCAD/EMTDC® the switch devices are simple $R_{\text{on}}/R_{\text{off}}$ model while in the new method based program, the realistic IGBT and diode switching characteristics are considered. Actually, the waveforms in Fig. 2.12(h) are more close to experimental results (see Fig. 8 in reference [58] and Fig. 9 in reference [59]). There are always voltage spikes during the voltage level transition and they are in-

deed caused by the switching transients of semiconductor devices.

To further validate the accuracy of the proposed method based program, the IGBT and diode switching transient waveforms in NPC are also recorded and compared with SaberRD® which has very sophisticated semiconductor models. The target IGBT and diode part number employed in simulation are FZ1500R33HL3 from Infineon® and VS-SD1053CS20L from Vishay®. The switching parameters of these two devices from data-sheet are listed in Table 2.2.

Table 2.2: Switching Parameters of IGBT and Diode

Parameter		**Datasheet**	**SaberRD®**	**Proposed method based program**
IGBT	Turn-on delay time ($t_{\mathrm{d(on)}}$)	0.50 μs	0.52 μs	0.54 μs
	Rise time (t_{r})	0.55 μs	0.53 μs	0.58 μs
	Turn-off delay time ($t_{\mathrm{d(off)}}$)	4.3 μs	4.3 μs	4.4 μs
	Fall time (t_{f})	0.40 μs	0.38 μs	0.42 μs
Diode	Reverse recovery time (t_{rr})	4.0 μs	4.0 μs	4.0 μs

The outcome switching transients from these two simulation tools are illustrated in Fig. 2.13 and the corresponding switching parameters are also shown in Table 2.2. As can be seen, the switching transients processes are highly non-linear and can take several micro seconds. Both these two simulation tools reproduced the switching transients properly. The key parameters ($t_{\mathrm{d(on)}}$, t_{r}, $t_{\mathrm{d(off)}}$, t_{f}, t_{rr}) are very close to that given in data-sheet. In this sense, the proposed method based program achieved comparable switching transients accuracy as with SaberRD®.

Again, the computational efficiency performance of these simulation tools differ greatly. To conduct a 1 s simulation of this NPC-fed PMSM drive system at the time step of 200 ns on a Intel i7-3770 processor computer platform, PSCAD/EMTDC® spends around 143 s while the proposed method based program only consumes 13.288 s—more than 10 times faster. As for the SaberRD®, it takes several hours to finish the same test set-up due to the complexity of its iterative algorithms and it utilizes the variable time-step [60], thus its computational efficiency is not compared here.

The above two test cases demonstrate that the method proposed in this paper is feasible in off-line simulation. It can give almost the same accuracy results of

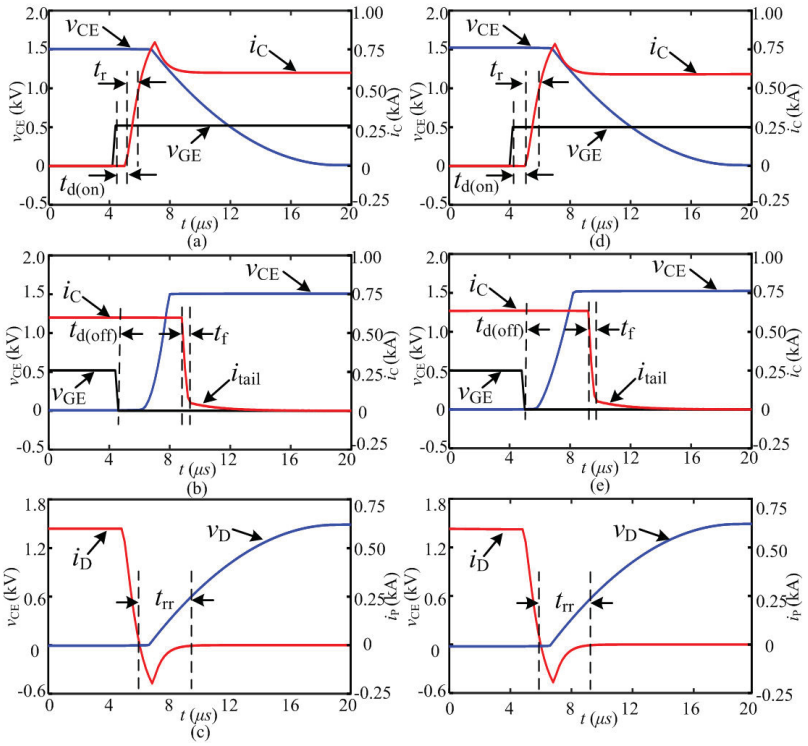

Figure 2.13: Comparison of switching transients between SaberRD® and new method based program. (a) IGBT turn-on transients from SaberRD®. (b) IGBT turn-off transients from SaberRD®. (c) Diode reverse recovery transients from SaberRD®. (d)-(f) Counterparts of (a)-(c) from the proposed method based program.

mature simulation software while spending far less execution time. In addition, this method has high generality. It can be applied to deal with most of (if not all) the nonlinearities in the major power electronic circuit topologies while retaining its high computational efficiency.

2.6 Real-Time Simulation Validation

Real-time simulation is widely accepted by industry engineers and designers as it has the ability to offer hardware-in-the-loop (HIL) tests which are more close to real applications compared with off-line simulation. In real-time simulation, the demand for computational efficiency is extremely high because it has to update the states of emulated system within every time-step. In most cases, real-time simulation is very hard to achieve and simplifications have to made to trade accuracy for speed. However, the method proposed in this paper lowers the computational burden while still retaining almost the same accuracy with traditional method.

This means it is very suitable for real-time simulation. In addition, the constant admittance matrix exploits the advantage of parallel computing to its full strength as every node voltage can be calculated independently and simultaneously.

In this section, the above two test cases are implemented in real-time on the Xilinx® Virtex UltraScale+VCU118-ES1 FPGA Evaluation Platform. The FPGA based real-time simulator has merits such as low cost, low hardware utilization, easy of maintenance, easy of reprogramming and high reliability. Because of the good generality of the proposed method, there is no special treatment of the circuit model itself like many other real-time simulation programs. Thus, the signal flow chart for these two test models is common and is given in Fig. 2.14. The whole project is divided into two parallel working modules: the control and the model module. The control module is designed to generate driving signals of semiconductor devices. Some of the common algorithms like coordinates transformation, PI controller, SVPWM and PWM generator are implemented here. The model module is responsible for updating the states of the simulated system and is partitioned into two sequential tasks: calculating the node voltages and calculating the companion current sources. The node voltages can be obtained by direct calculation using (2.6) or through LU factorization of (3.1). In the FPGA based program, the former is preferred although solving (3.1) has higher precision because (2.6) is more suitable for parallel programing and thus saves execution time; however, it is not always the case as it depends on the programmer and system sizing.

Calculation of the companion current sources is the key feature of this new method. It is partitioned into two successive processes—updating the states of linear and nonlinear elements. The linear elements will be dealt with first, either by Trapezoidal rule or Backward Euler rule or any other integration method. Trapezoidal rule is always stable and has an error term of $O((\Delta t)^3)$ while Backward Euler rule has simpler form but lower precision. The updating of nonlinear elements starts with judgment of them to be treated as current or voltage sources. The judgment condition can be from control signals or system states. After this step, the exact value of the equivalent current or voltage source is calculated in accordance with the nonlinear functions and a new matrix M is developed accordingly. Finally, the diagonal time-varying matrix equations is solved by either precomputed inversion or factorization or modified Gaussian elimination or updating inverse using the Sherman-Morrison formula. The selection of algorithm depends on many factors, especially the system sizing as discussed in Sec. 2.4. Considering that the program is implemented on the FPGA board, the first and third methods

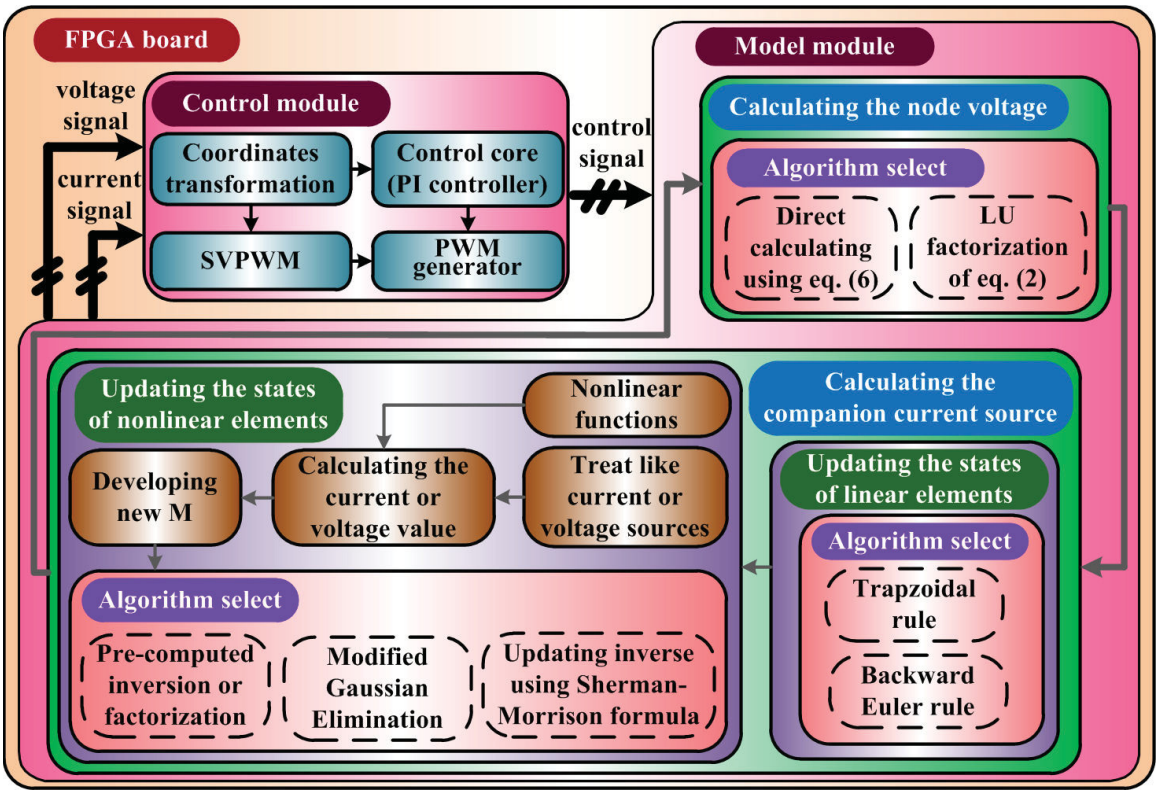

Figure 2.14: Signal flow chart of the proposed method implemented on FPGA.

will have higher priority. In the two test cases that are considered here, the MMC model will use pre-computed inversion and the NPC-fed PMSM drive model will employ updating inverse by the Sherman-Morrison formula.

2.6.1 Real-time simulation results of MMC

As discussed in Sec. 2.4, the matrix M in MMC model is 2×2 and has only two possible variations corresponding to upper switch on lower switch off mode, and upper switch off lower switch on mode, respectively. Therefore, the process of updating the states of nonlinear elements is easy as these two possible M matrices are pre-computed and stored in memory. The only challenge comes from calculating the node voltages. Because MMC topology has many switches, the matrix **A** in (2.6) has a size of 53×82 for a five-level topology. If they are implemented fully parallel in FPGA, more than 4000 multipliers are needed and each multiplier will consume several DSP blocks which is unbearable for the existing FPGA board. To reduce the hardware consumption, several techniques are adopted here:

1) The data format employed in this test case is the 59-bit fixed point number to

guarantee lower DSP blocks consumption and efficient precision as well. Although the 59×59 fixed point multiplication has to use 10 DSP blocks which is higher than double-precision floating point format, the addition of fixed point numbers is much simpler than floating point numbers. Thus, the overall hardware consumption is reduced.

2) The calculation process of each node voltage which involves 82 multiplications and 81 additions is partitioned into 4 groups to deal with 19, 20, 21, 22 multiplications, respectively. Each group is instantiated by a multiply-accumulate module. This means each multiplier is reused about 20 times and more importantly, the pipe-line technique is included.

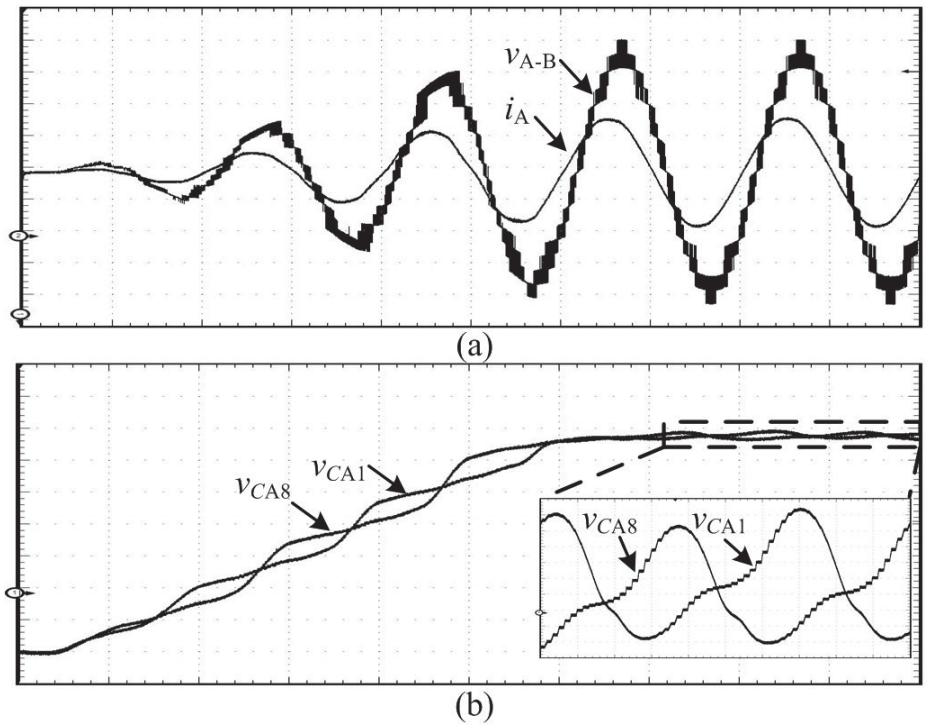

Figure 2.15: Real-time implementation waveforms of the five-level MMC system. (a) Ch1: Line-Line voltage ($V_{\mathrm{A-B}}$), y-axis: 1.5 kV/div. Ch2: load current (i_{A}) waveforms, y-axis: 0.5 kA/div, x-axis: 10 ms/div. (b) Submodule capacitor voltage (Ch1: V_{CA1} and Ch2: V_{CA8}) waveforms, y-axis:0.2143 kV/div, x-axis: 10 ms/div.

With the help of these techniques, the 500 ns time-step real-time simulation of the five-level MMC test case discussed in Sec. V.A is realized. The system clock implemented is 100 MHz which means every time step the state updating is accomplished within 50 system clocks. The hardware utilization and real-time implementation waveforms are illustrated in Table 2.3 and Fig. 2.15, respectively. The results are almost the same with off-line waveforms except they are real-time.

Table 2.3: Hardware utilization of the five-level MMC model

Resource	LUT	FF	BRAM	DSP
Utilization	582115 (49.24%)	211466 (8.94%)	37.5 (1.74%)	2140 (31.3%)

2.6.2 Real-time simulation results of NPC

The NPC-fed PMSM drive system experienced a much simpler node voltage calculation process as its system size is much smaller. What should be paid attention to is solving the diagonal time-varying matrix equations. As analyzed in Sec.V.B, M is 6×6, but the possible variations of M is much smaller than 2^6, actually there are only 4 variations representing 4 possible switching combinations of one phase leg, as indicated in Fig. 2.16. Note that there is no need to worry about the switching pair dead-time as the dead-time modes are already included in the above 4 possible modes.

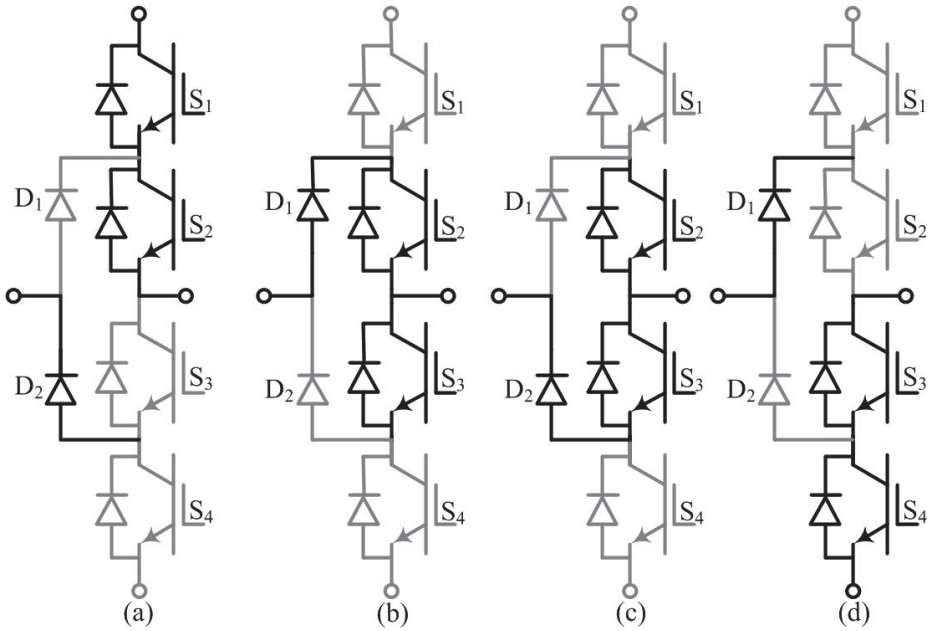

Figure 2.16: Four possible switching combinations of three-level NPC phase leg. Dark color represents switch-on, gray color represents switch-off. (a) Output positive voltage level; (b) Output neutral voltage level and load current is positive; (c) Output neutral voltage level and load current is negative; (d) Output negative voltage level.

Observing the four possible switching combinations, mode (a) and (c) have 4 same switches (S_2, S_4, D_1, D_2) and 2 different switches (S_1, S_3); mode (b) and (d) have 4 same switches (S_1, S_3, D_1, D_2) and 2 different switches (S_2, S_4). Thus modes

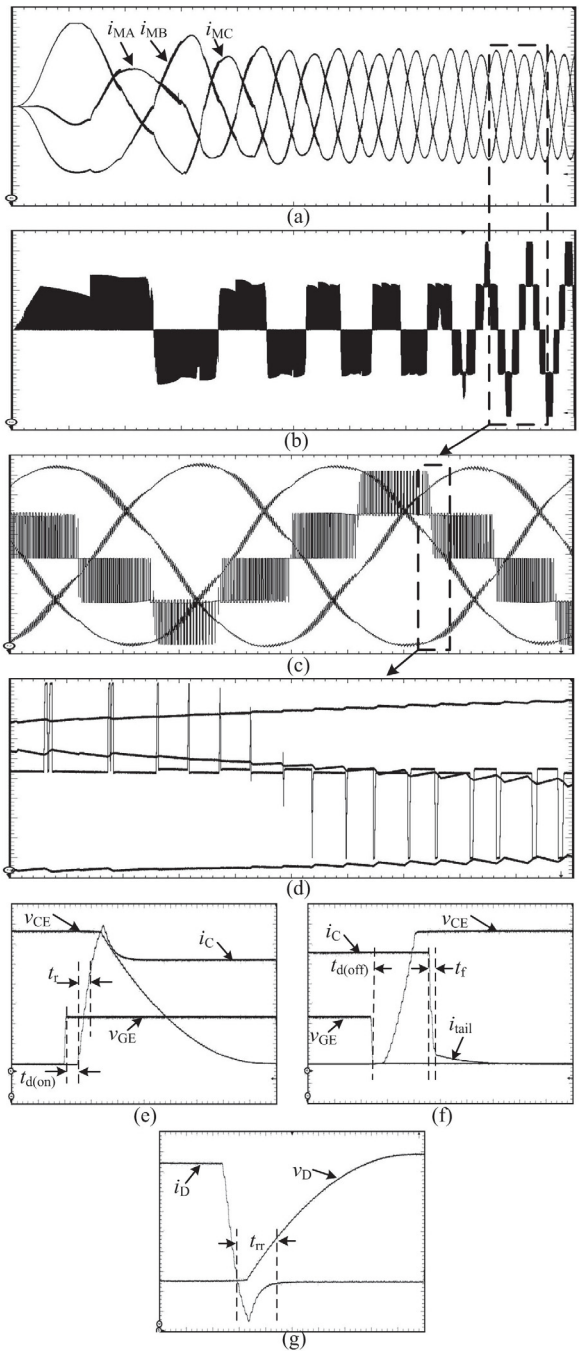

Figure 2.17: Real-time implementation waveforms of the three-level NPC fed-PMSM system. (a) Ch1: PMSM Phase A current (i_{MA}), Ch2: PMSM Phase B current (i_{MB}), Ch3: PMSM Phase C current (i_{MC}), y-axis: 0.3 kA/div, x-axis: 0.1 s/div. (b) NPC Line-Line voltage between phase A and B, y-axis: 0.7143 kV/div, x-axis: 0.1 s/div. (c) Magnified waveforms of (a) and (b), Ch1-Ch3: y-axis: 0.18 kA/div, Ch4: y-axis: 0.7143 kV/div, x-axis: 0.01 s/div. (d) Magnified waveforms of (c), Ch1-Ch3: y-axis: 0.17 kA/div, Ch4: y-axis: 0.33 kV/div, x-axis: 0.5 ms/div. (e)-(f) IGBT turn-on and turn-off transients, Ch1: V_{CE}, y-axis: 0.25 kV/div, Ch2: i_{C}, y-axis: 0.125 kA/div, Ch3: V_{GE}, y-axis: 5 V/div, x-axis: 2 μs/div. (g) Diode reverse recovery transients. Ch1: y-axis: 0.1 kA/div, Ch2: 0.24 kV/div x-axis: 2 μs/div.

(b) and (c) can be served as the base matrices in the Sherman-Morrison formula updating process. From mode (c) to mode (a) and from mode (b) to mode (d) only takes two updating processes. Furthermore, in order to accelerate the renewal of system states in every time-step, the Sherman-Morrison updating process is not included in the main sequential computation loop of system states in the model module, but rather works in parallel with the main loop just like the control module. This means, whenever there is a new mode coming, the control module will be responsible for updating the new inverse of matrix M. It is when the new inverse of matrix M is ready that the new mode will take effect. This kind of operation will introduce some delay in the control loop, however, considering that there is always real delay (approximately half the carrier period of switching devices) in power electronic converter control and the introduced Sherman-Morrison updating process delay is less than 1 μs, which is much smaller than half the carrier period, the resulting effect is negligible. In this arrangement, the NPC-fed PMSM drive system achieved 200 ns time-step on the 100 MHz system clock FPGA board. The resulting hardware utilization is summarized in Table 2.4 and the real-time implementation waveforms are shown in Fig. 2.17.

Table 2.4: Hardware utilization of the three-level NPC model

Resource	LUT	FF	BRAM	DSP
Utilization	125418 (10.61%)	98601 (4.17%)	106 (4.91%)	998 (14.59%)

2.7 Summary

This chapter provided a new perspective to deal with nonlinearities in a fast and stable manner in power electronic circuit simulation. The proposed method utilizes a uniform representation to substitute the nonlinearities in order to keep the system admittance matrix constant. The nonlinear elements then can be further viewed as current or voltage sources according to their nature or system states and the corresponding current or voltage equations are developed accordingly. Therefore, the computational difficulty is transformed to solve a diagonal time-varying matrix equation. Three methods are provided for solving it, which can cover most circumstances that are encountered in practical applications. The off-line and real-time test cases validated the feasibility of this new method and also demonstrated

its fast simulation speed. In addition, the proposed method has very good generality: it can be used to deal with most nonlinearities in major power electronic topologies while achieving comparable accuracy as with the mature simulation software at both the system-level and device-level. This method can be a good alternative algorithm to accelerate the speed in power electronic circuit simulation and it is also suitable to be made into a drag and drop tool incorporated with existing commercial softwares.

3

Modeling Methodology and Mathematic Analysis of EZM

3.1 Introduction

Chapter 2 presented an idea of modeling nonlinearities as a fixed value resistor in parallel with a current source. It still can be viewed as the application of nodal analysis method because it obeys all the modeling rules of nodal analysis method. The only difference is that the values of nonlinearities's equivalent resistors are set to be 1. Actually, the current or voltage values of these nonlinearities are predicted and the program makes much effort to find the solution of the companion current source so as to make the current or voltage value of the nonlinearities the same with the predicted values. However, the job of simulation program is to find the current and voltage values of every element in the circuit at every time-step. If the current or voltage values of the nonlinearities are already known by prediction, why not simply view them as current or voltage sources in the circuit and skip the solution process of companion current sources? This could save a lot computation time. Along with this idea, why not view all the elements (including linearities and nonlinearities) as current or voltage sources and solve the current-voltage relation in the circuit? The problem then becomes how to find the current-voltage relation of all elements in the circuit.

Generally speaking, the current-voltage relation of a circuit contains only ideal

sources is not easy to find. There are some basic rules that have to follow. For example, if there are some ideal voltage sources form a loop or some ideal current sources connect to a common node in the circuit, then mathematic contention may occur because the sum of these ideal voltage or current sources may not be zero. Even if there is no such contention in the circuit, there may be current-voltage source type transition during simulation for some elements like the power electronic switching devices. Therefore, some special algorithms or even circuit lemma are desirable to find the current-voltage relation efficiently. Actually, the idea used to model nonlinearities in chapter 2 provides a good way to identify current-voltage relation of a general circuit. If all the elements in the circuit are replaced by a resistor in parallel with a companion current source and set the resistor value to be 1, something interesting can be found. The current-voltage relation can be described by an antisymmetric matrix and this is exactly the foundation of EZM modeling methodology.

This chapter presents the proving process of a current-voltage relation lemma and modeling methodology of EZM based on this circuit lemma. The relation between EZM model and state-space model is also explained where a method to transform EZM model into state-space model is provided.

3.2 EZM Modeling Methodology

The EZM modeling methodology is based on a circuit lemma that indicates the relationship of branch voltages and currents in the circuit.

Lemma 1: Given a circuit that has n nodes and b branches, there exist n-1 individual branch voltages so that the other b-n+1 branch voltages can be expressed as simply addition or subtraction of these n-1 voltages. Meanwhile, these n-1 branch currents can be expressed as simply addtion or substraction of the b-n+1 branch currents. In addition, when written in matrix form, this matrix is an antisymmetric matrix.

The author would like to give an example first to exemplify this lemma and then prove it. The topology of Fig. 3.1 is taken from a commonly used power electronic circuit named Neutral Point Clamped (NPC) topology and this is a half bridge configuration. There are 6 nodes denoted from n_0 to n_5 and 9 branches denoted as b_1 to b_9.

Fig. 3.1(a) shows one possible working mode of this circuit where switches b_2 and b_3 are in on-state while switches b_1 and b_4 are in off-state. Meanwhile, the

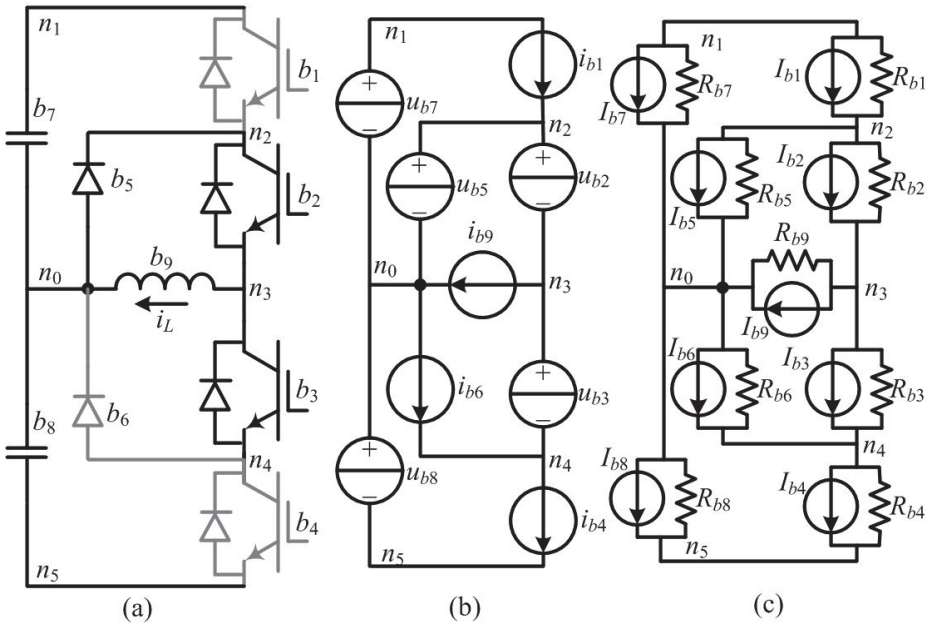

Figure 3.1: NPC half bridge topology. (a) Working mode. (b) Voltage/current source equivalent configuration. (c) Resistor companion current source equivalent configuration.

current of inductor b_9 flows from n_3 to n_0, which makes diode b_5 in on-state and b_6 in off-state.

As is well known that the circuit topology can be expressed as node-branch incidence matrix or loop-branch incidence matrix. However the nodes in the circuit are unique while loops are not (in other words, there is only one node-branch incidence matrix while there are multiple loop-branch incidence matrices). This is why most simulation programs favor nodal analysis and take node voltages as computation variables, rather than Thévenin analysis and solving loop currents. The core value of Lemma 1 is providing a way to find the relationship of branch currents by simple manipulation of node-branch incidence matrix, so that the program can get rid of some complex graph concepts like trees. The following process shows how to obtain the current relationship in Fig. 3.1 by use of Lemma 1.

Step 1: Write the node-branch incidence matrix $\mathbf{A}$,

$$\mathbf{A} = \begin{bmatrix} 0 & 0 & 0 & 0 & -1 & 1 & -1 & 1 & -1 \\ 1 & 0 & 0 & 0 & 0 & 0 & 1 & 0 & 0 \\ -1 & 1 & 0 & 0 & 1 & 0 & 0 & 0 & 0 \\ 0 & -1 & 1 & 0 & 0 & 0 & 0 & 0 & 1 \\ 0 & 0 & -1 & 1 & 0 & -1 & 0 & 0 & 0 \\ 0 & 0 & 0 & -1 & 0 & 0 & 0 & -1 & 0 \end{bmatrix}. \tag{3.1}$$

The node-branch incidence matrix is formed in such a way that the rows and columns of $\mathbf{A}$ correspond to the nodes and branches in the topology, respectively. The entry of $\mathbf{A}(a_{ij})$ is 1 when node i connects to branch j's positive end; and is -1 when they interconnect at branch j's negative end. When they have no connection in the topology, then $\mathbf{A}(a_{ij})$ is 0.

Step 2: Classify the b branches and select n-1 branches as voltage sources and others as current sourcres. In Fig. 3.1, b_2, b_3, b_5, b_7, b_8 are suitable to be taken as voltage sources while b_1, b_4, b_6 and b_9 are suitable to be taken as current sources, as shown in Fig. 3.1(b). Then split matrix $\mathbf{A}$ into two sections which correspond to the n-1 voltage sources ($\mathbf{A_1}$) and b-n+1 current sources ($\mathbf{A_2}$), respectively. Before doing this, delete one row of matrix $\mathbf{A}$ since the rows of $\mathbf{A}$ are not independent. The choice of deleted row is arbitrary. However, it is better to choose a node which has voltage source connected to it. In this example, row 1 which corresponds to node n_0 is deleted.

$$\mathbf{A}_1 = \begin{bmatrix} 0 & 0 & 0 & 1 & 0 \\ 1 & 0 & 1 & 0 & 0 \\ -1 & 1 & 0 & 0 & 0 \\ 0 & -1 & 0 & 0 & 0 \\ 0 & 0 & 0 & 0 & -1 \end{bmatrix}, \mathbf{A}_1 = \begin{bmatrix} 1 & 0 & 0 & 0 \\ -1 & 0 & 0 & 0 \\ 0 & 0 & 0 & 1 \\ 0 & 1 & -1 & 0 \\ 0 & -1 & 0 & 0 \end{bmatrix}. \tag{3.2}$$

Step 3: Do matrix manipulation so as to find the voltage relationships in Lemma

1.

$$\begin{bmatrix} u_{b1} \\ u_{b4} \\ u_{b6} \\ u_{b9} \end{bmatrix} = \mathbf{A}_2'(\mathbf{A}_1')^{-1} \begin{bmatrix} u_{b2} \\ u_{b3} \\ u_{b5} \\ u_{b7} \\ u_{b8} \end{bmatrix} = \begin{bmatrix} 0 & 0 & -1 & 1 & 0 \\ -1 & -1 & 1 & 0 & 1 \\ 1 & 1 & -1 & 0 & 0 \\ -1 & 0 & 1 & 0 & 0 \end{bmatrix} \begin{bmatrix} u_{b2} \\ u_{b3} \\ u_{b5} \\ u_{b7} \\ u_{b8} \end{bmatrix}. \tag{3.3}$$

where $\mathbf{A}_1'$ is the transpose of $\mathbf{A_1}$, and is the same for other matrices.

Step 4: Rewrite (3.3) into full $b \times b$ matrix form and using the antisymmetry property in Lemma 1 to supplement the section that indicates currents' relationship.

$$\begin{bmatrix} u_{b1} \\ i_{b2} \\ i_{b3} \\ u_{b4} \\ i_{b5} \\ u_{b6} \\ i_{b7} \\ i_{b8} \\ u_{b9} \end{bmatrix} = \begin{bmatrix} 0 & 0 & 0 & 0 & -1 & 0 & 1 & 0 & 0 \\ 0 & 0 & 0 & 1 & 0 & -1 & 0 & 0 & 1 \\ 0 & 0 & 0 & 1 & 0 & -1 & 0 & 0 & 0 \\ 0 & -1 & -1 & 0 & 1 & 0 & 0 & 1 & 0 \\ 1 & 0 & 0 & -1 & 0 & -1 & 0 & 0 & -1 \\ 0 & 1 & 1 & 0 & -1 & 0 & 0 & 0 & 0 \\ -1 & 0 & 0 & 0 & 0 & 0 & 0 & 0 & 0 \\ 0 & 0 & 0 & -1 & 0 & 0 & 0 & 0 & 0 \\ 0 & -1 & 0 & 0 & 1 & 0 & 0 & 0 & 0 \end{bmatrix} \begin{bmatrix} i_{b1} \\ u_{b2} \\ u_{b3} \\ i_{b4} \\ u_{b5} \\ i_{b6} \\ u_{b7} \\ u_{b8} \\ i_{b9} \end{bmatrix}. \tag{3.4}$$

In (3.4), the section in blue indicates the voltage relationship and can be obtained directly from (3.3). The section in red indicates the current relationship in the circuit and is obtained by antisymmetric supplement. There is no need to analyze loop-branch incidence matrix anymore.

The proof of Lemma 1 can be conducted by use of duality principle. However, this will make the proving process complicated. This chapter provides a new approach of proof which is easy to understand.

Proof: First, replace all voltage and current sources with a uniform representation which has a constant resistor in parallel with a companion current source, as shown in Fig. 3.1(c). Then every branch voltage can be written as a linear combination of those companion current sources. Because the resistors in the network are constants, the coefficients of those linear combinations are also constants.

Second, set the value of all resistors to be 1 and write the following matrix equation:

$$\mathbf{u}_b = \mathbf{M}_1 \mathbf{I}_b, \tag{3.5}$$

where $\mathbf{u}_b$ is branch voltage vector, $\mathbf{I}_b$ is companion current source vector, $\mathbf{M}_1$ is a $b \times b$ constant symmetric matrix. Analyze the relationship of branch voltage and current, the following equation can be written:

$$i_{bx} = u_{bx}/R_{bx} + I_{bx}, \tag{3.6}$$

where x is the index number of branch. Because the value of all resistors in the network is 1, (3.6) can be written as:

$$i_{bx} = u_{bx} + I_{bx}. \tag{3.7}$$

Then the branch current vector can be expressed as:

$$\mathbf{i}_b = \mathbf{M}_2 \mathbf{I}_b. \tag{3.8}$$

Matrix $\mathbf{M}_1$ and $\mathbf{M}_2$ have very similar form; their off-diagonal elements are the same and their diagonal elements differ by 1, or in matrix form:

$$\mathbf{M}_2 = \mathbf{M}_1 + \mathbf{I}, \tag{3.9}$$

where $\mathbf{I}$ is identity matrix.

Third, reorder the index of branch number so that the first *n*-1 branches are voltage sources and the latter *b*-*n*+1 branches are current sources. Then the following matrix equation can be obtained.

$$\begin{bmatrix} u_{b(n-1))} \\ i_{b(b-n+1))} \end{bmatrix} = \mathbf{M}\mathbf{I}_b, \tag{3.10}$$

where the first *n*-1 rows of $\mathbf{M}$ are the same with the first *n*-1 rows of $\mathbf{M}_1$, the last *b*-*n*+1 rows of $\mathbf{M}$ are the same with the last *b*-*n*+1 rows of $\mathbf{M}_2$. It is obvious that $\mathbf{M}$ is also a symmetric matrix since it differs with $\mathbf{M}_1$ and $\mathbf{M}_2$ only on diagonal elements.

Fourth, invert matrix $\mathbf{M}$ and (3.10) can be rewritten as:

$$\mathbf{I}_b = \begin{bmatrix} \mathbf{M}_{11}^{-1} & \mathbf{M}_{12}^{-1} \\ \mathbf{M}_{21}^{-1} & \mathbf{M}_{22}^{-1} \end{bmatrix} \begin{bmatrix} u_{b(n-1))} \\ i_{b(b-n+1))} \end{bmatrix} = \mathbf{M}^{-1} \begin{bmatrix} u_{b(n-1))} \\ i_{b(b-n+1))} \end{bmatrix}. \tag{3.11}$$

Equation (3.11) reveals that the companion current source vector $\mathbf{I}_b$ can also be expressed by the selected *n*-1 voltage sources and *b*-*n*+1 current sources. More importantly, the companion current source of every branch is simply the difference of branch current and voltage, as shown below:

$$I_{bx} = i_{bx} - u_{bx}, \tag{3.12}$$

which means (3.11) has a similar form with (3.4). Let's denote the matrix in (3.4) as $\mathbf{T}$ and the reordered form (where the first *n*-1 rows represent current relation and the last *b*-*n*+1 rows represent voltage relation) as $\bar{\mathbf{T}}$. To convert from $\bar{\mathbf{T}}$ to $\mathbf{M}^{-1}$, let's consider in this way: for the *n*-1 voltage sources, their current value i_{bx} can be obtained by $\bar{\mathbf{T}}$, when placing one additional -1 on the diagonals of $\mathbf{M}_{11}^{-1}$ and placing these $\bar{\mathbf{T}}$ elements in $\mathbf{M}_{12}^{-1}$, their companion current sources I_{bx} are obtained; for the *b*-*n*+1 current sources, their voltage value u_{bx} can be obtained by $\bar{\mathbf{T}}$, when multiplying -1 with these $\bar{\mathbf{T}}$ elements and placing them in $\mathbf{M}_{21}^{-1}$ and placing one additional 1 on the diagonals of $\mathbf{M}_{22}^{-1}$, their companion current sources I_{bx} are obtained. As mentioned previously, matrix $\mathbf{M}$ is a symmetric matrix and so does $\mathbf{M}^{-1}$, then $\mathbf{M}_{12}^{-1}$=$(\mathbf{M}_{21}^{-1})'$ and $\bar{\mathbf{T}} = -\bar{\mathbf{T}}'$. That is where the antisymmetry of matrix $\mathbf{T}(\bar{\mathbf{T}})$ comes from.

It has to be mentioned that the reordering operation in step 3 is not necessary in the proving process and will not affect the antisymmetry of $\mathbf{T}(\bar{\mathbf{T}})$. The only reason for doing so is for better understanding. This proving process can be applied to any circuit topology, so Lemma 1 is a general rule.

Based on the above analysis, the EZM modeling methodology takes branch voltage or current as the computational variables. Given a circuit that has *n* nodes and *b* branches, EZM always selects *n*-1 branches and takes their voltages as system variables, and takes the remaining *b*-*n*+1 branches's currents as system variables. The updating of system variables can be divided into two interleaved processes: (1) Advancing the system variables according to components' characteristics; (2) Taking into account the influence of the system network. The working principle of EZM can be illustrated in Fig. 3.2.

For the *n*-1 voltage source branches, they feed the network with their voltages and the network solver feeds them back with current values; for the *b*-*n*+1 current source branches, they feed the network with their currents and the network solver feeds them back with voltage values. This work is accomplished by using of Lemma 1. As can be seen, once matrix $\mathbf{T}$ is developed, the feedbacks of network is just simply addition/subtraction of the input system variables. The components

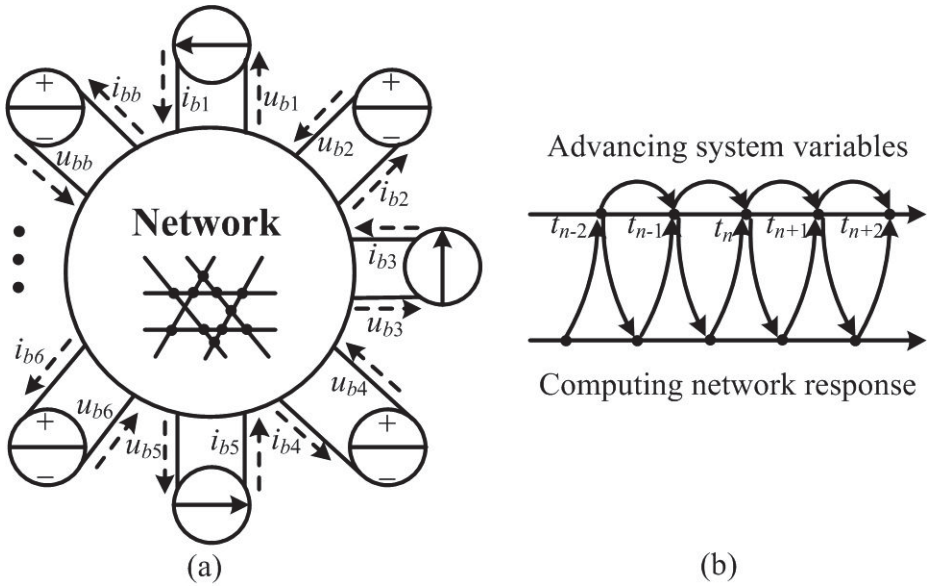

Figure 3.2: EZM's working principle. (a) Configuration in space. (b) Configuration in time.

can then utilize the response of network to update their values at next time-step.

There are some pros and cons that have to be mentioned regarding EZM's working principle.

(1) The most significant feature of EZM is the decoupling of circuit topology and components' characteristics. The variations of components' characteristics will not affect the processing of circuit topology and the same is true vice versa. In most cases, the circuit topology remains unchanged during simulation and there is no need to invert matrix repeatedly.

(2) Even in cases when the circuit topology changes with time (like circuit breakers and switches), the development of matrix $\mathbf{T}$ is relatively easy and suitable for computer programing. The only computational complexity comes from the inversion of matrix $\mathbf{A}_1'$. Two features of $\mathbf{A}_1'$ make this task easy. First, the elements of $\mathbf{A}_1'$ have only three possible values: 0 or ± 1 and there are at most 2 nonzero values in each row; second, when the corresponding node of deleted row in $\mathbf{A}$ has at least one voltage source connected to it, then there is at least one row in $\mathbf{A}_1'$ that has only one nonzero value.

(3) The processing of individual components is also decoupled from each other. As can be seen in Fig. 3.2, the network receives system variables at time t_{n-1} and feeds back to components at time t_n. The feedbacks are used by components at time t_n, which means the component is using the previous time-step system variables to compute the current time-step value. This kind of configuration will be

definitely detrimental to the numerical stability and accuracy of the model. But this phenomena can be alleviated by better numerical algorithms and smaller time-steps, which will be analyzed in the later section. However, it does not mean this design is unreasonable. Actually, the author believe that it is a more natural way to simulate the behavior of circuits. From the point view of component itself, it does not care what kind of topology or vicinity components it connects to. It just behaves as its own way and can be viewed as the consequence of constantly interacting between component's input/output voltage and current. The only difference is that this interaction process in reality happens simultaneously or at an infinite small time-step.

(4) The decoupling of circuit topology and every individual component makes EZM extremely suitable for parallel computation. If the computational cost of developing matrix $\mathbf{T}$ is neglected, the overall computational complexity of EZM becomes linear or $O(N)$, and if fully parallel computation is achieved, the computational complexity even reduces to $O(1)$ in respect of computation time, i.e., constant computational complexity, which makes real-time simulation and smaller time-step possible.

(5) High scalability is achieved in EZM as when adding or removing one branch from the network, it is not necessary to remodel the system from scratch. The matrix that represents the remaining part of network is still useful and can be scaled up/down.

(6) Hierarchical design is inherently embedded in EZM. As can be seen that every branch is represented by voltage or current source; there is no restriction about the inner structure of branch at all. In other words, the equivalent voltage or current source in upper level may contain multiple lower level voltage and current sources as long as the interface with upper level remains the same. The inner variation in lower level will not affect the computation of upper level and they can even be solved using traditional nodal analysis or state-space method. This feature provides great facility for system partitioning.

(7) Multi-rate computation is convenient in EZM. Due to the decoupling nature of each individual component, every component can have its own simulation time-step and will not affect each other. Each row of matrix $\mathbf{T}$ represents the computation in network solver corresponding to one component. They can work along with individual component's rate and do not necessarily have the same time-step. This feature is very useful in practice because different components in the circuit have different inertia and require different time-steps.

(8) The choice of each component being viewed as voltage or current source is a big issue. Although no standard way for determining this is available, there are still some empirical practices which can serve as guidelines. Table 3.1 lists some common circuit components and their conventions.

Table 3.1: Some conventions of circuit components

Voltage-source-like	**Current-source-like**
Resistors, Capacitors, Batteries, Generators Switches in turn-on transients and steady on-state	Resistors, Inductors, PV panels, Motors, Switches in turn-off transients and steady off-state

Based on the above classification, some treatments have to be taken to avoid circuit contentions. For example, when two capacitors connect in parallel, they should be merged into one to avoid two voltage sources connected in parallel. The same is true for series connected inductors. Special attention should be given to resistors as they can be viewed as either voltage source or current source. It depends on the circuit configuration. When the resistor connects in parallel with a voltage source, then it should be viewed as a current source; when it connects in series with a current source, then it should be viewed as a voltage source. In addition, EZM is not suitable for solving a pure resistor network. The reason is that one cannot write a formula about the gradient of resistor's voltage or current. In other words, the transient frequency of resistor can be infinitely high which is beyond the computation ability of EZM. As a result, the transients of resistor should be incorporated with other circuit components and all the directly parallel and series connected resistors should be merged. Fortunately, this task is not hard to achieve.

(9) Three-phase system is very important in modern power systems and it is treated slightly different in EZM. It is well known that a n ports network has only n-1 independent output voltages or currents. The three-phase voltage/current source should be treated as two independent voltage/current sources in EZM unless the neutral point also connects out, as shown in Fig. 3.3.

As a result, the commonly used abc/dq coordinate transformation in EZM is

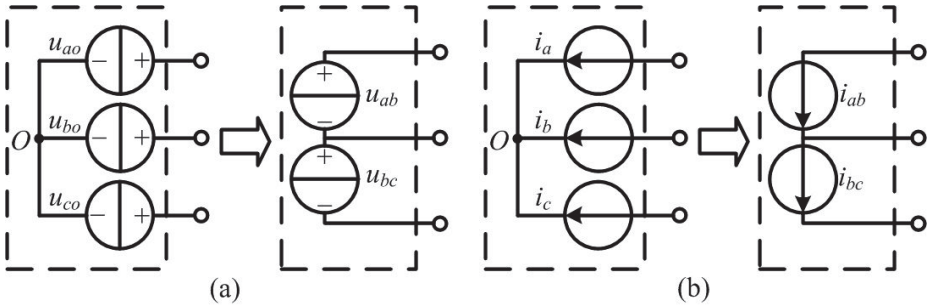

Figure 3.3: Three-phase voltage/current equivalent configuration in EZM. (a) Voltage source configuration. (b) Current source configuration.

slightly different with traditional one:

$$\begin{bmatrix} x_d \\ x_q \\ x_0 \end{bmatrix} = \frac{2}{3\sqrt{3}} \begin{bmatrix} \cos\left(\theta + \frac{\pi}{6}\right) & \cos\left(\theta - \frac{\pi}{2}\right) & \cos\left(\theta + \frac{5}{6}\pi\right) \\ -\sin\left(\theta + \frac{\pi}{6}\right) & -\sin\left(\theta - \frac{\pi}{2}\right) & -\sin\left(\theta + \frac{5}{6}\pi\right) \\ \frac{1}{2} & \frac{1}{2} & \frac{1}{2} \end{bmatrix} \begin{bmatrix} x_{ab} \\ x_{bc} \\ x_{ca} \end{bmatrix}, \tag{3.13}$$

where x_{ca}=-x_{ab}-x_{bc} is not an independent source.

3.3 Supplemental Analysis of EZM

In the modeling process of EZM, the branches of a circuit are first viewed as neither voltage or current sources and then it has been proved that for any circuit that has n nodes and b branches, the branch voltage/current relationship can be expressed in form of an anti-symmetric matrix $\mathbf{T}$. By utilization of this property, the circuit topology and component's characteristics can be decoupled and dealt with separately. As a result, the computational complexity is reduced and making EZM very suitable for parallel computing.

The antisymmetric matrix $\mathbf{T}$ is very important as it is the link between voltage and current relationships in the topology, where the current relationship can be found by manipulation of node-branch incidence matrix solely. In the forming process of $\mathbf{T}$, one key step is to develop the voltage relationship using the following equation:

$$\mathbf{T_1} = \mathbf{A}_2'(\mathbf{A}_1')^{-1}, \tag{3.14}$$

where $\mathbf{A}_1$ and $\mathbf{A}_2$ are two sections of node-branch incidence matrix $\mathbf{A}$ correspond to the n-1 voltage sources and b-n+1 current sources, respectively. The superscript $'$ denotes the transpose of a matrix.

From algorithm execution point of view, the matrix inversion should always be taken care of properly because it is usually very time consuming. This section provides a fast algorithm to compute $\mathbf{T}_1$ based on some features of $\mathbf{A}_1$, which has not been elaborated.

According to the definition of node-branch incidence matrix $\mathbf{A}$, there are only two non-zeros in every column, denoting the positive and negative ends' position in the topology. Moreover, one row of $\mathbf{A}$ is deleted to avoid row dependence because the sum of all rows is zero. As $\mathbf{A}_1$ is a subsection of $\mathbf{A}$, $\mathbf{A}_1$ has at most two non-zeros in each column as well and there is at least one column that has only one non-zero element.

In the proposed algorithm, the first step of computing $\mathbf{T}_1$ is performing column operations in $\mathbf{A}_1$ to eliminate one nonzero in those that have two. Take the $\mathbf{A}_1$ in the last section as an example,

$$\mathbf{A}_1 = \begin{bmatrix} 0 & 0 & 0 & 1 & 0 \\ 1 & 0 & 1 & 0 & 0 \\ -1 & 1 & 0 & 0 & 0 \\ 0 & -1 & 0 & 0 & 0 \\ 0 & 0 & 0 & 0 & -1 \end{bmatrix}. \tag{3.15}$$

By subtracting column 3 from column 1 and then adding column 1 into column 2, all the columns of $\mathbf{A}_1$ have one and only one nonzero element (and it is also true for all the rows). The column operations can be represented by a series of post-multiplication of elementary matrices $\mathbf{Q}_1 \cdots \mathbf{Q}_m$, where m is the number of operations required. For $\mathbf{A}_1$ in (3.15),

$$\bar{\mathbf{A}}_1 = \mathbf{A}_1\mathbf{Q}_1 \cdots \mathbf{Q}_m = \begin{bmatrix} 0 & 0 & 0 & 1 & 0 \\ 0 & 0 & 1 & 0 & 0 \\ -1 & 0 & 0 & 0 & 0 \\ 0 & -1 & 0 & 0 & 0 \\ 0 & 0 & 0 & 0 & -1 \end{bmatrix}, \tag{3.16}$$

where *m*=2 and

$$\mathbf{Q}_1 = \begin{bmatrix} 1 & 0 & 0 & 0 & 0 \\ 0 & 1 & 0 & 0 & 0 \\ -1 & 0 & 1 & 0 & 0 \\ 0 & 0 & 0 & 1 & 0 \\ 0 & 0 & 0 & 0 & 1 \end{bmatrix}, \mathbf{Q}_2 = \begin{bmatrix} 1 & 1 & 0 & 0 & 0 \\ 0 & 1 & 0 & 0 & 0 \\ 0 & 0 & 1 & 0 & 0 \\ 0 & 0 & 0 & 1 & 0 \\ 0 & 0 & 0 & 0 & 1 \end{bmatrix}. \tag{3.17}$$

Then the inverse of $\mathbf{A}_1$ can be written as

$$\mathbf{A}_1^{-1} = \mathbf{Q}_1 \cdots \mathbf{Q}_m \bar{\mathbf{A}}_1^{-1}. \tag{3.18}$$

Note that $\bar{\mathbf{A}}_1$ has one and only one nonzero (+1 or -1) in every column and row, which makes $\bar{\mathbf{A}}_1$ an orthogonal matrix whose inverse is its transpose. The proving process is quite straightforward.

Proof: Rewrite $\bar{\mathbf{A}}_1$ into column vector form:

$$\bar{\mathbf{A}}_1 = \begin{bmatrix} \mathbf{u}_1 & \mathbf{u}_2 & \dots & \mathbf{u}_{n-1} \end{bmatrix}, \tag{3.19}$$

where $\mathbf{u}_i$ are column vectors whose nonzero elements (+1 or -1) locate at (*n*-1) different rows. Then

$$\bar{\mathbf{A}}_1' \bar{\mathbf{A}}_1 = \begin{bmatrix} \mathbf{u}_1' \\ \mathbf{u}_2' \\ \dots \\ \mathbf{u}_{n-1}' \end{bmatrix} \begin{bmatrix} \mathbf{u}_1 & \mathbf{u}_2 & \dots & \mathbf{u}_{n-1} \end{bmatrix} = \mathbf{I}, \tag{3.20}$$

because

$$\mathbf{u}_i' \mathbf{u}_j = \begin{cases} 1, & when \quad i = j \\ 0, & when \quad i \neq j \end{cases}.$$

Accordingly,

$$(\mathbf{A}_1')^{-1} = (\mathbf{Q}_1 \cdots \mathbf{Q}_m \bar{\mathbf{A}}_1^{-1})' = \bar{\mathbf{A}}_1 \mathbf{Q}_m' \cdots \mathbf{Q}_1'. \tag{3.21}$$

Note that computing $(\mathbf{A}_1')^{-1}$ is not the ultimate goal and is not necessary. The more efficient way is combining (3.14) and (3.21) to compute $\mathbf{T}_1$ directly,

$$\mathbf{T}_1 = \mathbf{A}_2' \bar{\mathbf{A}}_1 \mathbf{Q}_m' \cdots \mathbf{Q}_1'. \tag{3.22}$$

As can be seen that the computation of $\mathbf{T}_1$ is split into $\mathbf{A}_2'$ post multiplication of $\bar{\mathbf{A}}_1$ and $\mathbf{Q}_m' \cdots \mathbf{Q}_1'$. Post multiplication of $\bar{\mathbf{A}}_1$ is simply reordering and sign changing of the original matrix. Post multiplication of $\mathbf{Q}_m' \cdots \mathbf{Q}_1'$ represents a series of elementary column operations that reverse to the operations from $\mathbf{A}_1$ to $\bar{\mathbf{A}}_1$. In both cases, the computation is easy to program and efficient on computer. There is no need to do matrix inversion.

Another important issue of EZM is the selection of a branch to be viewed as voltage or current source as some elements (like resistors) can be viewed as either voltage or current sources. In matrix analysis form, it's about the appropriate split of node-branch incidence matrix $\mathbf{A}$ into $\mathbf{A}_1$ and $\mathbf{A}_2$.

It can be seen in (3.14) that, as long as $\mathbf{A}_1$ is invertible, the subsequent analysis is valid. According to graph theory, if $\mathbf{M}(T)$ is the node-branch incidence matrix of a tree T that has n nodes, then any sub-matrix of $\mathbf{M}(T)$ of order $n-1$ is nonsingular [61]. That means, as long as the branches corresponding to $\mathbf{A}_1$ in $\mathbf{A}$ form a spanning tree, $\mathbf{A}_1$ is nonsingular. It makes sense because the branches in $\mathbf{A}_1$ should not form loops while spanning tree is a minimum subset of a graph that contains all nodes but without loops. Therefore, when selecting the branches in circuit to be deemed as voltage sources, any combination that constitutes a spanning tree of the circuit topology is practicable. The appropriate split comes from proper consideration of both topology requirements and element's characteristics.

3.4 Numerical Stability Analysis of EZM

This section uses a simply RLC circuit (shown in Fig. 3.4(a)) to analyze the numerical stability of EZM and its relation with nodal analysis and state-space method.

First, using the state-space method routine to solve the system, the following state-space equations can be obtained:

$$\begin{bmatrix} \frac{\mathrm{d}u_C}{\mathrm{d}t} \\ \frac{\mathrm{d}i_L}{\mathrm{d}t} \end{bmatrix} = \begin{bmatrix} -\frac{1}{R_1 C} & \frac{1}{C} \\ -\frac{1}{L} & -\frac{R_2}{L} \end{bmatrix} \begin{bmatrix} u_C \\ i_L \end{bmatrix} + \begin{bmatrix} 0 \\ \frac{1}{L} \end{bmatrix} u_{sc}, \tag{3.23}$$

where the voltage of capacitor u_C and the current of inductor i_L are selected as state variables.

When discretized using the Forward Euler method, (3.23) can be rewritten as:

$$\begin{bmatrix} u_C(t_n) \\ i_L(t_n) \end{bmatrix} = \begin{bmatrix} 1 - \frac{\Delta t}{R_1 C} & \frac{\Delta t}{C} \\ -\frac{\Delta t}{L} & 1 - \frac{R_2 \Delta t}{L} \end{bmatrix} \begin{bmatrix} u_C(t_{n-1}) \\ i_L(t_{n-1}) \end{bmatrix} + \begin{bmatrix} 0 \\ \frac{\Delta t}{L} \end{bmatrix} u_{sc}, \tag{3.24}$$

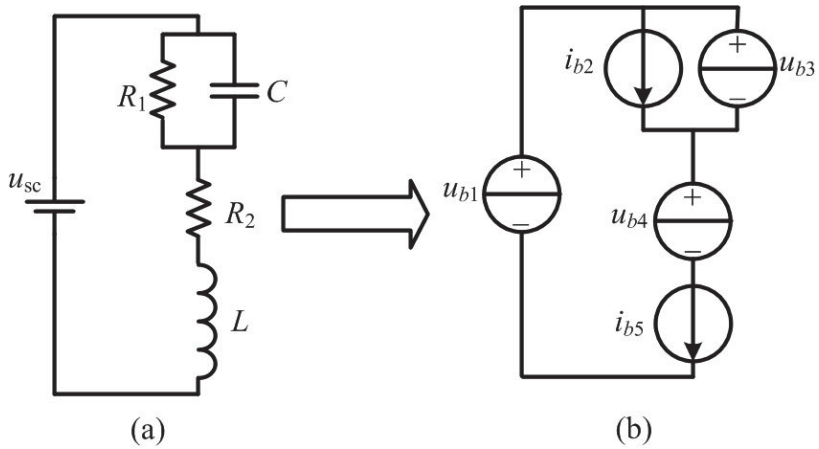

Figure 3.4: Numerical stability analysis example. (a) Circuit configuration. (b) Equivalent circuit in EZM.

where Δt=t_n-t_{n-1} is the time-step.

Second, solving the same system using EZM. The equivalent circuit is shown in Fig. 3.4(b). There are 5 branches in total and the corresponding matrix $\mathbf{T}$ can be obtained using Lemma 1.

$$\begin{bmatrix} i_{b1} \\ u_{b2} \\ i_{b3} \\ i_{b4} \\ u_{b5} \end{bmatrix} = \begin{bmatrix} 0 & 0 & 0 & 0 & -1 \\ 0 & 0 & 1 & 0 & 0 \\ 0 & -1 & 0 & 0 & 1 \\ 0 & 0 & 0 & 0 & 1 \\ 1 & 0 & -1 & -1 & 0 \end{bmatrix} \begin{bmatrix} u_{b1} \\ i_{b2} \\ u_{b3} \\ u_{b4} \\ i_{b5} \end{bmatrix}. \tag{3.25}$$

According to each component's characteristics, the system variables should be renewed in the following way:

$$\begin{aligned} u_{b1}(t_n) &= u_{sc}, \\ i_{b2}(t_n) &= \frac{u_{b2}(t_{n-1})}{R_1}, \\ u_{b3}(t_n) &= u_{b3}(t_{n-1}) + \frac{\Delta t}{C} i_{b3}(t_{n-1}), \\ u_{b4}(t_n) &= R_2 i_{b4}(t_{n-1}), \\ i_{b5}(t_n) &= i_{b5}(t_{n-1}) + \frac{\Delta t}{L} u_{b5}(t_{n-1}), \end{aligned} \tag{3.26}$$

where the capacitor voltage and inductor current are also discretized using the Forward Euler method. When incorporating with (3.25), $u_{b3}(t_n)$ and $i_{b5}(t_n)$ can

also be written as:

$$\begin{aligned} u_{b3}(t_n) &= (1 - \frac{\Delta t}{R_1 C}) u_{b3}(t_{n-1}) + \frac{\Delta t}{C} i_{b5}(t_{n-1}), \\ i_{b5}(t_n) &= (1 - \frac{R_2 \Delta t}{L}) i_{b5}(t_{n-1}) - \frac{\Delta t}{L} u_{b3}(t_{n-1}) + \frac{\Delta t}{L} u_{sc}. \end{aligned} \tag{3.27}$$

which is exactly the same with (3.24). In other words, the numerical stability of solving the system using (3.25) and (3.26) is exactly the same with (3.24). To find the eigenvalues of (3.24), the following equation should be solved:

$$[z - (1 - \frac{\Delta t}{R_1 C})][z - (1 - \frac{R_2 \Delta t}{L})] + \frac{\Delta t^2}{LC} = 0. \tag{3.28}$$

To make the eigenvalues locate inside the unit circle, the absolute term of (3.28) should be less than 1, i.e.,

$$(1 - \frac{\Delta t}{R_1 C})(1 - \frac{R_2 \Delta t}{L}) + \frac{\Delta t^2}{LC} < 1 \tag{3.29}$$

It can be observed that the first term in (3.29) is always less 1, provided that the second term is small enough, then the whole expression will be less than 1. In other words, as long as the time-step Δt is small enough, the above solver is stable.

Actually, lowering the time-step is not the only way to enhance the numerical stability of EZM. Another way is using better numerical algorithm. As mentioned before, the solver uses previous time-step system variables to compute the current time-step value. In numerical algorithm area, this means the employment of an explicit method. Explicit method means all the system variables are totally determined from previous time-step values and there is no influence between current time-step values. In this manner, the matrix inversion is saved. The implicit method, however, takes into account the interaction effect of system variables at each time-step and matrix inversion is required. This is why the implicit method is always unconditionally numerical stable while explicit method is always conditionally stable. For example, the Tustin method (or Trapezoidal method) always maps the left half plane zone in continuous domain to the inner unit circle zone in discrete domain and this is what nodal analysis method's computation approach. There are various explicit methods that can be found in literature and they are all suitable to be employed in EZM. Among them, the Heun method (also known as modified trapezoidal method or improved Euler method) and the Runge-Kutta method are good choices. The 4-th order Runge-Kutta method makes a good balance between numerical performance and computational load. It will serve as the numerical discretization method in the following test case.

3.5 Transformation between EZM and state-space model

It is known that state-space method is widely accepted in many engineering areas and can be used as the tool for multi-domain simulation. However, it is challenging to analytically derive state-space models for the system with moderate to large size, thus making it inconvenient for real-time simulation. Typically speaking, some graph theory concepts like tree and co-tree have to be utilized for analysis [62]- [65]. This section aims at building a bridge that links state-space method and EZM, through which the state-space model of a typical circuit can be obtained by transformation from EZM model.

In the following analysis, general *RLC* circuit is considered by convention. The steps converting from EZM model to state-space model are elaborated and an example is given for better illustration, as shown in Fig. 3.5(a).

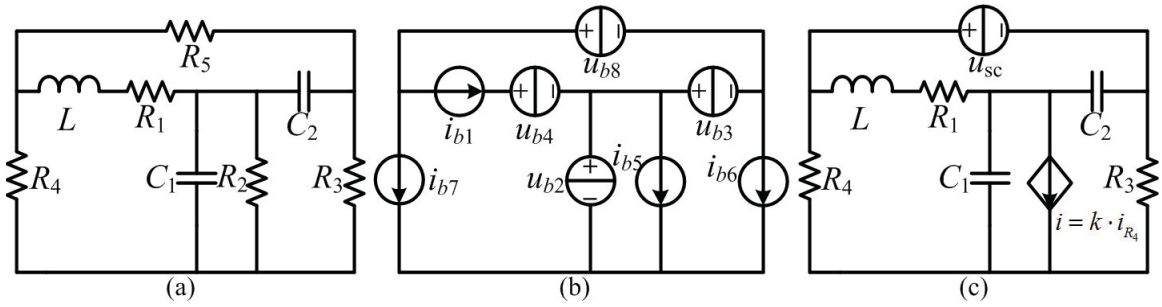

Figure 3.5: Example *RLC* Network and its equivalent model in EZM.

Step 1: Follow the routine presented in previous section to construct the EZM model and find the voltage-current relationship matrix $\mathbf{T}$. In the example given here, branch C_1, C_2, R_1 and R_5 are deemed as voltage sources while branch L, R_2, R_3 and R_4 are deemed as current sources, as shown in Fig. 3.5(b). The correspond-

ing $\mathbf{T}$ matrix is as follows,

$$\begin{bmatrix} u_{b1} \\ i_{b2} \\ i_{b3} \\ i_{b4} \\ u_{b5} \\ u_{b6} \\ u_{b7} \\ i_{b8} \end{bmatrix} = \begin{bmatrix} 0 & 0 & -1 & -1 & 0 & 0 & 0 & 1 \\ 0 & 0 & 0 & 0 & -1 & -1 & -1 & 0 \\ 1 & 0 & 0 & 0 & 0 & 1 & 1 & 0 \\ 1 & 0 & 0 & 0 & 0 & 0 & 0 & 0 \\ 0 & 1 & 0 & 0 & 0 & 0 & 0 & 0 \\ 0 & 1 & -1 & 0 & 0 & 0 & 0 & 0 \\ 0 & 1 & -1 & 0 & 0 & 0 & 0 & 1 \\ -1 & 0 & 0 & 0 & 0 & 0 & -1 & 0 \end{bmatrix} \begin{bmatrix} i_{b1} \\ u_{b2} \\ u_{b3} \\ u_{b4} \\ i_{b5} \\ i_{b6} \\ i_{b7} \\ u_{b8} \end{bmatrix} . \tag{3.30}$$

Step 2: Write the differential equation of all energy-storage elements (inductors and capacitors) based on $\mathbf{T}$ matrix.

$$\begin{cases} u_{b1} = L\dfrac{\mathrm{d}i_{b1}}{\mathrm{d}t} = -u_{b3} - u_{b4} + u_{b8} \\ i_{b2} = C_1\dfrac{\mathrm{d}u_{b2}}{\mathrm{d}t} = -i_{b5} - i_{b6} - i_{b7} \\ i_{b3} = C_2\dfrac{\mathrm{d}u_{b3}}{\mathrm{d}t} = i_{b1} + i_{b6} + i_{b7} \end{cases} . \tag{3.31}$$

Step 3: Note that it is often the case that the current of inductors and voltage of capacitors are selected as the state variables. In the above example, they are i_{b1}, u_{b2} and u_{b3}. However, the differential equations in Step 2 contain not only state variables, but also some other branch voltages and currents (called non-state variables henceforth). It is worth mentioning that the state and non-state variables constitute the complete set of branch variables used in EZM. The next operation needed is to express non-state variables in the form of state variables by taking elements' characteristics into account.

Some non-state variables have no inter-cross element with other non-state variables in matrix $\mathbf{T}$. They can be expressed as state variable forms easily. In the given example, u_{b4}, i_{b5} and i_{b6} are such type.

$$\begin{cases} i_{b4} = \dfrac{u_{b4}}{R_1} = i_{b1} \\ u_{b5} = R_2 i_{b5} = u_{b2} \\ u_{b6} = R_3 i_{b6} = u_{b2} - u_{b3} \end{cases} \Rightarrow \begin{cases} u_{b4} = R_1 i_{b1} \\ i_{b5} = u_{b2}/R_2 \\ i_{b6} = (u_{b2} - u_{b3})/R_3 \end{cases} . \tag{3.32}$$

Other non-state variables, however, have inter-cross element with each other and matrix equation has to be solved. For i_{b7} and u_{b8} in the example, the following

matrix equation can be formed,

$$\begin{cases} u_{b7} = R_4 i_{b7} = u_{b2} - u_{b3} + u_{b8} \\ i_{b8} = u_{b8}/R_5 = -i_{b1} - i_{b7} \end{cases} \Rightarrow$$

$$\begin{bmatrix} R_4 & -1 \\ 1 & 1/R_5 \end{bmatrix} \begin{bmatrix} i_{b7} \\ u_{b8} \end{bmatrix} = \begin{bmatrix} u_{b2} - u_{b3} \\ -i_{b1} \end{bmatrix}. \tag{3.33}$$

Solving (3.33), the remaining non-state variables are expressed in the form of state variables,

$$\begin{cases} i_{b7} = -\dfrac{R_5}{R_4 + R_5} i_{b1} + \dfrac{1}{R_4 + R_5}(u_{b2} - u_{b3}) \\ u_{b8} = -\dfrac{R_4 R_5}{R_4 + R_5} i_{b1} - \dfrac{R_5}{R_4 + R_5}(u_{b2} - u_{b3}) \end{cases}. \tag{3.34}$$

It can be observed that the matrix in this process has fixed off-diagonal elements (0 or ± 1) and only the diagonals vary with branch characteristics. Therefore, some special techniques can be utilized to expedite the solving process, such as the algorithms presented in the last chapter.

Step 4: Combine the results in Steps 2 and 3, the differential equations can be rewritten in the form that only has state variables. The results in (3.31), (3.32) and (3.34) yield

$$\begin{cases} \dfrac{\mathrm{d}i_{b1}}{\mathrm{d}t} = -(R_1 + \dfrac{R_4 R_5}{R_4 + R_5})\dfrac{1}{L} i_{b1} - \dfrac{R_5}{(R_4 + R_5)L} u_{b2} \\ \qquad\qquad - \dfrac{R_4}{(R_4 + R_5)L} u_{b3} \\ \dfrac{\mathrm{d}u_{b2}}{\mathrm{d}t} = \dfrac{R_5}{(R_4 + R_5)C_1} i_{b1} - (\dfrac{1}{R_2} + \dfrac{1}{R_3} + \dfrac{1}{R_4 + R_5})\dfrac{1}{C_1} u_{b2} \\ \qquad\qquad + (\dfrac{1}{R_3} + \dfrac{1}{R_4 + R_5})\dfrac{1}{C_1} u_{b3} \\ \dfrac{\mathrm{d}u_{b3}}{\mathrm{d}t} = \dfrac{R_4}{(R_4 + R_5)C_2} i_{b1} + (\dfrac{1}{R_3} + \dfrac{1}{R_4 + R_5})\dfrac{1}{C_2} u_{b2} \\ \qquad\qquad - (\dfrac{1}{R_3} + \dfrac{1}{R_4 + R_5})\dfrac{1}{C_2} u_{b3} \end{cases}, \tag{3.35}$$

which is exactly the canonical form of state variable model.

Note that it is also very convenient to handle external and dependent sources in above steps. The external sources can be viewed the same as state variables because they are permitted to appear in the right hand side of the differential equations. The only difference is that the external sources should be placed into input matrix $\mathbf{B}$ rather than system matrix $\mathbf{A}$. The dependent sources can be handled by

putting them aside first and solving the other non-state variables. When all the other non-state variables are solved, substituting them into dependent sources' own function, then the dependent sources can be expressed as function of state variables and/or external sources as well.

In the above example, if $u_{b8} = u_{\rm sc}$ is an external stimulus voltage source and $i_{b5} = k \cdot i_{b7}$ is a current controlled current source (shown in Fig.3.5.(c)), then Steps 1 and 2 of the transformation remain unchanged and the solution of non-state variables in Step 3 becomes

$$\begin{cases} u_{b4} = R_1 i_{b1} \\ i_{b6} = (u_{b2} - u_{b3})/R_3 \\ i_{b7} = (u_{b2} - u_{b3} + u_{b8})/R_4 \end{cases}. \tag{3.36}$$

Accordingly, the dependent source can be expressed as

$$i_{b5} = \frac{k}{R_4}(u_{b2} - u_{b3} + u_{b8}). \tag{3.37}$$

The corresponding state variable model of the modified schematic graph is obtained by combining (3.31), (3.36) and (3.37), which yield

$$\frac{d\mathbf{x}}{dt} = \mathbf{A}\mathbf{x} + \mathbf{B}u_{\rm sc}, \tag{3.38}$$

where

$$\mathbf{A} = \begin{bmatrix} -\frac{R_1}{L} & 0 & \frac{1}{L} \\ 0 & -(\frac{k+1}{R_4} + \frac{1}{R_3})\frac{1}{C_1} & (\frac{k+1}{R_4} + \frac{1}{R_3})\frac{1}{C_1} \\ \frac{1}{C_2} & (\frac{1}{R_3} + \frac{1}{R_4})\frac{1}{C_2} & -(\frac{1}{R_3} + \frac{1}{R_4})\frac{1}{C_2} \end{bmatrix},$$

$$\mathbf{B} = \begin{bmatrix} \frac{1}{L} \\ -\frac{k+1}{R_4 C_1} \\ \frac{1}{R_4 C_2} \end{bmatrix}, \mathbf{x} = \begin{bmatrix} i_{b1} \\ u_{b2} \\ u_{b3} \end{bmatrix}.$$

The quickest way to check the validity of the transformation is to examine the degrees of freedom (DOF) in both models. The circuit in Fig. 3.5(a) has 8 branches, which means they can determine 8 independent values. This number is exactly the same with the DOF in (3.35) and also equals to the rank of matrix $\mathbf{T}$. Similarly, the system in Fig. 3.5(c) has 7 branches because one branch (u_{b8}) is deemed as external stimulus sources. Correspondingly, the model in (3.38) also has 7 independent matrix element values.

The above steps demonstrate that it is feasible to transform EZM model to state-space model. In other words, EZM model is another correct representation of mathematic description of the circuit. The state-space model and EZM model are actually one thing that takes two different forms. They are equivalent in mathematic modeling.

The effort of constructing state variable model through EZM model may not necessarily be much easier than constructing it directly using graphic theory. However, if it is for circuit simulation purpose only, there is actually no need to construct state-space model at all. The EZM model is able to offer the correct results as well. And more importantly, the effort of constructing EZM model is much easier than state-space model. The EZM takes branch variables as the computation objects and decouples them during the modeling process. It is a more natural way to comprehend the circuit and also very suitable for modeling and parallel computing on digital processors. These features make EZM model a competitive alternative to replace state-space model in multi-domain simulation because of its high computational efficiency and relatively less modeling effort.

The above process, on the other hand, can be conducted backward as well, i.e., transform state variable model into EZM model. All that needs to be done is to construct an appropriate matrix $\mathbf{T}$ and select several rows to represent the state variables (the remaining parts then become non-state variables). The only thing that one should be aware of is that the number of branches in the circuit should be greater than or equal to the DOF in the state variable model. However, it has to be pointed out that the reversing transformation is not unique, i.e., there are multiple equivalent circuits corresponding to the same state variable model. Moreover, there is practically no need to do so because the state variable model is a more concise representation of the system. If the state variable model is already given, it can be used for computation directly. In cases like multi-domain simulation, the state variable model from one domain is often mixed with circuit model from the other domain and if a unified solver is required, there exists a simple equivalent configuration that can be recognized both by state variable method and EZM, as shown in Fig. 3.6. The main advantage is that the circuit has been simplified to a great extent by utilization of dependent sources and the coefficients have direct corresponding relation.

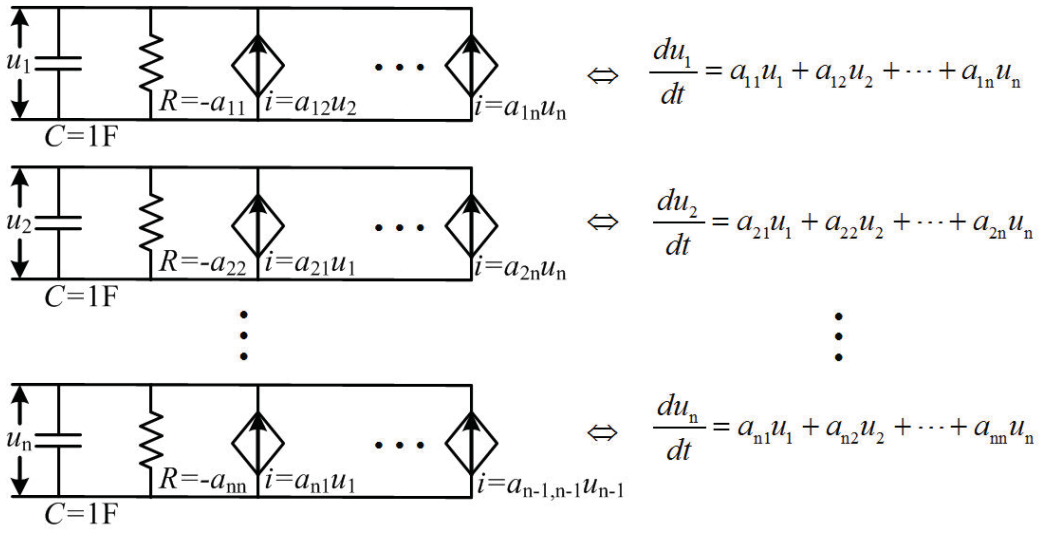

Figure 3.6: Simple equivalent circuit configuration of state variable model.

3.6 Summary

This chapter presented an efficient method (EZM) which is very suitable for large-scale circuit simulation. The proposed method was based on a circuit lemma, which indicated the relationship of branch voltages and currents. The modeling methodology and mathematic analysis of of EZM is provided. By utilization of this lemma, the circuit topology and components' characteristics are decoupled and the computational complexity reduces to nearly linear. The transformation between EZM model and state-space model is also elaborated and with the help of EZM, matrix inversion can be avoided when solving a large complex system.

4

A Fast Time-step Selection Approach for EZM

4.1 Introduction

As has been mentioned in the last chapter, simulating a circuit using EZM means the employment of explicit method for solving the differential equations of the system. It is because of the explicit numerical method that makes EZM very suitable for parallel computation because every state variable can be updated independently during the computation process. However, the numerical stability of explicit methods is always conditional as they usually have relatively small stability region. That makes time-step selection very important for successful implementation of EZM. This chapter takes the high frequency low loss (HFLL) circuit, in specific the electromagnetic interference (EMI) filter, as an example to illustrate a fast time-step selection approach for EZM.

Time-domain simulation of EMI circuit model in power electronics has received more and more attention in recent years [66]- [68]. Compared with frequency-domain simulation, the time-domain simulation approach is straightforward but requires substantial computation resource and lengthy simulation time [69]. Therefore, if possible, the circuit simulation users always want to use larger time-step for efficient analysis and design, which makes time-step selection one of the most critical procedures in time-domain simulation. Typically, a lower time-step yields

higher output accuracy but consumes more computation time. However, the time-step can not be set arbitrarily large. There are two constraints that determine the upper bound of the time-step. One is that the simulation results should meet some accuracy requirement. For example, if the 40th harmonic of a current/voltage is to be analyzed, then the time-step should be at most half the reciprocal of 40 times the base (modulation) frequency. The other constraint is the numerical stability of the discrete solver. This is especially important for explicit solvers because they are always conditionally stable.

Numerical stability is a desirable property of numerical methods. A numerical method is said to be stable if errors incurred in one step do not magnify in later steps [70]. The numerical stability of a given problem is determined by two factors: the numerical solver and the simulation model. There are two types of numerical solvers that are available for circuit simulation: implicit and explicit solver. The implicit solvers usually have large stability region in the complex plane. Some even include the whole left half plane, which means they are always numerically stable as long as the simulation model itself is stable in continuous domain. Examples of implicit solver include the Backward Euler (BE) and the Trapezoidal rule (TR). However, BE and TR method reveal to be both poorly accurate and inefficient when employed to simulate circuits with high frequency oscillation due to their low-order truncation error [71]. Inefficiency comes from the fact that matrix inversion or its equivalent alternative (like Gaussian Elimination or some iterative algorithms) is inevitable when utilizing the implicit solver. The computational complexity of such process increases as a cubic function $O(N^3)$ of the system size. Moreover, the implicit solver is not suitable for parallel computation, which is the trend of future high performance computing.

The explicit solvers, on the other hand, usually have smaller stability region in the complex plane. But they can get rid of matrix inversion and are very suitable for parallel computation. The corresponding computational complexity increases only as quadratic function $O(N^2)$ of the system size and can be apportioned on distributed computational resources. It should be noted that the numerical solver does not possess region of stability independent of the problem it is applied to [72], so the product ($z = h\lambda$) is chosen for stability evaluation, where h is the time-step and λ is the eigenvalue of the model. The difficulty of applying explicit solver is how to find the proper time-step h so that every z of the simulation model lies within the stability region of the solver.

It should also be mentioned that although explicit solvers generally have smaller

stability region, it does not mean they are less accurate than implicit solvers. The accuracy of a solver is usually quantified by local truncation error (LTE) and it only relates to the numerical order of that solver. In general, a method with $O(h^{n+1})$ LTE is said to be of nth order. For example, the Heun's method (explicit) and Tustin method (implicit) offer the same accuracy results at the same time-step as long as they are numerical stable because they are both order-2 methods and their LTEs are in $O(h^3)$.

Although the stability region of a given solver in the complex z plane can be found beforehand, the eigenvalues of the circuit model may distribute randomly. To determine the suitable time-step, all the eigenvalues have to be found because usually the stability region has different lengths (from the edge to the origin) along different directions. However, the computational complex of eigenvalue problem is also $O(N^3)$. That creates a dilemma: if a $O(N^3)$ problem has to be solved before using explicit solver, why not just use implicit solver directly? Not to mention the effort that has to made to construct the state-space model of the circuit.

The time-step selection process of simulating a general circuit using explicit solver is in no way easy. In many cases this is done by estimation, then trial and error iteration, which is very time-consuming. Some variable time-step methods, like the Runge-Kutta-Fehlberg (RKF45) method [73], use two different approximations for the solution (fourth and fifth order Runge-Kutta) and adjust next time-step size accordingly based on the comparison results [74]. However, the RKF45 method may fail and give fundamentally incorrect solutions because the generated step size is outside the region of stability, especially for the class of stiff ordinary differential equations (ODEs) [75]. Failure of such time-step control scheme can be explained by the lack of information from the circuit itself.

Nevertheless, for some special class of circuits, the time-step selection process can be expedited by leveraging the circuit properties. The high frequency low loss (HFLL) circuit is one of such type. High frequency means there are oscillatory phenomenon in the circuit. Typically, the parasitic capacitance and inductance influence are incorporated so that small time-step has to be utilized. Low loss in this paper means the energy dissipated in the circuit is negligible so that the eigenvalues of the circuit are very close to the imaginary axis. In such cases, only the maximum or upper bound of the eigenvalues needs to be found to determine the suitable time-step.

This chapter presents a quick method to select time-step for explicit solver based simulation of HFLL circuit. The proposed method is easy to implement

and remains $O(N^2)$ in computation. Such property preserves the efficiency superiority of explicit solver over implicit solver. This method is verified by an EMI filter simulation in a DC/AC converter compared with experimental results and shows its strength in efficiency.

4.2 Stability Region of Explicit Solver

Stability region is an important property of a numerical solver. It is evaluated by applying the solver to the Dahlquist test equation:

$$\dot{x} = \lambda x, x(0) = x_0, \tag{4.1}$$

where $\dot{x}$ means derivative of x, λ is eigenvalue of the problem and x_0 is the initial value. The stability region is quantified in the complex z plane ($z = \lambda h$), where h is the time-step.

The region that makes $x(k)$ converging to its analytic solution as $k \to \infty$ is called stability region, where $x(k)$ represents the kth step solution. Fig. 4.1 illustrates the stability regions of 1 to 4th order Runge-Kutta (RK) methods.

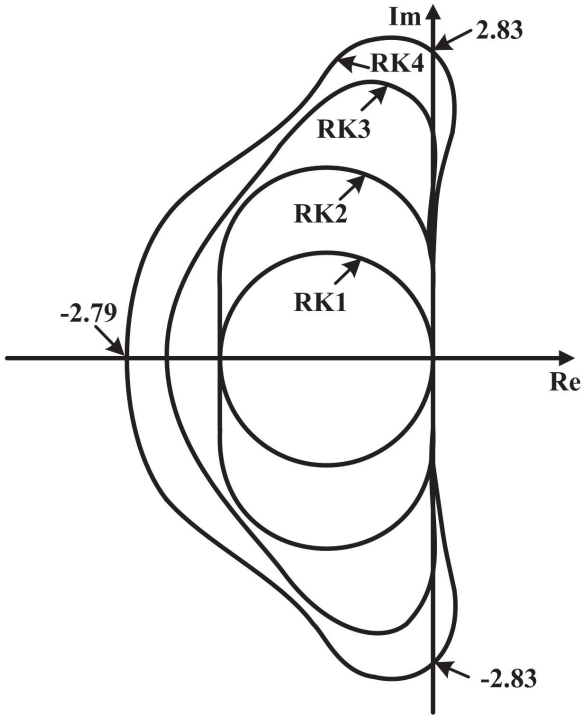

Figure 4.1: Stability regions of 1 to 4th order Runge-Kutta methods.

In real applications, it is more common to solve the multi-variable state-space

equation:

$$\dot{\mathbf{x}} = \mathbf{A}\mathbf{x}, \mathbf{x}(0) = \mathbf{x}_0, \tag{4.2}$$

where $\mathbf{x}$ is state vector and $\mathbf{A}$ is system matrix. It may be obscure how the numerical stability results derived from (4.1) can be applied to analyze (4.2). A simple matrix transformation can make it clear.

If $\mathbf{A}$ is diagonalizable (which is often the case in engineering problems), then there exists a matrix $\mathbf{P}$ that satisfies

$$\mathbf{A} = \mathbf{P}\mathbf{\Lambda}\mathbf{P}^{-1}, \tag{4.3}$$

where $\mathbf{\Lambda}$ is a diagonal matrix. It also can be proved that the diagonals of $\mathbf{\Lambda}$ are the eigenvalues of $\mathbf{A}$ and the columns of $\mathbf{P}$ are the corresponding eigenvectors. If $\mathbf{y} = \mathbf{P}^{-1}\mathbf{x}$ is selected as the new state vector, then (4.2) can be transformed into

$$\dot{\mathbf{y}} = \mathbf{P}^{-1}\mathbf{A}\mathbf{P}\mathbf{y} = \mathbf{\Lambda}\mathbf{y}. \tag{4.4}$$

Solving (4.4) is like solving n individual Dahlquist equations, where n is the dimension of $\mathbf{y}$. Once $\mathbf{y}$ is obtained, $\mathbf{x}$ can be obtained by simple linear transformation.

The above analysis implies that as long as all the eigenvalues of $\mathbf{A}$ times time-step h locate in the stability region of a given solver, then it is numerically safe to use that solver in simulation. Generally speaking, it is difficult to find the complete set of eigenvalues of matrix $\mathbf{A}$. However, for HFLL circuit, its eigenvalues are very close to the imaginary axis, which makes only the maximum eigenvalue matters in quantifying the time-step.

This chapter chooses the classical fourth-order Runge-Kutta (RK4) method as the solver because it offers a good balance between accuracy and computation effort. It is the highest order method in RK family that uses the same number of function evaluations as with the order of accuracy each step. Higher order RK methods need much more computation efforts but do not necessarily bring better accuracy results [82].

The stability region of RK4 method can be found in Fig. 4.1. Its intersections with imaginary axis are $\pm j2.83$. Therefore, the time-step that is used for solving HFLL circuit should satisfy

$$h \leq \frac{2.83}{\bar{\lambda}}, \tag{4.5}$$

where $\bar{\lambda}$ is the upper bound of eigenvalues of HFLL circuit.

4.3 Finding The Upper Bound of Eigenvalues of HFLL Circuit

There are various ways to find the upper bound of eigenvalues of a given matrix. The most straightforward way must be finding all the eigenvalues first, then the maximum eigenvalue can be identified. This is definitely not an efficient choice because most information are wasted and only the maximum value is of concern. There are also some iterative algorithms available that can be used to find the maximum eigenvalue, like the power iteration, the Lanczos algorithm and the Arnoldi algorithm. However, these algorithms are either prone to convergence problem or subject to some restrictions. Most importantly, they are not computationally efficient as they require $O(N^2)$ calculations in each iteration. In the worst case, N iterations are needed to finish the process. Therefore, they are still $O(N^3)$ algorithms in complexity.

Unlike all above methods, this paper utilize Laguerre–Samuelson's inequality to find the upper bound of eigenvalues of HFLL circuit. This inequality can be expressed as following [83]:

Let $\sum_{k=0}^{n} c_k s^k$ be a polynomial with all real roots. Then all roots of this polynomial are bounded by

$$-\frac{c_{n-1}}{nc_n} \pm \frac{n-1}{nc_n}\sqrt{c_{n-1}^2 - \frac{2n}{n-1}c_n c_{n-2}}. \tag{4.6}$$

It is known that the eigenvalues of a matrix are the roots of its characteristic polynomial. When applying this inequality to the characteristic polynomial of a matrix, the above bounds can be even simplified because $c_n = 1$. Then only two scalar values c_{n-1} and c_{n-2} need to be computed to find the upper bound. The following two subsections explain how to compute these two scalar values for non-degenerate and degenerate HFLL circuits's state-space matrix, respectively. Degenerate circuits are those that contain one or more loops that consist only of capacitances and possibly voltage sources, or one or more cutsets that consist only of inductances and possibly current sources [84]. Non-degenerate circuits are those do not contain such loops and cutsets. The handling of these two cases are slightly different.

4.3.1 Non-degenerate circuit case

As indicated previously, the energy dissipation in HFLL circuit is negligible, which means the values of resistors in the circuit are either very large or very small so

that the current or voltage of the resistor can be neglected. In the first step, these resistors are removed from the circuit to expedite the analysis. The large value resistor branch is viewed as open circuit while the small value resistor branch is viewed as short circuit. After removing these resistors, the remaining part contains only capacitors and inductors. To proceed with the analysis, it is necessary to show that a circuit consisting of only capacitors and inductors has all its eigenvalues on the imaginary axis.

It has been proved in the last chapter that for a given circuit that has b branches and n nodes, there exists $n-1$ branches to be viewed as voltage sources and the remaining $b-n+1$ branches to be viewed as current sources. Then the voltage/current relationship of these branches can be expressed in form of an anti-symmetric matrix.

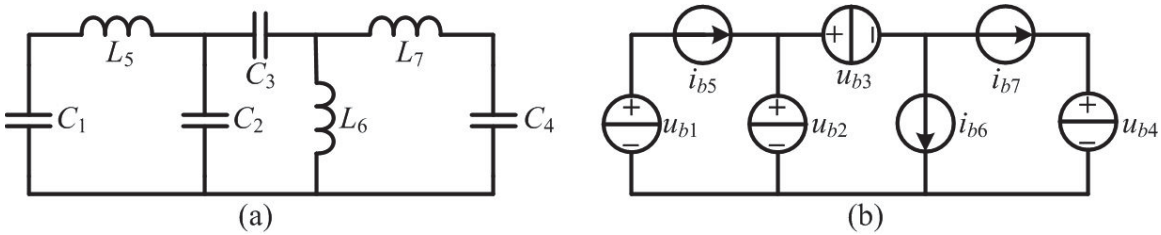

Figure 4.2: A non-degenerate circuit consisting of only capacitors and inductors.

For a non-degenerate circuit consisting of only capacitors and inductors, the capacitors are suitable to be viewed as voltage sources while the inductors are suitable to be reviewed as current sources. Take the circuit in Fig. 4.2 as an example. If the branches of C_1, C_2, C_3, C_4 are viewed as voltage sources and the branches of L_5, L_6, L_7 are viewed as current sources, then their voltage/current relationship can be express as

$$\begin{bmatrix} i_{b1} \\ i_{b2} \\ i_{b3} \\ i_{b4} \\ u_{b5} \\ u_{b6} \\ u_{b7} \end{bmatrix} = \underbrace{\begin{bmatrix} 0 & 0 & 0 & 0 & -1 & 0 & 0 \\ 0 & 0 & 0 & 0 & 1 & -1 & -1 \\ 0 & 0 & 0 & 0 & 0 & 1 & 1 \\ 0 & 0 & 0 & 0 & 0 & 0 & 1 \\ 1 & -1 & 0 & 0 & 0 & 0 & 0 \\ 0 & 1 & -1 & 0 & 0 & 0 & 0 \\ 0 & 1 & -1 & -1 & 0 & 0 & 0 \end{bmatrix}}_{\mathbf{R}} \begin{bmatrix} u_{b1} \\ u_{b2} \\ u_{b3} \\ u_{b4} \\ i_{b5} \\ i_{b6} \\ i_{b7} \end{bmatrix}. \tag{4.7}$$

As can be seen, the relation matrix $\mathbf{R}$ in (4.7) is an anti-symmetric matrix. More importantly, simply replacing the left-hand-side vector in (4.7) with the derivative of right-hand-side vector times the corresponding capacitor or inductor values, the state-space model of this circuit can be obtained, as shown in (4.8).

$$\begin{bmatrix} C_1\frac{du_{b1}}{dt} \\ C_2\frac{du_{b2}}{dt} \\ C_3\frac{du_{b3}}{dt} \\ C_4\frac{du_{b4}}{dt} \\ L_5\frac{di_{b5}}{dt} \\ L_6\frac{di_{b6}}{dt} \\ L_7\frac{di_{b7}}{dt} \end{bmatrix} = \begin{bmatrix} 0 & 0 & 0 & 0 & -1 & 0 & 0 \\ 0 & 0 & 0 & 0 & 1 & -1 & -1 \\ 0 & 0 & 0 & 0 & 0 & 1 & 1 \\ 0 & 0 & 0 & 0 & 0 & 0 & 1 \\ 1 & -1 & 0 & 0 & 0 & 0 & 0 \\ 0 & 1 & -1 & 0 & 0 & 0 & 0 \\ 0 & 1 & -1 & -1 & 0 & 0 & 0 \end{bmatrix} \begin{bmatrix} u_{b1} \\ u_{b2} \\ u_{b3} \\ u_{b4} \\ i_{b5} \\ i_{b6} \\ i_{b7} \end{bmatrix}. \tag{4.8}$$

It is known that the eigenvalues of an anti-symmetric matrix are either 0 or purely imaginary, i.e., they all locate on the imaginary axis. Although the state-space matrix ($\mathbf{A}$) of a non-degenerate pure capacitor and inductor circuit is not an anti-symmetric matrix, it can be expressed as the multiplication of a diagonal matrix ($\mathbf{D}$) and an anti-symmetric matrix ($\mathbf{R}$):

$$\mathbf{A} = \mathbf{DR}, \tag{4.9}$$

where the diagonals of $\mathbf{D}$ are the reciprocals of the capacitor and inductor values. For the model in (4.8),

$$\mathbf{D} = \begin{bmatrix} \frac{1}{C_1} & 0 & 0 & 0 & 0 & 0 & 0 \\ 0 & \frac{1}{C_2} & 0 & 0 & 0 & 0 & 0 \\ 0 & 0 & \frac{1}{C_3} & 0 & 0 & 0 & 0 \\ 0 & 0 & 0 & \frac{1}{C_4} & 0 & 0 & 0 \\ 0 & 0 & 0 & 0 & \frac{1}{L_5} & 0 & 0 \\ 0 & 0 & 0 & 0 & 0 & \frac{1}{L_6} & 0 \\ 0 & 0 & 0 & 0 & 0 & 0 & \frac{1}{L_7} \end{bmatrix}. \tag{4.10}$$

The characteristic polynomial of $\mathbf{A}$ can be expressed as

$$\begin{aligned} \det(\lambda\mathbf{I} - \mathbf{A}) &= \det(\lambda\mathbf{I} - \mathbf{DR}) \\ &= \det(\mathbf{D}^{\frac{1}{2}}(\lambda\mathbf{I} - \mathbf{D}^{\frac{1}{2}}\mathbf{R}\mathbf{D}^{\frac{1}{2}})\mathbf{D}^{-\frac{1}{2}}), \end{aligned} \tag{4.11}$$

where $\mathbf{I}$ is identity matrix, $\mathbf{D}^{\frac{1}{2}}$ and $\mathbf{D}^{-\frac{1}{2}}$ are square root of $\mathbf{D}$ and $\mathbf{D}^{-1}$, respectively. It can be concluded that the eigenvalues of $\mathbf{A}$ are the same with $\mathbf{D}^{\frac{1}{2}}\mathbf{R}\mathbf{D}^{\frac{1}{2}}$. Because $\mathbf{D}^{\frac{1}{2}}$ is a diagonal matrix, $\mathbf{D}^{\frac{1}{2}}\mathbf{R}\mathbf{D}^{\frac{1}{2}}$ is an anti-symmetric matrix as well. Therefore, the eigenvalues of $\mathbf{A}$ all locate on the imaginary axis.

Another issue that has to be aware of is that the Laguerre-Samuelson's inequality is valid only when the roots of the polynomial are all real. Thus it can not be applied to the characteristic polynomial of $\mathbf{A}$ directly. To fix this, recall that the imaginary part of eigenvalues of a real matrix always appear in conjugate pairs, thus it is more appropriate to calculate the square of eigenvalues of $\mathbf{A}$ to make the roots of the characteristics polynomial all real. Doing so is equal to calculating the eigenvalues of $\mathbf{A}^2$ (denoted as $\bar{\mathbf{A}}$ henceforth). Then the question is transformed into computing coefficients (c_{n-1} and c_{n-2}) of characteristic polynomial of $\bar{\mathbf{A}}$ accordingly.

Factoring $\bar{\mathbf{A}}$'s characteristic polynomial as following

$$\sum_{k=0}^{n} c_k s^k = \coprod_{i=1}^{n} (s - s_i) = s^n - \sum_{i=1}^{n} s_i s^{n-1} + \cdots, \tag{4.12}$$

where s_i are the roots of the polynomial. Because the sum of eigenvalues of a matrix is equal to the trace of it. It can be easily found that

$$c_{n-1} = -\sum_{i=1}^{n} s_i = -\text{trace}(\bar{\mathbf{A}}) = -\sum_{i=1}^{n} \bar{a}_{ii}, \tag{4.13}$$

where $\bar{a}_{ii}$ are the diagonals of $\bar{\mathbf{A}}$.

The computation of c_{n-2}, however, is not that explicit. One possible way is to find its relationship with the traces of powers of $\bar{\mathbf{A}}$ by leveraging Newton's identities [85]:

Denoting t_k as the trace of $\bar{\mathbf{A}}^k$, then the following formula holds:

$$\begin{aligned} &t_k + c_{n-1}t_{k-1} + \cdots + c_0 t_{k-n} = 0, (k > n); \\ &t_k + c_{n-1}t_{k-1} + \cdots + c_{n-k+1}t_1 = -k c_{n-k}, (1 \le k \le n). \end{aligned} \tag{4.14}$$

Setting k=1 and 2 in (4.14), respectively, the expression of c_{n-2} can be found as

$$c_{n-2} = \frac{1}{2}\left(t_1^2 - t_2\right). \tag{4.15}$$

Combining (4.6), (4.13) and (4.15), the upper bound (in absolute value) of eigenvalues of $\bar{\mathbf{A}}$ can be written as

$$\bar{s} = \frac{t_1}{n} - \sqrt{n-1}\sqrt{\frac{t_2}{n} - \left(\frac{t_1}{n}\right)^2}. \tag{4.16}$$

Note that $\bar{s} < 0$ because the eigenvalues of $\bar{\mathbf{A}}$ are all negative. The expression (4.16) is exactly the same with the bound presented in [86] and is claimed as the "tightest" when all the eigenvalues are real.

The corresponding upper bound of eigenvalues of $\mathbf{A}$ is

$$\bar{\lambda} = \sqrt{|\bar{s}|} = \sqrt{-\frac{t_1}{n} + \sqrt{n-1}\sqrt{\frac{t_2}{n} - \left(\frac{t_1}{n}\right)^2}}. \tag{4.17}$$

As can be seen that only two matrix multiplications (one from $\mathbf{A}$ to $\bar{\mathbf{A}}$ and one from $\bar{\mathbf{A}}$ to $\bar{\mathbf{A}}^2$) is required to obtain the upper bound of the eigenvalues of a HFLL circuit using this method. Besides, the second multiplication (from $\bar{\mathbf{A}}$ to $\bar{\mathbf{A}}^2$) is not necessarily to be accomplished completely because only the diagonals are of concern. These mathematic operations still remain $O(N^2)$ in computation complexity. Thus it preserves the computation efficiency advantage of explicit solver.

In addition, because of the anti-symmetry of $\mathbf{R}$, the calculation of $\mathbf{A}^2$ can be further simplified. The matrix $\mathbf{R}$ and $\mathbf{D}$ can be partitioned into the following form:

$$\mathbf{R} = \begin{bmatrix} \mathbf{0} & \mathbf{R_{12}} \\ \mathbf{-R'_{12}} & \mathbf{0} \end{bmatrix}, \mathbf{D} = \begin{bmatrix} \mathbf{D_{11}} & \mathbf{0} \\ \mathbf{0} & \mathbf{D_{22}}, \end{bmatrix} \tag{4.18}$$

where $\mathbf{R}'_{12}$ is the transpose of $\mathbf{R}_{12}$. Then $\bar{\mathbf{A}}$ and $\bar{\mathbf{A}}^2$ can be expressed as

$$\bar{\mathbf{A}} = \begin{bmatrix} -\mathbf{D}_{11}\mathbf{R}_{12}\mathbf{D}_{22}\mathbf{R}'_{12} & \mathbf{0} \\ \mathbf{0} & -\mathbf{D}_{22}\mathbf{R}'_{12}\mathbf{D}_{11}\mathbf{R}_{12} \end{bmatrix} \tag{4.19}$$

$$\bar{\mathbf{A}}^2 = \begin{bmatrix} (\mathbf{D}_{11}\mathbf{R}_{12}\mathbf{D}_{22}\mathbf{R}'_{12})^2 & \mathbf{0} \\ \mathbf{0} & (\mathbf{D}_{22}\mathbf{R}'_{12}\mathbf{D}_{11}\mathbf{R}_{12})^2 \end{bmatrix} \tag{4.20}$$

It also can be proved that the traces of $\mathbf{D}_{11}\mathbf{R}_{12}\mathbf{D}_{22}\mathbf{R}'_{12}$ and $\mathbf{D}_{22}\mathbf{R}'_{12}\mathbf{D}_{11}\mathbf{R}_{12}$ are the same and so are the traces of their square. Thus the dimension of matrix multiplication can be reduced by half (that one quarter in mathematic calculation amount).

It is interesting to note that there is a very concise formula for calculating t_1 of $\bar{\mathbf{A}}$:

$$t_1 = -\sum_{r_{ij} \neq 0} d_i d_j, \tag{4.21}$$

where r_{ij} are the entries of $\mathbf{R}$, d_i, d_j are the diagonals of $\mathbf{D}$. For the example in Fig. 4.2,

$$\begin{aligned} t_1 = -2(&\frac{1}{L_5C_1} + \frac{1}{L_5C_2} + \frac{1}{L_6C_2} + \frac{1}{L_7C_2} + \frac{1}{L_6C_3} \\ &+ \frac{1}{L_7C_3} + \frac{1}{L_7C_4}). \end{aligned} \tag{4.22}$$

In cases when only very rough estimation is needed, one can simply assume c_{n-2} in (4.6) is 0, then the upper bound can be selected as

$$\bar{\lambda} = \sqrt{c_{n-1}} = \sqrt{-t_1}, \tag{4.23}$$

which is very convenient to compute.

4.3.2 Degenerate circuit case

Although non-degenerate case has covered a lot of circuits in engineering application, there are still cases when degenerate circuit may occur, especially in three-phase power systems. Fig. 4.3(a) is a typical example of degenerate circuit in which C_1, C_2 and C_3 form a loop while L_4, L_5, and L_6 connect to a common node. In such cases, if all capacitors are simply viewed as voltage sources and all inductors as current sources, as shown in Fig. 4.3(b), their voltage-current relation can no longer be represented by an anti-symmetric matrix $\mathbf{R}$ because of the singularity of matrix $\mathbf{A}_1$ in the last chapter.

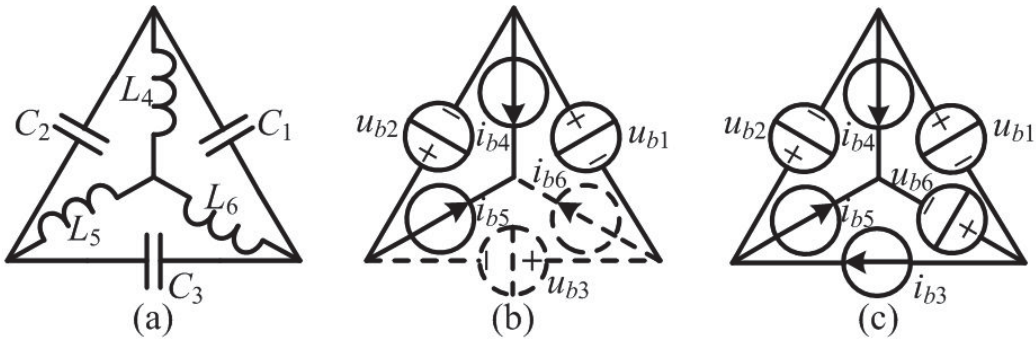

Figure 4.3: A degenerate circuit consisting of only capacitors and inductors.

To fix this problem, one branch of the capacitor loop should be viewed as current source and one branch of the inductor cutset should be viewed as voltage source, as illustrated in Fig. 4.3(c). Then their voltage/current relation can be developed following the same routine as in non-degenerate case, as shown in (4.24).

$$\begin{bmatrix} i_{b1} \\ i_{b2} \\ u_{b3} \\ u_{b4} \\ u_{b5} \\ i_{b6} \end{bmatrix} = \begin{bmatrix} 0 & 0 & \boxed{1} & -1 & -1 & 0 \\ 0 & 0 & \boxed{1} & 0 & -1 & 0 \\ \boxed{-1} & \boxed{-1} & 0 & 0 & 0 & 0 \\ 1 & 0 & 0 & 0 & 0 & \boxed{1} \\ 1 & 1 & 0 & 0 & 0 & \boxed{1} \\ 0 & 0 & 0 & \boxed{-1} & \boxed{-1} & 0 \end{bmatrix} \begin{bmatrix} u_{b1} \\ u_{b2} \\ i_{b3} \\ i_{b4} \\ i_{b5} \\ u_{b6} \end{bmatrix}. \tag{4.24}$$

Special attention should be given to the entries that are boxed. For the branches that are altered types (C_3, L_6), their voltage/current are the opposite of summation of all remaining branches' voltage/currents in the loop/cutset that make the circuit degenerate. Thus the entries (r_{ij}) of the rows that indicating these branches' voltage/current relation are either -1 or 0. If branch i and branch j are in the same degenerate loop/cutset, then $r_{ij} = -1$, otherwise $r_{ij} = 0$. In addition, because of the anti-symmetry of matrix $\mathbf{R}$, every -1 entry in these rows has an opposite entry at the anti-symmetric location in matrix $\mathbf{R}$. Just as the boxed entries are shown in (4.24).

When writing state-space equation of the degenerate circuit, the branches that are altered types can not be viewed as independent branch because their states can be represented by other branch's states. For the example in Fig. 4.3,

$$\begin{cases} i_{b3} = C_3 \dfrac{du_{b3}}{dt} = C_3 \dfrac{d(-u_{b1} - u_{b2})}{dt} = C_3 \left(-\dfrac{du_{b1}}{dt} - \dfrac{du_{b2}}{dt} \right), \\ u_{b6} = L_6 \dfrac{di_{b6}}{dt} = L_6 \dfrac{d(-i_{b4} - i_{b5})}{dt} = L_6 \left(-\dfrac{di_{b4}}{dt} - \dfrac{di_{b5}}{dt} \right). \end{cases} \tag{4.25}$$

while the other state equation can be written as usual,

$$\begin{cases} C_1 \dfrac{du_{b1}}{dt} = i_{b3} - i_{b4} - i_{b5} \\ C_2 \dfrac{du_{b2}}{dt} = i_{b3} - i_{b5} \\ L_4 \dfrac{di_{b4}}{dt} = u_{b1} + u_{b6} \\ L_5 \dfrac{di_{b5}}{dt} = u_{b1} + u_{b2} + u_{b6} \end{cases} . \tag{4.26}$$

Substituting (4.25) into (4.26), the state-space representation of Fig. 4.3 can be obtained,

$$\underbrace{\begin{bmatrix} C_1 + C_3 & C_3 & 0 & 0 \\ C_3 & C_2 + C_3 & 0 & 0 \\ 0 & 0 & L_4 + L_6 & L_6 \\ 0 & 0 & L_6 & L_5 + L_6 \end{bmatrix}}_{\mathbf{M}} \begin{bmatrix} \frac{du_{b1}}{dt} \\ \frac{du_{b2}}{dt} \\ \frac{di_{b4}}{dt} \\ \frac{di_{b5}}{dt} \end{bmatrix} =$$

$$\begin{bmatrix} 0 & 0 & -1 & -1 \\ 0 & 0 & 0 & -1 \\ 1 & 0 & 0 & 0 \\ 1 & 1 & 0 & 0 \end{bmatrix} \begin{bmatrix} u_{b1} \\ u_{b2} \\ i_{b4} \\ i_{b5} \end{bmatrix}. \tag{4.27}$$

Compared with (4.8), the matrix $\mathbf{M}$ on the left hand side is no longer a diagonal matrix, thus its inversion is not that explicit. However, there are two features of $\mathbf{M}$ that can be leveraged to simplify the solving process of its inversion. First, every degenerate loop/cutset is decoupled from each other, thus $\mathbf{M}$ can be partitioned into several square blocks on the diagonal so that the inversion of $\mathbf{M}$ is transformed into the inversion of these square blocks. Second, although these blocks are not diagonal matrix, they can be expressed as the summation of a diagonal matrix and a scalar times an all-ones matrix. For example,

$$\begin{bmatrix} C_1 + C_3 & C_3 \\ C_3 & C_2 + C_3 \end{bmatrix} = \begin{bmatrix} C_1 & 0 \\ 0 & C_2 \end{bmatrix} + C_3 \begin{bmatrix} 1 & 1 \\ 1 & 1 \end{bmatrix}. \tag{4.28}$$

This is actually a rank-1 modification of the original diagonal matrix. According to Sherman-Morrison's formula [54], the inversion of a rank-1 modification of the original matrix can be expressed as

$$\mathbf{M}^{-1} = (\mathbf{D} + \mathbf{uv})^{-1} = \mathbf{D}^{-1} - \sigma \mathbf{D}^{-1}\mathbf{uv}\mathbf{D}^{-1}, \tag{4.29}$$

where $\sigma = 1/(1 + \mathbf{v}\mathbf{D}^{-1}\mathbf{u})$ is a scalar.

Without loss of generality, assuming $\mathbf{M}$ has $n-1$ individual diagonals (m_1 to $m_{n-1}, n \geq 2$) and the same off-diagonal entries (m_n), then $\mathbf{D}$, $\mathbf{u}$ and $\mathbf{v}$ in (4.29) can be selected as

$$\begin{aligned} \mathbf{D} &= \begin{bmatrix} m_1 & 0 & \cdots & 0 \\ 0 & m_2 & \cdots & 0 \\ \vdots & \vdots & \ddots & \vdots \\ 0 & 0 & \vdots & m_{n-1} \end{bmatrix}, \\ \mathbf{u} &= m_n \begin{bmatrix} 1 \\ 1 \\ \vdots \\ 1 \end{bmatrix}, \mathbf{v} = \begin{bmatrix} 1 & 1 & \cdots & 1 \end{bmatrix}. \end{aligned} \tag{4.30}$$

The inversion of M can be derived as following:

$$\mathbf{M}^{-1} = \begin{bmatrix} \frac{1}{m_1} & 0 & \cdots & 0 \\ 0 & \frac{1}{m_2} & \cdots & 0 \\ \vdots & \vdots & \ddots & \vdots \\ 0 & 0 & \cdots & \frac{1}{m_{n-1}} \end{bmatrix} -$$

$$\frac{m_n}{1 + m_n \sum_{i=1}^{n-1} \frac{1}{m_i}} \begin{bmatrix} \frac{1}{m_1 m_1} & \frac{1}{m_1 m_2} & \cdots & \frac{1}{m_1 m_{n-1}} \\ \frac{1}{m_2 m_1} & \frac{1}{m_2 m_2} & \cdots & \frac{1}{m_2 m_{n-1}} \\ \vdots & \vdots & \ddots & \vdots \\ \frac{1}{m_{n-1} m_1} & \frac{1}{m_{n-1} m_2} & \cdots & \frac{1}{m_{n-1} m_{n-1}} \end{bmatrix}$$

$$= \frac{1}{\sum_{j=1}^{n} \prod_{\substack{i=1 \\ i \neq j}}^{n} m_i} \begin{bmatrix} \sum_{\substack{j=1 \\ j \neq 1}}^{n} \prod_{\substack{i=1 \\ i \neq j}}^{n} m_i & -\prod_{\substack{i=1 \\ i \neq 2}}^{n} m_i & \cdots & -\prod_{\substack{i=1 \\ i \neq n-1}}^{n} m_i \\ -\prod_{\substack{i=1 \\ i \neq 1}}^{n} m_i & \sum_{\substack{j=1 \\ j \neq 2}}^{n} \prod_{\substack{i=1 \\ i \neq j}}^{n} m_i & \cdots & -\prod_{\substack{i=1 \\ i \neq n-1}}^{n} m_i \\ \vdots & \vdots & \ddots & \vdots \\ -\prod_{\substack{i=1 \\ i \neq 1}}^{n} m_i & -\prod_{\substack{i=1 \\ i \neq 2}}^{n} m_i & \cdots & \sum_{\substack{j=1 \\ j \neq n-1}}^{n} \prod_{\substack{i=1 \\ i \neq j}}^{n} m_i \end{bmatrix}. \tag{4.31}$$

The above process of dealing with degenerate circuit is not hard to be promoted to more general case and a circuit lemma can be summarized.

Lemma 1: A degenerate circuit can be transformed into non-degenerate by the following steps if the loops/cutsets that make the circuit degenerate contain at least one capacitive/inductive branch. 1) Set the reference direction of the branches in the degenerate loops/cutsets identical*. 2) Select one capacitive/inductive branch in the degenerate loops/cutsets and remove it by viewing it as open/short circuit. 3) Add self-capacitance/inductance to every branch and mutual-capacitance/inductance to every two branches in these loops/cutsets. The added self- and mutual-capacitance/inductance value is the same with the capacitance/inductance value in the branch that is removed.

(*Setting the reference direction identical means the branch voltages in the loop form either a clockwise or anti-clockwise loop and the branch currents in the cutset either all flow into or all flow out the cutset. This is to make sure that the removed branch's voltage/current is the opposite of summation of all remaining branches' voltage/currents and to provide the reference direction for the added mutual-capacitance/inductance.)

When applying the above lemma to the most simple case, i.e., two capacitors connect in parallel or two inductors connect in series, it will result into one capacitor whose value is the sum of the two capacitors and one inductor whose value is the sum of the two inductors, which exactly coincide with the common sense.

Once the degenerate circuit has been transformed into non-degenerate circuit and the inversion of coefficient matrix M has been found by (4.31), the upper bound of eigenvalues of the degenerate circuit can be obtained following the same routine in Section 4.3.A.

4.4 Numerical Validation on EMI Filter

HFLL circuit is not rare in electrical application. The EMI filter is one typical example. It has found a large application in areas such as adjustable-speed drives, renewable energy, battery charging for electric vehicles, future more electric aircrafts, and others [76]. There are many papers in literature discussing derivation of the equivalent circuit model of EMI network [77]- [80]. These models are obtained either by impedance measurement and then parameter extraction or by advanced modeling methodology like finite element method and partial element equivalent circuit (PEEC) method. Few of them pay attention to the time-domain simulation of the equivalent circuit model, which is not easy for the existing simulation tools. For example, the time needed for a 55-μs transient simulation of a multi-conductor cable EMI equivalent circuit using SPICE is 3.6 s on a standard PC, as reported in [81], that's almost 65 thousand times slower than real-time.

To validate the effectiveness of the proposed time-step selection method, this chapter selects the EMI filter as an illustrating example because it is a typical HFLL circuit and needs to take the parasitic effects into account to reflect its attenuation performance. A three-phase EMI attenuation filter prototype is constructed and its 3-D model is developed in ANSYS, as shown in Fig. 4.4(a)-(b). The filter is composed of a first-stage common-mode inductor, followed by three X-capacitors in Δ-connection and the second-stage common-mode inductor, then three Y-capacitors in star-connection and finally a grounding capacitor. This filter is placed between a three-phase two-level converter and the AC grid to test its performance. The equivalent circuit of the experimental setup is shown in Fig. 4.4(c) where the parasitic resistors, capacitors and inductors in the windings and wires of the EMI filter are taken into account. The parasitic network of common-mode inductor is adopted from [76] and the parameters of these parasitic elements are extracted by

ANSYS Q3D tool using finite element method. This 3-D model is carefully constructed so that the lumped values of these parasitic elements can be accurately captured by ANSYS. Once the equivalent circuit of the EMI filter is obtained, the proposed method can be utilized to select an appropriate time-step for simulation.

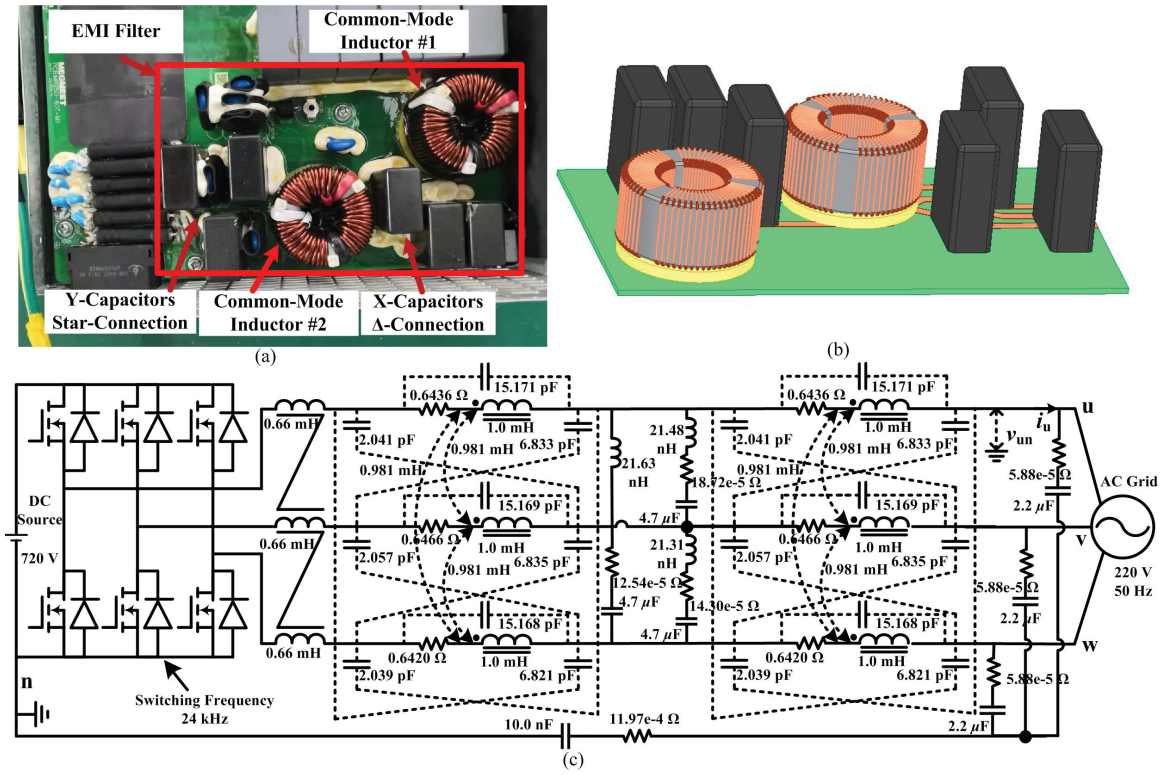

Figure 4.4: (a) Structure of the EMI filter prototype. (b) The filter's 3-D model in ANSYS. (c) The equivalent circuit of the test-bench.

As can be seen that, this is a typical HFLL circuit where the resistor values are very small. By neglecting the effect of these resistors, the upper bound of this circuit's eigenvalues can be found following the routine presented in Section 4.3, which is 3.3622×10^{9}. According to equation (4.5), the upper bound of the selected time step using RK4 solver is 8.4171×10^{-10} s.

The corresponding numerical simulation is conducted on Matlab platform using EZM with RK4 solver. The results are illustrated in Fig. 4.5(a) and (b), respectively. It has to be mentioned that although the resistors are neglected in the time-step selection analysis, they are not neglected when conducting the modeling and simulation because the dissipative effect is very important with regard to attenuating the high frequency noise. The last chapter explained in detail how to take care of these resistors.

The voltage v_{un} (grid side phase-u line to reference ground n at DC side) and

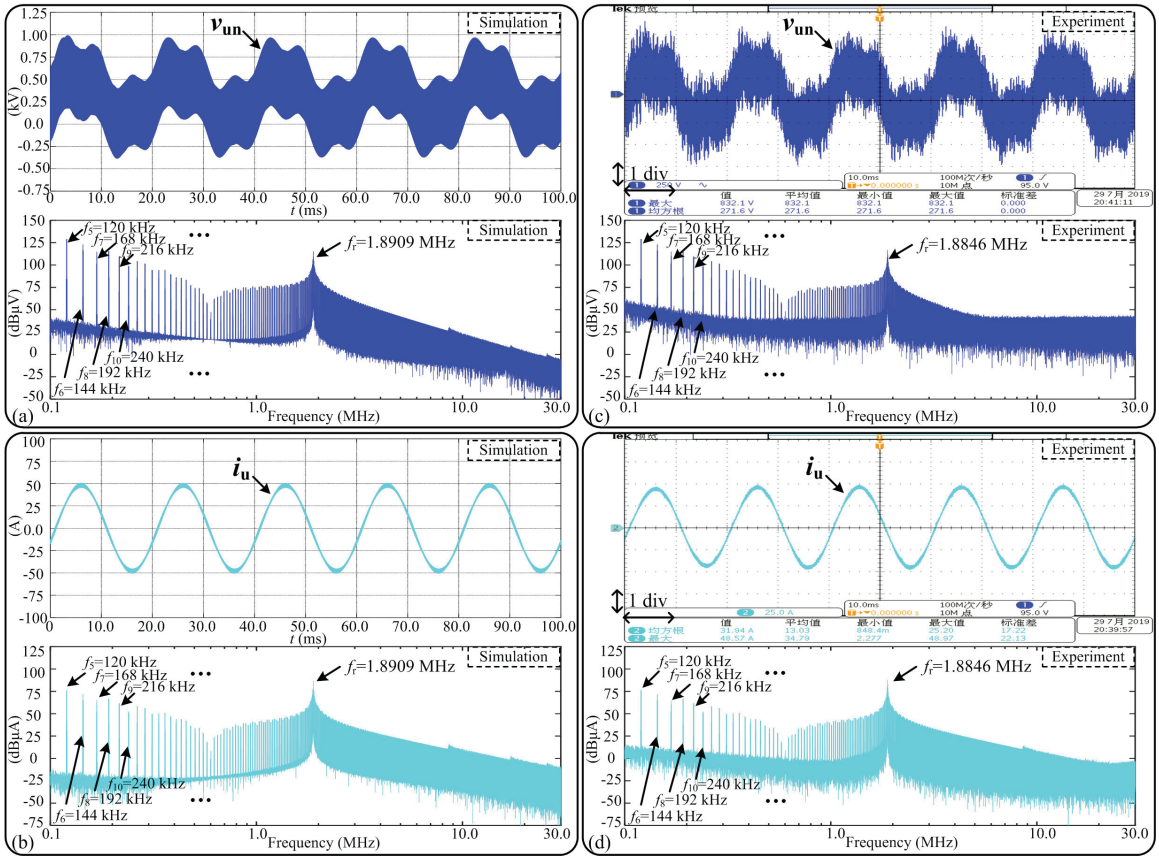

Figure 4.5: Time-domain and frequency domain comparison between the proposed time-step selection method based simulation and the experiment. (a)-(b) v_{un} and i_{u} from simulation; (c)-(d) v_{un} and i_{u} from experiment. (upper: time-domain waveform, x-axis: 10 ms/div, y-axis: 0.25 kV/div for voltage, 25 A/div for current. lower: high frequency spectrum, x-axis: log-scale from 100 kHz to 30 MHz, y-axis 25 dBμV/div for voltage, 25 dBμA/div for current)

current i_{u} are selected for frequency domain analysis. To make a complete evaluation, the high frequency spectrum (100 kHz to 30 MHz) are displayed in Fig. 4.5 for both simulation and experimental results. As can be seen that, there are several spikes distributed along the left half axis in the frequency spectrum. These spikes are aroused by the switching devices working at 24 kHz, which is a recognized phenomenon in power electronics analysis.

Most part of the high frequency spectrum are below 100 dBμV or 100 dBμA, except for a resonant peak at 1.8909 MHz in simulation spectrum and 1.8846 MHz in experimental spectrum. According to the analysis in [87], this can be explained by the resonance between parasitic capacitor C_p in common mode inductor and the parallel inductance of common mode inductor L_C and differential mode inductor L_D. Since there are two common mode inductors in the circuit, the resonance

frequency can be expressed as

$$f_r = \frac{1}{2\pi\sqrt{\frac{L_C L'_D}{2L_C+L'_D} \times C'_p}} = 1.8824 \text{ MHz}, \tag{4.32}$$

where $L_C = 1.0$ mH, $L'_D = 0.66/3 = 0.22$ mH, $C'_p = 3 \times (15.171 + 6.833 + 2.041) = 72.135$ pF. The reason L'_D is divided by 3 while C'_p is multiplied by 3 is because the three-phase L_D and C_p are connected in parallel in the common-mode equivalent circuit.

As a comparison, the same test-bench is also simulated using Maltab/Simulink's embedded solver and the results are similar with those in Fig. 4.5. The selected numerical method is the ODE23tb solver because it is the more efficient choice for stiff problems when a crude error tolerance is permitted [88]. Even though this is one of the most efficient solver in Matlab/Simulink, it is still much slower than the proposed time selection method with RK4 solver on this test-bench. To conduct the same 100.0 ms simulation in Fig. 4.5, the RK4 solver with 8.4171×10^{-10} s time-step consumes 902.7 s while the ODE23tb solver costs 15128.6 s on the same computer. The former is more than 16 times faster than the latter and also faster than some reported performance on EMI time-domain simulation like in [81] (9 thousand times v.s 65 thousand times slower than real-time).

The efficiency difference mainly results from the solver's computational complexity. RK4 solver is an explicit method so that no matrix inversion is required at every time-step calculation (the computation complexity remains $O(N^2)$) while ODE23tb is an implementation of trapezoidal rule with the second order backward difference formula (TR-BDF2), an implicit Runge-Kutta formula with two stages [88], and this makes its computation complexity in $O(N^3)$. Although the average time-step of ODE23tb solver (ODE23tb is a variable time-step method) is 1.205×10^{-9} s and larger than the one selected for RK4 solver, the implicit solver still consumes much more time than the explicit solver.

The experimental and simulation results agree with each other in very high degree, yet there are still some discrepancies between them and the theoretic analysis. The following factors may help explain the discrepancy. 1) Some nonlinear features like the saturation of inductors, the temperature varying phenomenon of capacitors and resistors are omitted. 2) The near-field coupling between inductors, inductors and capacitors and between capacitors, especially the coupling between the first filter stage and the second filter stage, could contribute to some differences. 3) There are some background noise in the experimental measurement. That's also

the reason spectrums from experiment do not attenuate in frequency higher than 5 MHz. 4) The above frequency domain results are obtained based on 10 ns sampling period, which is not the integer multiple of the solver's time-step. Therefore, linear interpolation has to be adopted to sample the signals at 10 ns interval. This may lead to some frequency spectrum distortions. Nevertheless, it is safe to say that the adopted numerical solver has achieved numerical stability along the whole simulation. The selected time-step is valid and superior than some traditional time-step selection schemes.

4.5 Summary

This chapter presented a fast method to select time-step for simulating high frequency low loss circuit using explicit solver. The state-space model analysis of HFLL circuit show that all its eigenvalues distribute on the imaginary-axis, thus transforming the time-step selection problem into finding the upper bound of these eigenvalues. The process of formulating non-degenerate and degenerate circuits' state-space model is elaborated and a transformation lemma from the former case into the latter case is presented. Time-step is selected based on the Laguerre-Samuelson's inequality, which involves only two matrix multiplications during the calculation. As a verification, the equivalent circuit of an EMI filter that takes into account the parasitic effects is extracted from ANSYS and a numerical simulation is conducted to compare the performance of the presented time-step selection manner. Numerical results show that the presented method is able to capture all major and parasitic features of the circuit while be much more (16 times) efficient in computation time than the traditional method. Experimental field test of the EMI filter in a DC/AC converter validates the effectiveness of the proposed method.

5

EZM Based Modular Assembly Modeling of More Electric Aircraft

5.1 Introduction

The more electric aircraft, as its name implies, aims at replacing as much parts of the pneumatic, hydraulic and mechanical system with electric system, which inevitably links different domain techniques together. A high fidelity model should be able to exhibit multidisciplinary characteristics of MEA. This is especially important for on-the-move system because its state will change along with geographical factors like altitude and distance. There are abundant literature modeling one or two domain aspects of MEA. [89]- [91] report the analysis of electrically-driven ECS which intakes air directly from atmosphere rather than high-temperature engine bleed-air. [8], [9], [10], [92] explain the modeling of electro-hydrostatic-actuator for position control. [11], [93], [94] illustrate the structure of electro-mechanical-actuator and its application for aircraft flight control. However, the comprehensive modeling incorporating all four domain characteristics still remains relatively rare in literature.

Modern engineering modeling advancements and achievements have evolved many excellent tools for simulating individual aspects of an engineering problem. They can provide wide-range results in terms of accuracy and efficiency when only one kind of physical phenomenon is of concern. However, engineering problems

usually involve multi-domain modeling. For example, when designing a motor drive system, not only the electrical behavior is of importance, the mechanical and thermal performance of the system should also be designed properly.

Although physical behaviors from different domains take different forms, there is one commonality: energy. Many engineering problems can be summarized in the category of energy conversion process, either within one domain (e.g. electrical energy from AC to DC by rectifier) or between two or more domains (e.g. from rotating kinetic energy to electrical energy by generator). In many cases, the energy conversion process can be described by differential-algebraic equations (DAEs).

From the mathematic point of view, as long as the physical behavior can be described by DAEs, the multi-domain simulation is no different in terms of numerical computation, regardless of the various energy forms. The solver from one physical area can be applied into another. Among some typical aspects of engineering phenomena, the electrical part usually has the smallest time-constant. The electrical transient can be as short as several microseconds or even lower to nanosecond level. That means if a unified solver for multi-domain problem is needed, the electrical system solver is most likely to be competent.

There are multiple choices for electrical system solver. The state-space method (also called state variable method) is no doubt a very good one. The state variables are the smallest possible subset of system variables that can represent the entire state of the system at any given time [95]. That means state-space model is a highly concise representation of the DAEs that describe the system. Consequently, the mathematic computations required for solving them are also reduced. On the other hand, it is just because of its conciseness and compactness that make the state variable model not easy to obtain. Therefore, an alternative method that can simplify the modeling process without increasing much computational burden is welcome in engineering simulation area. EZM achieved a good balance between modeling effort and computation effort, which makes it a suitable solver for multi-domain simulation.

Modular assembly is deemed as an effective strategy to cope with the modeling of multi-domain system. It is believed that the pneumatic, hydraulic and mechanical parts are linked only through the electric system and there is no direct influence between them. That is because MEA is designed under the power-by-wire (PBW) principle, i.e., all energy except the propulsion, is transformed into electric power first and is distributed to different parts by power wires. As a consequence, this complex architecture can be divided into several modules where each module con-

tains only one specific domain and electric domain model. The challenge then falls on how to correctly assemble these modules into one integral model in electric domain. This leads to another important feature of MEA on-board powertrains, that is multi-machine.

The utilization of electric power as the main source to actuate other domain systems introduces multiple machines into the MEA powertrains. For example, the ECS and ESHA are actuated by electric-driven compressors and pumps, respectively. The EMA also needs electric machines to manipulate ball-screw and push rods. Simulation of machines is an intensively studied topic and a widely accepted general-purpose model (dq model) can be used. The difficulty lies on how to interface it with external network. [96] made a comprehensive survey on the interfacing techniques that are utilized to integrate the general-purpose models of electrical machines with the rest of power system network. They can be classified into indirect approaches that fit for modified nodal analysis method and direct approaches that fit for state-space method.

Indirect approaches are those who do not interface machine using its original model but the post-transformed forms. Typical post-transformed forms include the Thevenin-equivalent, the Norton-equivalent and the compensation-based model. Generally speaking, these indirect approaches always try to keep a constant admittance matrix to avoid extra computation burden in solving the nodal analysis network. However, the machine is essentially a time-varying model and modifications like prediction and compensation have to be made to keep the admittance matrix constant. Those modifications always come with detrimental effects on accuracy and numerical stability of the model, especially when there are multiple machines in the system.

Direct approaches, on the other hand, integrate the machine and external network equations together to achieve simultaneous solution of the whole network, thus bringing no extra accuracy and numerical stability loss. Once the state-space model of the whole system is found, either explicit or implicit numerical integration method can be employed to solve it.

This chapter aims at achieving real-time emulation of the on-the-move multi-domain multi-machine system on more electric aircraft, wherein computational efficiency is a crucial factor when choosing emulation scheme. The indirect approaches shall not be taken into consideration not only because of their side effects on accuracy and numerical stability, but also the fact that the machines on MEA are driven by power electronic converters to reach better controlling performance

and avoid unnecessary energy waste. Even though the admittance matrices of the machines can be made constant, it is a tough task to do so for power converters. Moreover, the power lines on MEA are too short to be viewed as transmission lines that contain travel-time delay for decoupling. Therefore, direct approach is the selected modeling scheme.

This chapter is organized as following: Section 5.2 explains the multi-domain models of MEA exhibited in this real-time emulation. In specific, the electrically driven ECS, ESHA and EMA are selected as the example in pneumatic, hydraulic and mechanical domains, respectively. Section 5.3 analyzes the structure of multi-machine powertrains on MEA and derives the corresponding state-space model. Explicit integration method is adopted for solving the model because of its inherent natural suitability for parallel computation. To guarantee numerical stability of the explicit solver, bounds (both on real part and imaginary part) for eigenvalues of the multi-machine system are identified and a Monte-Carlo test is performed to testify the validity of the bounds. Section 5.4 gives a summary of the work in this chapter.

5.2 Modular Multi-Domain Models on MEA

The MEA on-board powertrain is a high complexity multi-domain system that it is very cumbersome to model it as a whole. The divide and conquer manner could be a feasible solution where the whole system is partitioned into several sub-modules that each module is only responsible for modeling the relationship of one specific domain with electric domain. There can be multiple instances of the same module but due to the fact that they are linked only through electric domain and the transients in pneumatic, hydraulic and mechanic systems are much slower than that in electric system, it is reasonable to leave the assembly task only in electric domain. This is the basic idea of modular assembly scheme adopted in this chapter. This section describes the multi-domain models used to exhibit in this real-time implementation on FPGA.

5.2.1 Electrically-Driven Environmental Control System

As the aircraft engines have become more sensitive to the extraction of bleed air [89], the electrically-driven ECS (E-ECS) which intakes ambient air as input reaps energy savings over using engine bleed air as it does not require a pressure reduction valve and, as the temperature of the pre-compressor is less than engine

bleed air, thus requiring less pre-cooling [2]. Moreover, the adjustable speed feature of electrical motors will allow further optimization of airplane energy usage by not requiring excessive energy from the supplied compressed air [4]. A simplified schematic diagram of electrically-driven ECS is shown in Fig. 5.1 where some advanced features such as humidity control, ozone remover are omitted.

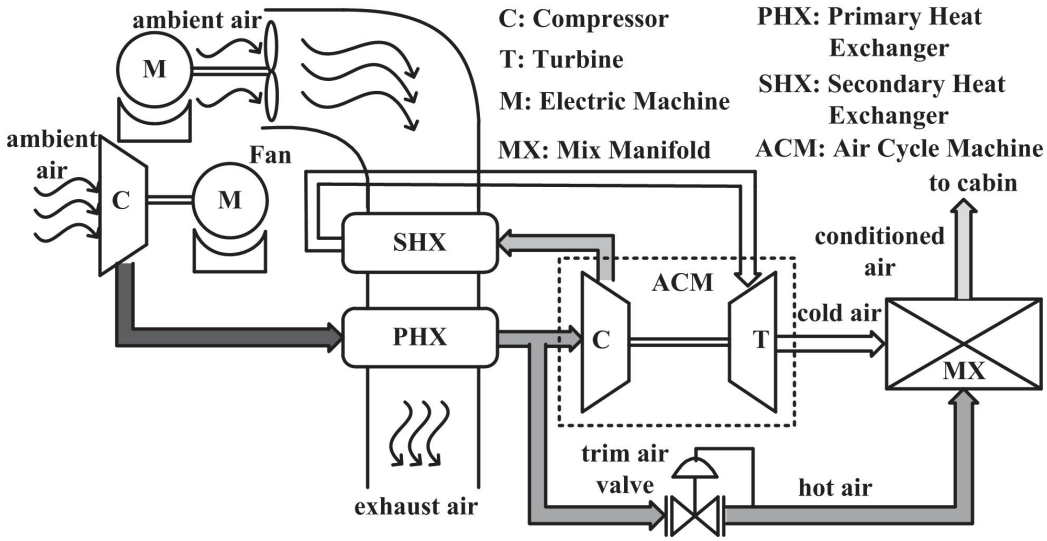

Figure 5.1: Schematic of a typical electrically-driven ECS.

The main parts of E-ECS include compressor and turbine, electric machine, fan, heat exchanger and mix manifold. The inlet of E-ECS is actuated by electric machine and it intakes the ambient air for two purposes: providing cooling flow for heat exchanger and generating pneumatic power (high temperature pressurized air) to air cycle machine (ACM) for post-processing. Noting that the temperature and pressure of ambient air are functions of aircraft altitude, thus the required electric power also changes along with aircraft mission profile (climb, cruise, descending, etc.)

The pneumatic part of E-ECS operates as an inverse Brayton cycle and can be described by the following equations.

5.2.1.1 Compressor and Fan

$$\begin{aligned} P_{\text{out}} &= PR \cdot P_{\text{in}}, \\ T_{\text{out}} &= T_{\text{in}} + \frac{T_{\text{in}}}{\eta_c}\left(PR^{\left(\frac{\gamma-1}{\gamma}\right)} - 1\right), \\ SP &= \dot{m} \cdot C_p \cdot (T_{\text{out}} - T_{\text{in}}), \end{aligned} \tag{5.1}$$

where P_{in}, T_{in} and P_{out},T_{out} are input, output pressure and temperature, respectively. PR is pressure ratio. $\dot{m}$ is mass flow rate and SP is shaft power. η_c, γ and C_p are constants referred as compressor/fan efficiency, air heat ratio and air heat capacity, respectively.

5.2.1.2 Turbine

$$\begin{aligned} T_{\text{out}} &= T_{\text{in}} - \frac{SP}{\dot{m} C_p}, \\ P_{\text{out}} &= P_{\text{in}} \left(1 - \frac{T_{\text{in}} - T_{\text{out}}}{\eta_t T_{\text{in}}}\right)^{\frac{\gamma}{\gamma-1}}, \end{aligned} \tag{5.2}$$

where η_t is turbine efficiency. All other variables have the same meaning as in (5.1). Noting that the turbine receives power from the shaft, called compressor-turbine matching, thus the shaft power comes from the compressor on the same shaft.

5.2.1.3 Heat Exchanger and Mixer Manifold

$$\begin{aligned} T_{\text{out}} &= \frac{\dot{m}_{\text{c}} \cdot T_{\text{c}} + \dot{m}_{\text{h}} \cdot T_{\text{h}}}{\dot{m}_{\text{c}} + \dot{m}_{\text{h}}}, \\ P_{\text{hx}} &= (1 - \epsilon_{\text{hx}}) \cdot P_{\text{in}}, \\ P_{\text{mx}} &= \frac{\dot{m}_c \cdot P_{\text{c}} + \dot{m}_h \cdot P_{\text{h}}}{\dot{m}_c + \dot{m}_h}, \end{aligned} \tag{5.3}$$

where $\dot{m}_{\text{c}}$, T_{c} and $\dot{m}_{\text{h}}$, T_{h} are mass flow rate and temperature of the cold and hot air, respectively. The output pressure of heat exchanger and mix manifold are determined by the second and third equation in (5.3), respectively where ϵ_{hx} is the pressure drop coefficient of heat exchanger.

The cabin temperature based on thermal balance is derived from the First Law of Thermodynamics, which is expressed as

$$\begin{aligned} \frac{\mathrm{d}T_{\text{cab}}}{\mathrm{d}t} &= \frac{q_{\text{mx}} + q_{\text{s}} + q_{\text{p}} + q_{\text{fu}}}{C_p \cdot \frac{P_{\text{cab}} \cdot V_{\text{cab}}}{T_{\text{cab}} \cdot R}}, \\ q_{\text{mx}} &= \dot{m}_{\text{mx}} C_p \left(T_{\text{mx}} - T_{\text{cab}}\right), \\ q_{\text{s}} &= A_{\text{win}} \cdot \cos(l) \phi(h), \\ q_{\text{p}} &= q_{\text{pp}} \cdot N_{\text{p}}, \\ q_{\text{fu}} &= \mu \left(T_{\text{cab}} - T_{\text{amb}}\right), \end{aligned} \tag{5.4}$$

where T_{cab}, P_{cab} and V_{cab} are cabin temperature, pressure and volume, respectively. R is the dry air gas constant. q_{mx} is the heat load introduced by E-ECS, i.e., the output of mix manifold. q_{s} is the heat load generated by solar radiation, which is function of cabin window area A_{win}, sunlight incidence angle l and an altitude function

$\phi(h)$. q_{p} is the heat load produced by passengers and crew members where q_{pp} is the average heat produced by one person and N_p is the total number of people on-board. q_{fu} represents the heat transfer between the fuselage and the ambient air where μ is the overall heat transfer coefficient and T_{amb} is the temperature of ambient air.

The cabin temperature is regulated by a trim air valve that controls the hot air entering the mix manifold. When the valve is on, hot air is added to the conditioned air and the raise of q_{mx} will increase T_{cab}. When the valve is off, the q_{mx} drops and results in decrease of T_{cab}. The temperature regulation is achieved by hysteresis control of the difference between the desired and actual temperature in the cabin.

5.2.2 Electro-Hydrostatic-Actuator

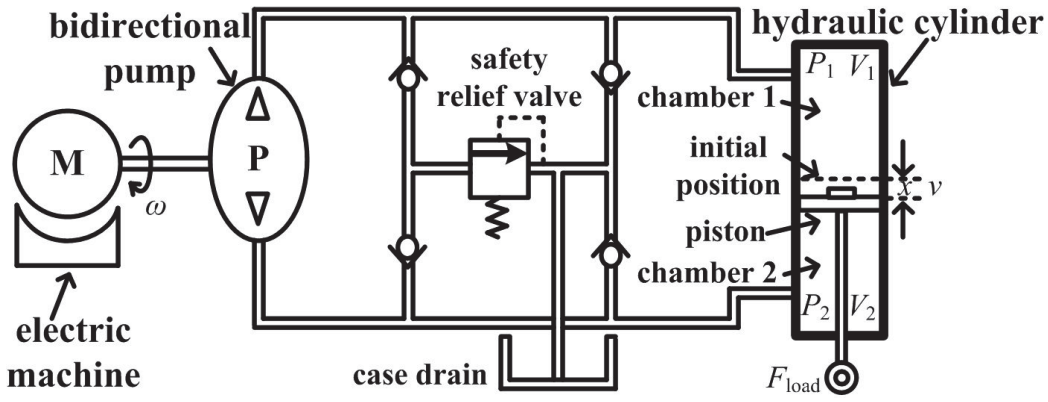

Figure 5.2: Schematic of a typical EHSA.

EHSA combines the benefits of conventional hydraulic systems and direct-drive electrical actuators, namely, high torque/mass ratio and modularity [9], as well as high energy efficiency, due to the fact that the pump works only on a movement demand and the actuating power is transferred by electricity (Power by Wire) instead of by the oil in the pipes (Power by Pipe) [10]. The structure of a typical EHSA is illustrated in Fig. 5.2. It is composed of an electric machine as the prime mover, a bidirectional pump regulating the oil flow in the pipes, a safety relief valve for over-pressure protection and a hydraulic cylinder that is split into two chambers to generate force from chamber pressure difference. The bidirectional fixed displacement gear pump is driven directly by the electric machine to realize high precision position control and fast system response.

There are one torque balance equation from machine-pump shaft (5.5), two oil flow continuity equations from each cylinder chamber (5.6)-(5.7), one force balance equation (5.8) and motion equation (5.9) from piston that are selected to describe the dynamics of EHSA, which are outlined as following:

$$J_M\dot{\omega} = T_E - T_P - T_{fr}(\omega), \tag{5.5}$$

$$Q_1 = Av + V_1\dot{P}_1/\beta + K_{lk}(P_1 - P_2), \tag{5.6}$$

$$Q_2 = Av - V_2\dot{P}_2/\beta + K_{lk}(P_1 - P_2), \tag{5.7}$$

$$A(P_1 - P_2) = m\dot{v} + F_{fr}(v) + F_{load}, \tag{5.8}$$

$$\dot{x} = v, \tag{5.9}$$

where J_M is the inertia on machine shaft, ω is the shaft rotating speed, T_E and T_P are electric torque from machine and hydraulic torque from pump, respectively. $T_{fr}(\omega)$ is the friction function on the shaft. Q_1, Q_2, P_1, P_2 and V_1, V_2 are the oil flow, pressure and volume in chamber 1 and 2, respectively. A is the area of piston surface, β is the bulk modulus of the oil, K_{lk} is the leakage coefficient of the cylinder. m, $F_{fr}(v)$ and F_{load} are the total mass, friction force and load force applied on the piston rod. v and x are piston movement velocity and displacement from initial position, respectively.

Apart from the above dynamic equations, each component has its own characteristics equation, which are

$$T_P = D(P_1 - P_2), \tag{5.10}$$

$$Q_{1,2} = D\omega - K_{lp}(P_1 - P_2), \tag{5.11}$$

$$V_1 = V_{10} + Ax, \tag{5.12}$$

$$V_2 = V_{20} - Ax, \tag{5.13}$$

where D is the volumetric pump displacement, K_{lp} is pump leakage coefficient. V_{10} and V_{20} are the initial volume of chamber 1 and 2, respectively.

$T_{fr}(\omega)$ and $F_{fr}(v)$ are two functions that use the LuGre model to capture friction phenomenon. The LuGre model contains only a few parameters but has the ability to model viscous friction, coulomb friction as well as Stribeck effect for predicting stick-slip motion, thus it can easily be matched to experimental data [97]. The LuGre model takes the form of (5.14),

$$L_{fr}(z) = \left(F_c + (F_s - F_c)\,e^{-|z/z_s|}\right)\operatorname{sgn}(z) + \sigma z, \tag{5.14}$$

where F_c and F_s are two constants corresponding to coulomb friction and stiction friction, respectively. z_s is a parameter determining how fast F_s approaches zero

and σ characterizes the viscous friction. There are only four parameters in the model, so it is convenient for experimental parameter identification.

Combining the derivative equations from (5.5)-(5.9) and the component characteristics equations from (5.10)-(5.13), the state-space model of the EHSA system can be obtained, which are written as following:

$$\begin{cases} \dot{\omega} = \dfrac{1}{J_M}\left(T_E - D\left(P_1 - P_2\right) - T_{fr}\left(w\right)\right) \\ \dot{P_1} = \dfrac{\beta}{V_{10} + Ax}\left(D\omega - K_l\left(P_1 - P_2\right) - Av\right) \\ \dot{P_2} = \dfrac{\beta}{V_{20} - Ax}\left(-D\omega + K_l\left(P_1 - P_2\right) + Av\right) \\ \dot{v} = \dfrac{1}{M}\left(A\left(P_1 - P_2\right) - F_{fr}\left(v\right) - F_{load}\right) \\ \dot{x} = v \end{cases}, \tag{5.15}$$

where $K_l = K_{lk} + K_{lp}$ is the combined leakage coefficient.

$T_{fr}\left(\omega\right)$ and $F_{fr}\left(v\right)$ are the major contributors of nonlinearities in the system that have significant effect on the start-up process, which will be demonstrated in later section.

5.2.3 Electro-Mechanical-Actuator

The electro-mechanical-actuator is an appealing candidate for flight control on MEA because of its benefits such as a decrease in maintenance effort and weight, and an increase in efficiency [11]. The aircraft flight control dynamics along with EMA performance is of great interests for system designers and engineers. In this section, an EMA serving as elevator for aircraft longitudinal control is selected as representative case-study, as shown in Fig. 5.3(a)-(b).

An EMA leverages on a gearbox and ball screw system to translate rotary motion into linear motion [94]. The linear motion changes the position of elevator surface and then affects the aircraft body correspondingly.

According to [98]- [99], the small-disturbance kinematics equations of aircraft

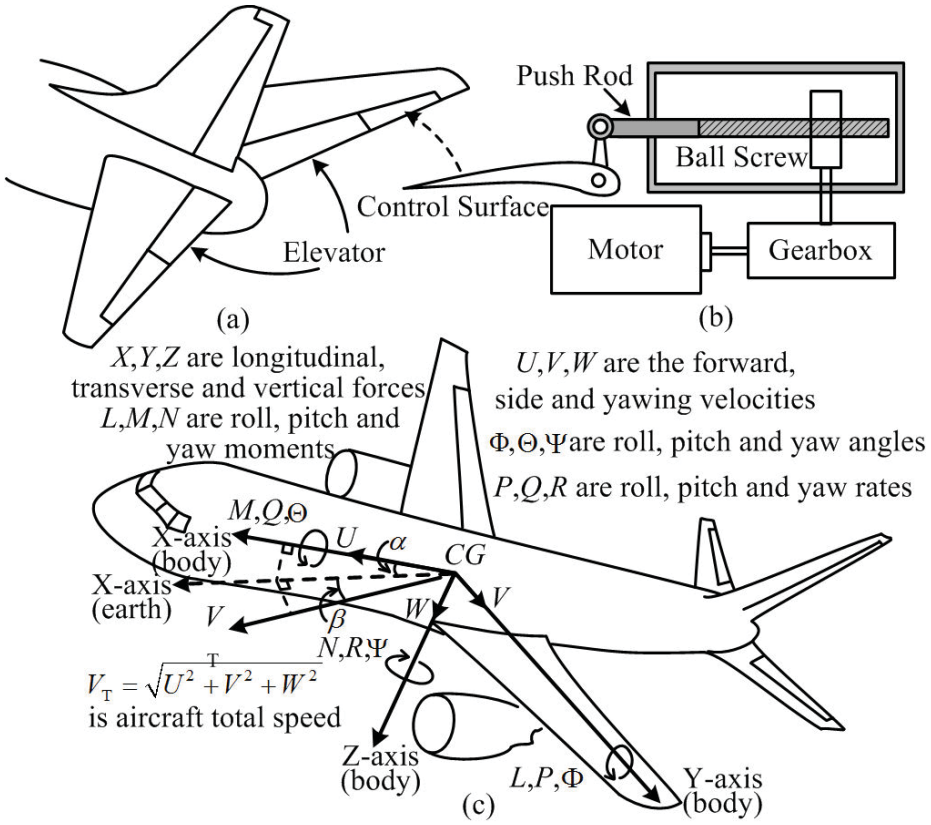

Figure 5.3: Schematic of a typical EMA and flight control model.

longitudinal motions from an equilibrium state can be expressed as

$$\begin{cases} m\left(\dot{u} + W_0 q - g\cos\Theta_0\theta\right) = \Delta X = \dfrac{\partial X}{\partial u}u + \dfrac{\partial X}{\partial w}w + \dfrac{\partial X}{\partial \delta_E}\delta_E \\ m\left(\dot{w} - U_0 q + g\sin\Theta_0\theta\right) = \Delta Z \\ \qquad\qquad = \dfrac{\partial Z}{\partial u}u + \dfrac{\partial Z}{\partial w}w + \dfrac{\partial Z}{\partial \dot{w}}\dot{w} + \dfrac{\partial Z}{\partial q}q + \dfrac{\partial Z}{\partial \delta_E}\delta_E \\ I_y\dot{q} = \Delta M = \dfrac{\partial M}{\partial u}u + \dfrac{\partial M}{\partial w}w + \dfrac{\partial M}{\partial \dot{w}}\dot{w} + \dfrac{\partial M}{\partial q}q + \dfrac{\partial M}{\partial \delta_E}\delta_E \\ \dot{\theta} = q \end{cases}, \tag{5.16}$$

where m is aircraft mass, I_y is its y-axis inertia. The meaning of other parameters can be found in Fig. 5.3(c). The subscript 0 represents the initial value at the selected equilibrium state while the lower case variable and prefix Δ means the small-scale perturbation corresponding to the upper case variables. The deviation of forces and moments ΔX, ΔZ and ΔM can be expressed as combined contribution of system states $[u, w, q, \theta]$ and input elevator control surface perturbation δ_E. The relevant partial derivatives are aerodynamic coefficients that can be estimated by wind tunnel tests or system identification based on logged experimental

data from the aircraft [100]. Some depending terms are omitted because they are generally insignificant, for example $\frac{\partial X}{\partial q}$ is ignored since q has negligible effect on u.

Based on (5.16), the state-space model of the small-disturbance aircraft longitudinal dynamics can be written in canonical form as follow

$$\begin{cases} \dot{u} = X_u u + X_w w + W_0 q - g\cos\Theta_0\theta + X_{\delta_E}\delta_E \\ \dot{w} = Z_u u + Z_w w + U_0 q - g\sin\Theta_0\theta + Z_{\delta_E}\delta_E \\ \dot{q} = (M_u + M_{\dot{w}}Z_u)u + (M_w + M_{\dot{w}}Z_w)w \\ \qquad + (M_q + M_{\dot{w}}U_0)q - M_{\dot{w}}g\sin\Theta_0\theta + M_{\delta_E}\delta_E \\ \dot{\theta} = q \end{cases}, \tag{5.17}$$

where $[u, w, q, \theta]$ is system state vector, δ_E is input control variable associated with elevator position and the following notations are used:

$$X_x = \frac{1}{m}\frac{\partial X}{\partial x}, Z_x = \frac{1}{m}\frac{\partial Z}{\partial x}, M_x = \frac{1}{I_y}\frac{\partial M}{\partial x},$$

where x can be system state or input variable.

5.2.4 Thermal Model of the PMSM

Motors should be operated without the risk for demagnetization of the magnets and/or stator winding failure [101]. The temperature rise in electric machine might exceed insulation material limit and lead to either failure of insulation or accelerated aging effect [102]. Therefore, the thermal analysis model for PMSM in the actuator system is considered in this subsection. The model is mainly adopted from [103] and will be discussed briefly here. Fig. 5.4 depicts the typical structure of PMSM and the equivalent lumped parameter thermal network (LPTN).

Lumped-circuit thermal model is fast in computation and have been extensively utilized and validated on numerous machine types and operating points [104]. In the adopted model, the machine is roughly divided into four parts: stator yoke, stator teeth, stator winding and permanent magnet. Each of them is represented by a node in the equivalent network and the corresponding voltages with respect to the reference (ground) $\vartheta_{\mathrm{SY}}, \vartheta_{\mathrm{SW}}, \vartheta_{\mathrm{ST}}, \vartheta_{\mathrm{PM}}$ represent the temperatures in these components. The temperatures of cooling liquid and ambient are assumed to be constant and represented by voltage sources $\vartheta_{\mathrm{C}}, \vartheta_{\mathrm{A}}$ in the LPTN, respectively. The capacitances $C_{\mathrm{SY}}, C_{\mathrm{SW}}, C_{\mathrm{ST}}, C_{\mathrm{PM}}$ are used to model the thermal capacity of each component and the resistors are used to describe the heat transfer between

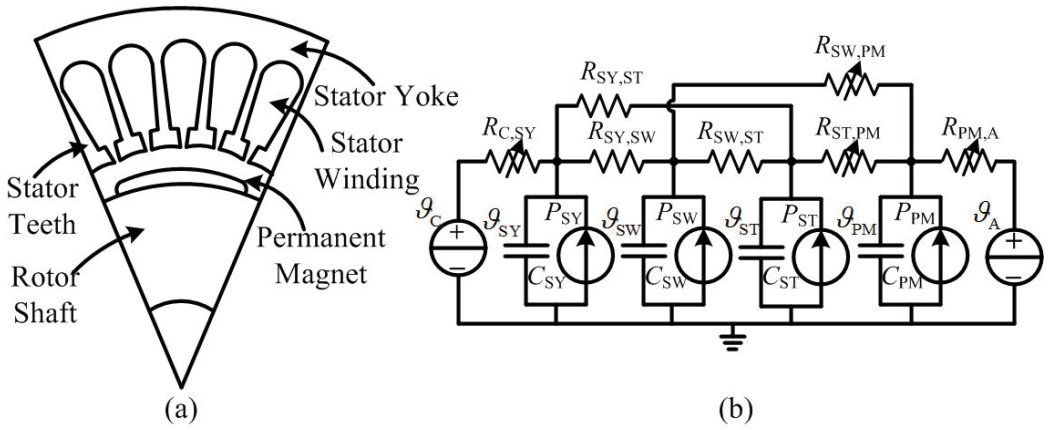

Figure 5.4: (a) Typical structure of PMSM; (b) The equivalent lumped parameter thermal network.

two components. Among the resistors, $R_{\mathrm{SW,SY}}, R_{\mathrm{SW,ST}}, R_{\mathrm{SY,ST}}$ are constant because they represent the conduction heat transfer within the stationary parts, while $R_{\mathrm{C,SY}}, R_{\mathrm{SW,PM}}, R_{\mathrm{ST,PM}}, R_{\mathrm{PM,A}}$ are varying with temperature because moving parts and convection process are taken into account [103]. Thus, the thermal model is a linear parameter-varying (LPV) system and the parameters are obtained based on material and size information of PMSM as well as system identification according to experimental data. It has to mention that solving LPV system is one of the strengths of EZM because of its full decoupling nature on all circuit branches. Only matrix multiplication is involved (no matrix inversion) in EZM's computation process and it is known that the computation effort of matrix multiplication is not sensitive to parameter-varying. By proper selection and identification of these parameters, good estimation accuracy regarding the considered components can be achieved, which makes this model very suitable for on-line monitoring and protection.

5.3 Assembly Analysis of Multi-Machine System

Once the sub-systems involving each domain with electric domain are transformed into modular models, the next task should be assembling them into an integrated model. This section deals with the eigenvalue analysis of power electronic converter based multi-machine drive system so as to provide facility for solving it in real-time using parallel algorithm on FPGA.

Fig. 5.5(a) depicts the general structure of the multi-machine drive system on MEA. This system is fed by a rippled DC voltage source that is converted from AC

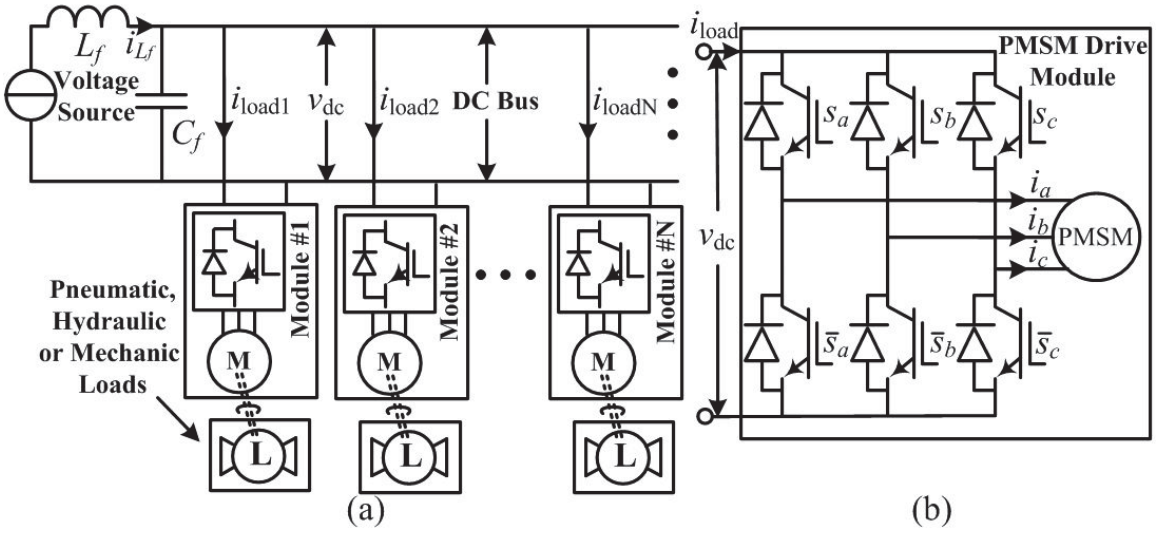

Figure 5.5: General structure of the multi-machine drive system on MEA.

bus by auto transformer rectifier unit (ATRU). The rippled DC voltage is smoothed by an LC filter and then feds the DC bus. The multiple machine drive systems are connected in parallel on the DC bus while the other domain systems are linked with the electric system through the machine shaft so that they can be viewed as torque loads applied on the shaft.

The multi-machine drive system is generally regarded as a very complicated structure that high fidelity modeling requires much effort. To simplify the analysis process yet still attain some constructive conclusions, the following assumptions are made.

(1) The internal impedance of the DC source in the system is deemed negligible or insignificant compared with the LC filter so that it can be viewed as "ideal" source.

(2) The transients of the torque loads generated by the pneumatic, hydraulic and mechanical system are much slower so they have negligible impact on the electric system transients (eigenvalues).

The above assumptions are generally true except for some extreme cases. It would suffice to yield insightful results in most cases such as performance evaluation, control parameter tunning, etc. It is a good compromise between accuracy and complexity in terms of mathematic modeling.

Before analyzing the eigenvalues of multi-machine drive system, it is necessary to clarify the single machine drive system as the first step. The permanent magnet synchronous machine (PMSM) is viewed as the best suited type for applications on

MEA because of its high power density and torque-to-inertia ratio as well as low losses [105]. Therefore, the three-phase two-level converter PMSM drive system depicted in Fig 5.5(b) is selected as the module structure for study. A PMSM can be described by the following dq equivalent circuit equations:

$$\begin{cases} v_d = r_s i_d - \lambda_q \omega + \dot{\lambda}_d \\ v_q = r_s i_q + \lambda_d \omega + \dot{\lambda}_q \\ v_0 = r_s i_0 + \dot{\lambda}_0 \\ 0 = r'_{kd} i'_{kd} + \dot{\lambda}'_{kd} \\ 0 = r'_{kq} i'_{kq} + \dot{\lambda}'_{kq} \end{cases}, \quad \begin{cases} \lambda_d = L_d i_d + L_{md} i'_{kd} + \lambda'_m \\ \lambda_q = L_q i_q + L_{mq} i'_{kq} \\ \lambda_0 = L_{ls} i_0 \\ \lambda'_{kd} = L_{md} i_d + L'_{kd} i'_{kd} + \lambda'_m \\ \lambda'_{kq} = L_{mq} i_q + L'_{kq} i'_{kq} \end{cases}, \tag{5.18}$$

where v, λ, L and r represents winding voltage, flux, inductance and resistance, respectively. The subscripts d, q and s denote d, q axis and stator winding parameters, respectively while subscripts k and m denote damper winding and mutual parameters. The superscript $'$ means the parameter is stator side equivalent. λ'_m is the flux induced by permanent magnet and can be viewed as constant. $\omega = \dot{\theta}$ is electrical angular velocity and is equal to the derivative of electrical rotor angular position θ.

The d and q axis variables and a, b, c axis variables can be transformed using the well known Park's and inverse Park's transformation, which can be found in [106].

$$\begin{aligned} \begin{bmatrix} x_d \\ x_q \\ x_0 \end{bmatrix} &= \frac{2}{3} \begin{bmatrix} \cos(\theta) & \cos\left(\theta - \frac{2}{3}\pi\right) & \cos\left(\theta + \frac{2}{3}\pi\right) \\ -\sin(\theta) & -\sin\left(\theta - \frac{2}{3}\pi\right) & -\sin\left(\theta + \frac{2}{3}\pi\right) \\ 1 & 1 & 1 \end{bmatrix} \begin{bmatrix} x_a \\ x_b \\ x_c \end{bmatrix} \\ \begin{bmatrix} x_a \\ x_b \\ x_c \end{bmatrix} &= \begin{bmatrix} \cos(\theta) & -\sin(\theta) & 1 \\ \cos\left(\theta - \frac{2}{3}\pi\right) & -\sin\left(\theta - \frac{2}{3}\pi\right) & 1 \\ \cos\left(\theta + \frac{2}{3}\pi\right) & -\sin\left(\theta + \frac{2}{3}\pi\right) & 1 \end{bmatrix} \begin{bmatrix} x_d \\ x_q \\ x_0 \end{bmatrix} \end{aligned} \tag{5.19}$$

As a result, the dq axis applied voltages and the load current that a machine extracted from the DC bus can be expressed as:

$$\begin{aligned} v_d =& f_1(\theta, s_a, s_b, s_c) v_{\mathrm{dc}} \\ =& \frac{2}{3}\left[\cos(\theta)\, s_a + \cos\left(\theta - \frac{2}{3}\pi\right) s_b + \cos\left(\theta + \frac{2}{3}\pi\right) s_c\right] v_{\mathrm{dc}}, \\ v_q =& f_2(\theta, s_a, s_b, s_c) v_{\mathrm{dc}} \\ =& -\frac{2}{3}\left[\sin(\theta)\, s_a + \sin\left(\theta - \frac{2}{3}\pi\right) s_b + \sin\left(\theta + \frac{2}{3}\pi\right) s_c\right] v_{\mathrm{dc}}, \end{aligned}$$

$$
\begin{aligned}
v_0 =& f_3(\theta, s_a, s_b, s_c) v_{\mathrm{dc}} = \frac{2}{3}\left(s_a + s_b + s_c\right) v_{\mathrm{dc}}, \\
i_{\mathrm{load}} &= s_a i_a + s_b i_b + s_c i_c = f_1 i_d + f_2 i_q + f_3 i_0 \\
&= f_1 \frac{L'_{kd}\lambda_d - L_{md}\lambda'_{kd} + (L_{md} - L'_{kd})\lambda'_m}{\sigma_d} \\
&\quad + f_2 \frac{L'_{kq}\lambda_q - L_{mq}\lambda'_{kq}}{\sigma_q} + f_3 \frac{\lambda_0}{L_{ls}},
\end{aligned} \tag{5.20}
$$

where s_a, s_b and s_c are switching signals of the upper arm switch in each phase. They are either 1 or 0, representing switch on and off state, respectively. $f_1(\theta, s_a, s_b, s_c)$, $f_2(\theta, s_a, s_b, s_c)$ and $f_3(s_a, s_b, s_c)$ (denoted as f_1, f_2 and f_3 henceforth), are three functions of switching signals and θ whose expressions can be found in (5.20) and $\sigma_d = L'_{kd}L_d - L^2_{md}$, $\sigma_q = L'_{kq}L_q - L^2_{mq}$.

Combining (5.18) and (5.20), the state-space form of single PMSM drive system is derived:

$$
\begin{bmatrix} \dot{\boldsymbol{\lambda}} \\ \dot{v_{\mathrm{dc}}} \end{bmatrix} = \begin{bmatrix} \mathbf{A}_{11} & \mathbf{A}_{12} \\ \mathbf{A}_{21} & 0 \end{bmatrix} \begin{bmatrix} \boldsymbol{\lambda} \\ v_{\mathrm{dc}} \end{bmatrix} + \mathbf{B}\lambda'_m, \tag{5.21}
$$

where

$$
\begin{aligned}
\boldsymbol{\lambda} &= \begin{bmatrix} \lambda_d \\ \lambda_q \\ \lambda_0 \\ \lambda'_{kd} \\ \lambda'_{kq} \end{bmatrix}, \mathbf{A}_{11} = \begin{bmatrix} -\frac{r_s L'_{kd}}{\sigma_d} & \omega & 0 & \frac{r_s L_{md}}{\sigma_d} & 0 \\ -\omega & -\frac{r_s L'_{kq}}{\sigma_q} & 0 & 0 & \frac{r_s L_{mq}}{\sigma_q} \\ 0 & 0 & -\frac{r_s}{L_{ls}} & 0 & 0 \\ \frac{r'_{kd} L_{md}}{\sigma_d} & 0 & 0 & -\frac{r'_{kd} L_d}{\sigma_d} & 0 \\ 0 & \frac{r'_{kq} L_{mq}}{\sigma_q} & 0 & 0 & -\frac{r'_{kq} L_q}{\sigma_q} \end{bmatrix}, \\
\mathbf{A}_{12} &= \begin{bmatrix} f_1 \\ f_2 \\ f_3 \\ 0 \\ 0 \end{bmatrix}, \mathbf{A}_{21} = \begin{bmatrix} -\frac{L'_{kd}}{\sigma_d C_f} f_1 \\ -\frac{L'_{kq}}{\sigma_q C_f} f_2 \\ -\frac{1}{L'_{ls} C_f} f_3 \\ \frac{L_{md}}{\sigma_d C_f} f_1 \\ \frac{L_{mq}}{\sigma_q C_f} f_2 \end{bmatrix}^{\mathrm{T}}, \mathbf{B} = \begin{bmatrix} -\frac{r_s (L_{md} - L'_{kd})}{\sigma_d} \\ 0 \\ 0 \\ -\frac{r'_{kd}(L_{md} - L_d)}{\sigma_d} \\ 0 \\ -\frac{L_{md} - L'_{kd}}{\sigma_d C_f} f_1 \end{bmatrix},
\end{aligned} \tag{5.22}
$$

and the superscript T means matrix transpose.

Accordingly, the state-space model of the multi-machine drive system linked

by a common DC bus can be written as

$$\begin{bmatrix} \dot{\boldsymbol{\lambda}}^1 \\ \dot{\boldsymbol{\lambda}}^2 \\ \vdots \\ \dot{\boldsymbol{\lambda}}^N \\ \dot{v}_{\mathrm{dc}} \\ \dot{i}_{L_f} \end{bmatrix} = \underbrace{\begin{bmatrix} \mathbf{A}_{11}^{(1)} & \mathbf{0} & \cdots & \mathbf{0} & \mathbf{A}_{12}^{(1)} & \mathbf{0} \\ \mathbf{0} & \mathbf{A}_{11}^{(2)} & \cdots & \mathbf{0} & \mathbf{A}_{12}^{(2)} & \mathbf{0} \\ \vdots & \vdots & \ddots & \vdots & \vdots & \vdots \\ \mathbf{0} & \mathbf{0} & \cdots & \mathbf{A}_{11}^{(N)} & \mathbf{A}_{12}^{(N)} & \mathbf{0} \\ \mathbf{A}_{21}^{(1)} & \mathbf{A}_{21}^{(2)} & \cdots & \mathbf{A}_{21}^{(N)} & 0 & \frac{1}{C_f} \\ \mathbf{0} & \mathbf{0} & \cdots & \mathbf{0} & -\frac{1}{L_f} & 0 \end{bmatrix}}_{\mathbf{A}_{(5N+2)\times(5N+2)}} \begin{bmatrix} \boldsymbol{\lambda}^1 \\ \boldsymbol{\lambda}^2 \\ \vdots \\ \boldsymbol{\lambda}^N \\ v_{\mathrm{dc}} \\ i_{L_f} \end{bmatrix} \tag{5.23}$$

where the superscript n ($1 \leq n \leq N$) denotes the nth module state variables in the system. They have the same form and meaning with that in (5.22). The input matrix $\mathbf{B}$ associated with λ'_m and voltage source are omitted because they have no effect on system eigenvalues.

As can be seen that all the block matrices $\mathbf{A}_{11}^{(k)}$, $\mathbf{A}_{12}^{(k)}$ and $\mathbf{A}_{21}^{(k)}$ are time-varying as different modules may have different angular velocities (ω) and switching states (f_1, f_2, f_3). Therefore, it is not advisable to solve it using some implicit numerical methods like the Trapezoidal method because they need to conduct matrix division or its equivalent at every time-step, thus making the computational complexity grow by $O(N^3)$. On the other hand, the explicit methods only need matrix multiplication and can be decomposed into parallel steps, which are very suitable to be implemented on FPGA for real-time emulation purpose.

However, one limitation that explicit methods have in common is the bounded numerical stability region. It is required that all the eigenvalues of the system times time-step must locate within the stability region. Therefore, ascertaining the system eigenvalue bounds becomes necessary before selecting the appropriate numerical method and time-step.

Since there are infinite variations of $\mathbf{A}$, it is impractical to find all its possible eigenvalues. However, there are some properties of $\mathbf{A}$ that can be leveraged to seek its eigenvalue bounds.

First of all, $\mathbf{A}$ can be decomposed into the sum of two matrices $\mathbf{A} = \mathbf{A_1} + \mathbf{A_2}$,

where

$$\mathbf{A}_1 = \begin{bmatrix} \mathbf{A}_{11}^1 & \mathbf{0} & \cdots & \mathbf{0} & \mathbf{0}\,\mathbf{0} \\ \mathbf{0} & \mathbf{A}_{11}^2 & \cdots & \mathbf{0} & \mathbf{0}\,\mathbf{0} \\ \vdots & \vdots & \ddots & \vdots & \vdots\,\vdots \\ \mathbf{0} & \mathbf{0} & \cdots & \mathbf{A}_{11}^N & \mathbf{0}\,\mathbf{0} \\ \mathbf{0} & \mathbf{0} & \cdots & \mathbf{0} & 0\;0 \\ \mathbf{0} & \mathbf{0} & \cdots & \mathbf{0} & 0\;0 \end{bmatrix}, \quad \mathbf{A}_2 = \begin{bmatrix} \mathbf{0} & \mathbf{0} & \cdots & \mathbf{0} & \mathbf{A}_{12}^1 & \mathbf{0} \\ \mathbf{0} & \mathbf{0} & \cdots & \mathbf{0} & \mathbf{A}_{12}^2 & \mathbf{0} \\ \vdots & \vdots & \ddots & \vdots & \vdots & \vdots \\ \mathbf{0} & \mathbf{0} & \cdots & \mathbf{0} & \mathbf{A}_{12}^N & \mathbf{0} \\ \mathbf{A}_{21}^1 & \mathbf{A}_{21}^2 & \cdots & \mathbf{0} & 0 & \frac{1}{C_f} \\ \mathbf{0} & \mathbf{0} & \cdots & \mathbf{0} & -\frac{1}{L_f} & 0 \end{bmatrix}.$$

Special attention should be given to $\mathbf{A}_2$ because 1) $\mathbf{A}_2$ has rank of only 2; and 2) $\mathbf{A}_2$ is a bipartite matrix, regardless of how $\mathbf{A}_{12}^{(k)}$ and $\mathbf{A}_{21}^{(k)}$ vary. A matrix $\mathbf{M}_{n\times n}$ is bipartite when it is possible to partition $\{1, 2, ..., n\}$ into two sets V_1 and V_2 so that for every $m_{ij} \neq 0$ in $\mathbf{M}$, i and j separately belong to V_1 and V_2 (i.e. i and j will not be in the same set).

It is clear that one feasible partition for $\mathbf{A}_2$ is placing $(5N + 1)$ in V_1 and placing 1 to $(5N + 2)$ except $(5N + 1)$ in V_2. According to [107], if μ is an eigenvalue of a bipartite matrix $\mathbf{M}$ with multiplicity k, then $-\mu$ is also an eigenvalue of $\mathbf{M}$ with multiplicity k. Considering the fact that $\mathbf{A}_2$ has only two nonzero eigenvalues, they must appear in conjugate pairs because $\mathbf{A}_2$ is real and they are opposite numbers because $\mathbf{A}_2$ is bipartite, then there is only one possibility: they are two pure imaginary numbers $\pm j\gamma$. More importantly, $\mathbf{A}_2$ is diagonalizable because the algebraic multiplicity of every eigenvalue equals its geometric multiplicity ($\pm j\gamma$ have multiplicity 1 and eigenvalue 0 has multiplicity $5N$). Therefore, there exists a nonsingular matrix $\mathbf{P}$ so as to make $\mathbf{PA_2P}^{-1}$ a diagonal matrix with its eigenvalues on the diagonal entries. Moreover, it is not prohibitive to conduct the same similarity transformation on $\mathbf{A}$ since it will not change the eigenvalues.

$$\begin{aligned} \bar{\mathbf{A}} = \mathbf{PAP}^{-1} &= \mathbf{PA_1P}^{-1} + \mathbf{PA_2P}^{-1} = \bar{\mathbf{A}}_1 + \bar{\mathbf{A}}_2 \\ &= \mathbf{PA_1P}^{-1} + \begin{bmatrix} j\gamma & 0 & \mathbf{0} \\ 0 & -j\gamma & \mathbf{0} \\ \mathbf{0} & \mathbf{0} & \mathbf{0}_{(5N\times 5N)} \end{bmatrix}, \end{aligned} \tag{5.24}$$

where $\bar{\mathbf{A}}_2$ is a diagonal matrix which is similar to $\mathbf{A}_2$.

According to [108], if μ is an eigenvalue of $\mathbf{M}_1 + \mathbf{M}_2$, then $\mu \in F(\mathbf{M}_1) + F(\mathbf{M}_2)$, where $F(\mathbf{M})$ is called the field of values defined as $F(\mathbf{M}) \equiv \{\mathbf{x}^*\mathbf{Mx} \mid \mathbf{x}$ is a complex vector and $\mathbf{x}^*\mathbf{x} = 1\}$. Obviously, $F(\bar{\mathbf{A}}_2)$ is a closed interval between $[-j\gamma, j\gamma]$ on

the imaginary axis. Then the eigenvalues of $\bar{\mathbf{A}}$ must locate within the union area that $F(\bar{\mathbf{A}}_1)$ move upward and downward along the imaginary-axis (vertically) for a length γ. Hence, the problem comes down to identifying $F(\bar{\mathbf{A}}_1)$ or equivalently, $F(\mathbf{A}_1)$. The following two theorems in [109] and [110] can help:

Theorem 1: If $\mathbf{M} = \mathbf{H}_1 + j\mathbf{H}_2$ with $\alpha_1 \leq \alpha_2 \leq \cdots \leq \alpha_n$ the eigenvalues of $\mathbf{H}_1$ and $\beta_1 \leq \beta_2 \leq \cdots \leq \beta_n$ the eigenvalues of $\mathbf{H}_2$, then the points of $F(\mathbf{M})$ lie in the interior or on the boundary of the rectangle constructed by the lines $\xi = \alpha_1, \xi = \alpha_n; \eta = \beta_1, \eta = \beta_n$ positioned parallel to the axes, where $\mathbf{H}_1$ and $\mathbf{H}_2$ are two hermitian matrices defined as: $\mathbf{H}_1 = (\mathbf{M} + \mathbf{M}^*)/2, \mathbf{H}_2 = (\mathbf{M} - \mathbf{M}^*)/(2j)$.

Theorem 2: Let $\mathbf{M}$ be an $n \times n$ complex matrix with real eigenvalues $\mu(\mathbf{M})$, and let $m = \mathrm{tr}(\mathbf{M})/n, s^2 = \mathrm{tr}(\mathbf{M}^2)/n - m^2$, then $m - s(n-1)^{1/2} \leq \mu(\mathbf{M}) \leq m + s(n-1)^{1/2}$, where tr means trace of the matrix.

Since $\mathbf{A}_1$ is a diagonal block matrix, the eigenvalue identifying can be conducted block-wise and then synthesize. In other words, the max/min eigenvalue of $\mathbf{A}_1$ is the max/min eigenvalue among all its blocks $\mathbf{A}_{11}^{(k)}$. It is worth mentioning that the real part bounds (α_1 and α_n) of $\mathbf{A}_{11}$ are invariant with angular velocity ω. They are determined only by machine electrical parameters (r, L, σ, etc.). While the imaginary part bounds ($\beta_n = -\beta_1 = \beta(\omega)$) are functions of ω:

$$\beta(\omega) = \sqrt{\frac{2}{5}\omega^2 + \frac{1}{10}\left(\frac{r_s - r'_{kd}}{\sigma_d} L_{md}\right)^2 + \frac{1}{10}\left(\frac{r_s - r'_{kq}}{\sigma_q} L_{mq}\right)^2}. \tag{5.25}$$

The upper bound $\bar{\beta}$ is achieved when ω equals the maximum angular velocity ω_m.

Meanwhile, the imaginary interval of $\mathbf{A}_2$ can be written as

$$\gamma = \sqrt{\sum_{k=1}^{N}\left(\frac{L_{kd}^{'(k)}}{\sigma_d^{(k)} C_f} f_1^2 + \frac{L_{kq}^{'(k)}}{\sigma_q^{(k)} C_f} f_2^2 + \frac{f_3^2}{L_{ls}^{(k)} C_f}\right) + \frac{1}{L_f C_f}}. \tag{5.26}$$

Since $f_1, f_2 \in [-\frac{2}{3}, \frac{2}{3}], f_3 \in [0, 2]$, the upper bound $\bar{\gamma}$ is achieved when $f_1 = f_2 = \frac{2}{3}$, and $f_3 = 2$.

To verify the effectiveness of the above eigenvalue bounds, a Monte-Carlo test is performed on a multi-machine system that has a total of 100 machines, where the values of angular velocity ω and f_1, f_2, f_3 are given randomly in their range. The corresponding bounds and system eigenvalues in 10,000 tests are demonstrated in Fig. 5.6. As can be seen that all the eigenvalues are located within the rectangular area constrained by the real and imaginary part bounds.

As an extensible modular model, another meaningful thing is to know how eigenvalue bounds will change when adding or removing one module from the

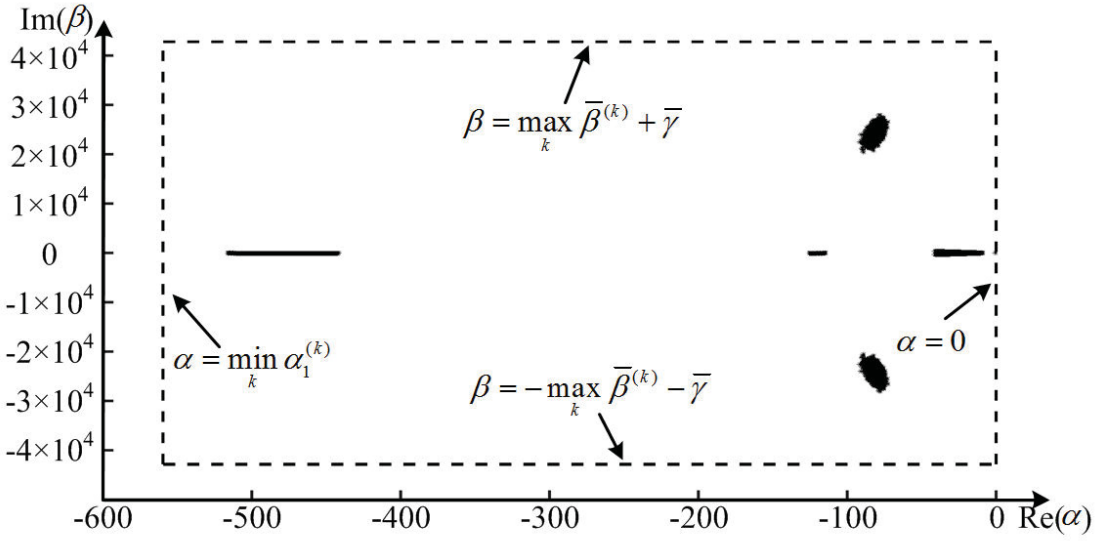

Figure 5.6: Monte-Carlo eigenvalue test results of a 100 machine system.

system. Based on the above analysis, it can be concluded that adding or removing module from the system does not change real part bounds unless the real parts of the added or removed module's eigenvalues exceed the existed real part bound's range. However, it will always affect the imaginary part bounds, not only because $\max_k \bar{\beta}^{(k)}$ may change, but also that $\bar{\gamma}$ is a function of module number N, as shown in (5.26).

It is worth mentioning that although the above analysis are based on the aforementioned assumptions, they are still valid when taking into account the load torque transients as doing so does not affect the fact that $\mathbf{A}_2$ is a bipartite matrix because these modules are linked by a common DC bus.

5.4 Summary

This chapter presented a modular assembly methodology for modeling the on-the-move MEA multi-domain multi-machine system. The featured pneumatic, hydraulic and mechanical parts on MEA are modeled as modules and their mathematical descriptions are given. In addition, this chapter analyzed the eigenvalue bounds of the multi-machine drive system when assembling these modules. It is found that the real part eigenvalue bound of the assembled system does not grow with the module number. It is the maximum range of the real part bound among all these individual modules. However, the imaginary part bound always

increases with the rise of module number. This chapter also gives practical eigenvalue bounds (both real and imaginary part) of the multi-machine drive system, which is useful when employing explicit numerical method to solve the system.

6

Real-Time Simulation Performance and Results of the EZM Based MEA Model

6.1 Introduction

Based on the modeling methodology and mathematic analysis of EZM in the previous chapters, a comprehensive model of MEA that contains all four domain (pneumatic, hydraulic, mechanical and electric) models is constructed. The model is emulated on the Xilinx® Virtex Ultrascale+VCU118-ES1 FPGA board and realized real-time execution in computation. The electric part is constructed based on the structure of Boeing®-787 on-board electric system, as illustrated in Fig. 1.2. The multi-domain models are based on the models explained in chapter 5 (Fig. 5.1, Fig. 5.2, Fig. 5.3). This chapter presents the test scenario configurations and detailed simulation results along with their comparisons with commercial softwares.

6.2 Hardware Configuration of the Real-Time Simulation Platform

The hardware configuration of the real-time MEA emulation system is shown in Fig. 6.1. The transient waveforms are calculated digitally in real-time on Xilinx® Virtex UltraScale+ VCU118-ES1 FPGA Evaluation Platform and exported to oscilloscope through a digital-to-analog converter (DAC) for display. There are multi-

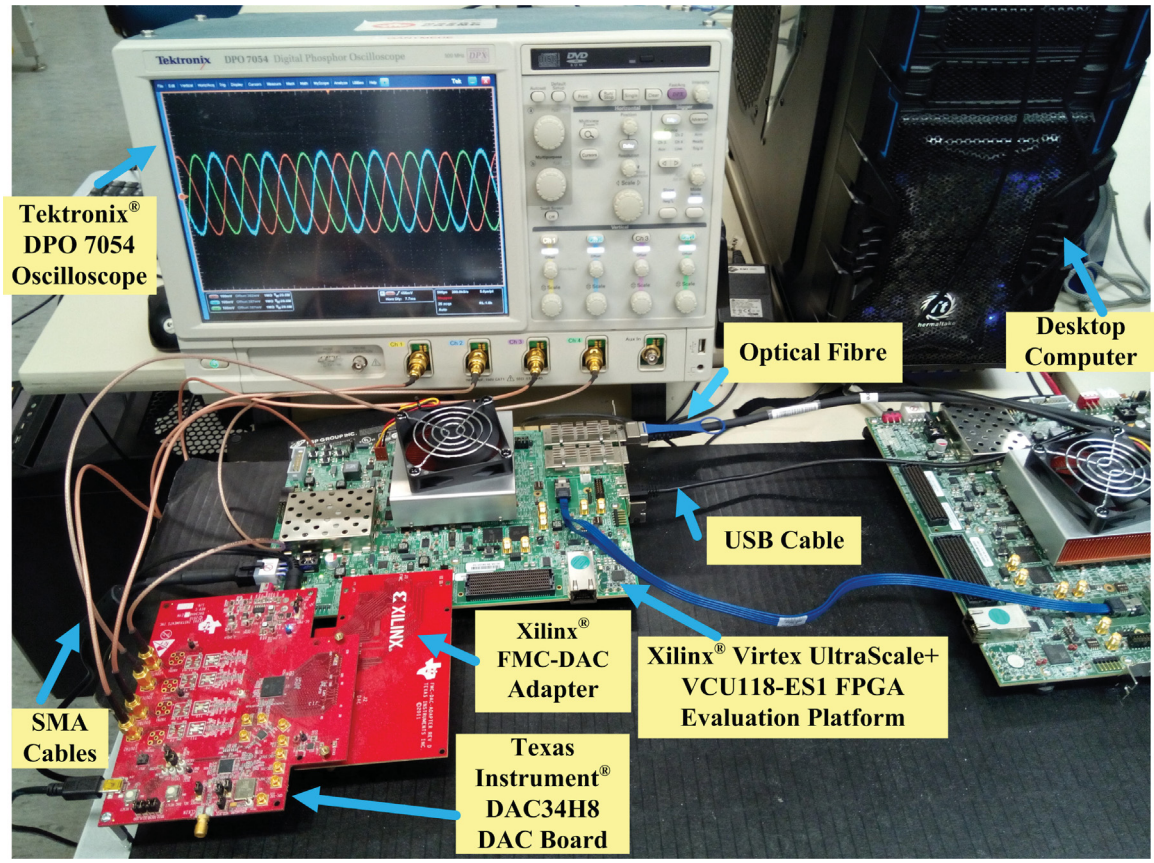

Figure 6.1: Hardware configuration of the real-time MEA emulation system.

ple communication interfaces between the FPGA board and the external computer so that the HIL emulation is available on this test set-up. The microgrid model of MEA with exact the same structure in Fig. 1.2 is built on the FPGA hardware while some controllers can be put on the external computer for performance validation and parameter design because it is very convenient to tune controller parameters on the computer. On the other hand, it is also convenient to modify the structure or component value of the MEA microgrid model. The only effort is to re-synthesize the model and download it to the FPGA board.

6.3 EZM Implementation Descriptions

Real-time application of a large and complicated system like MEA power system is difficult to achieve using conventional modeling methods because of their high computational complexity. However, by utilization of EZM modeling methodology, this task becomes relatively easy because the whole system can be dealt with

in a divide and conquer manner. The MEA microgrid is constructed at component level first where the corresponding characteristics can be found in literature. Then, these components are treated as either voltage or current sources and assembled into a network in hierarchical and zonal fashion. Thereby, the EZM's computation principle can be applied to solve the network state. When combined with FPGA where highly parallel computation is available, the real-time simulation of Boeing®-787 MEA microgrid is realized . The numerical stability analysis presented in the previous chapters assure that by employment of proper numerical discretization method and small time step (the 4-th Runge-Kutta method at 1 us time-step in this study case), the whole simulation model is computational safe and accurate.

The electrical part includes complete subsections (generation, transmission and distribution) of a typical power system and also contains various conversion processes (AC to DC, DC to AC). Fig. 6.2(a) exhibits the structure of MEA on-board power system for EMA to be modeled in this case study. It is constituted by a synchronous generator (SG), a phase-shift transformer, two diode rectifiers, an L-C filter, a three-phase inverter and a permanent-magnet-synchronous-machine (PMSM) for driving the actuator.

Constructing the state variable model of this system is possible but very difficult and time-consuming. However, by utilization of EZM, the modeling process becomes relatively easy. Following the hierarchical and zonal decomposition process of EZM, the whole system can be split into several sub-modules according to their basic functions, as shown in Fig. 6.2(b). Each sub-module behaves like either current or voltage source at the output terminal to interface with other modules. The top-level solver is only responsible for the voltage-current relations between these modules and does not need to consider their internal structures. In other words, any sub-module model that conforms to the output regulation would fit for the top-level solver, from the simplest functional model to the most sophisticated device-level model.

Take the three-phase inverter module as an example, it behaves like a current source when interfacing with the L-C filter and like a three-terminal-two-independent-voltage source when interfacing with the PMSM, while the L-C filter and PMSM feeds it back with their voltage and current values, respectively. The functional model adds two PMSM line currents as the value of output current source and selects 0 or ± 1 times filter voltage as the values of output voltage sources according to the switching signals from the control system. The device-

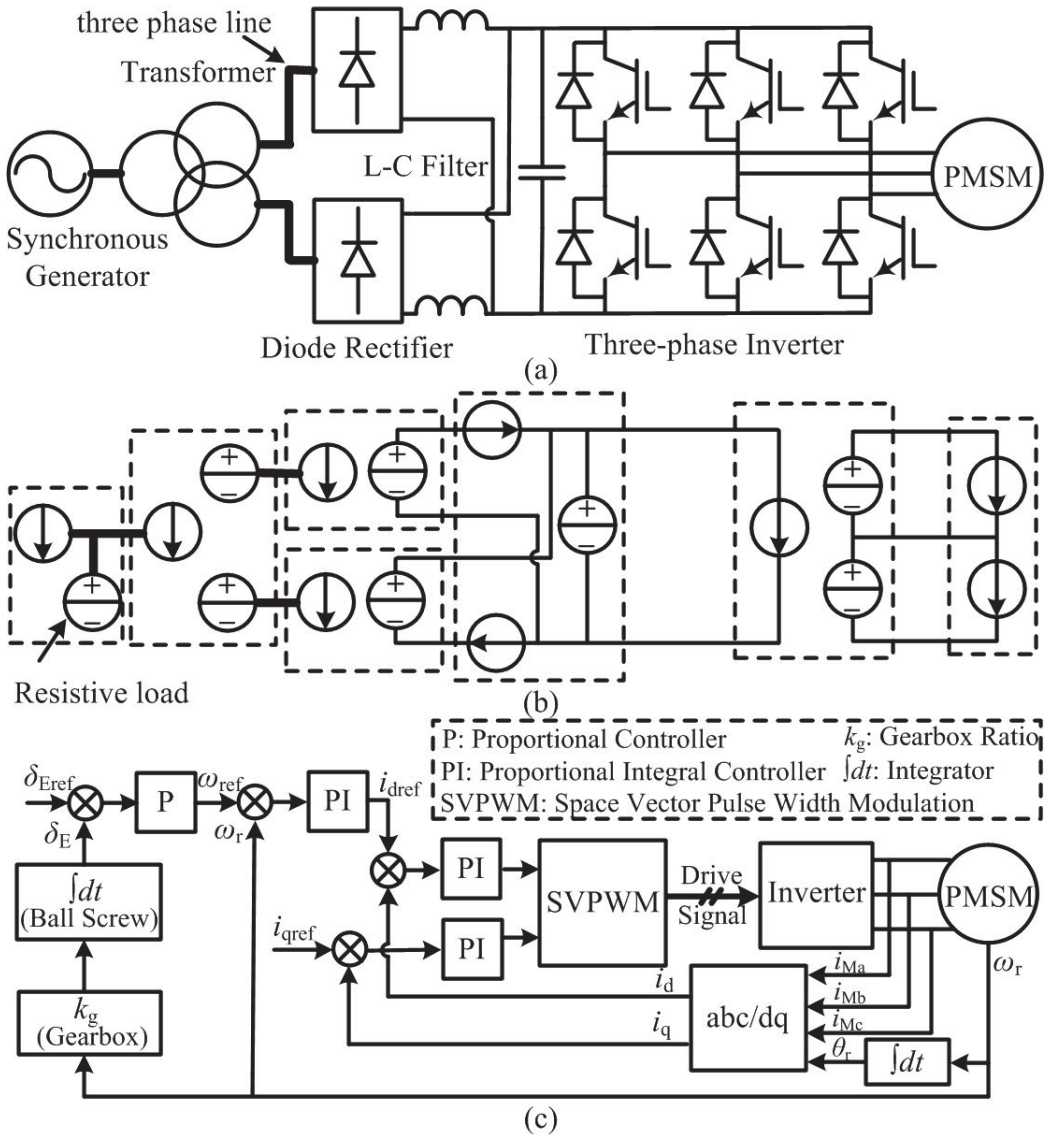

Figure 6.2: MEA on-board power system for EMA. (a) System configuration; (b) The equivalent EZM model; (c) Structure of control system.

level model, however, takes into account the switching transient of the power electronic devices so that the output current and voltage are no longer simple algebraic functions of the input values. This model can be realized by viewing the switches as current source in turn-off transients and steady off-state and as voltage source in turn-on transients and steady on-state.

Detailed mathematic models of the individual subsystems can be found in the following references: SG and PMSM models in [106]; diode rectifier model in [111]; insulated-gate-bipolar-transistor (IGBT) and converter model in [53]. Correspondingly, the implementation details of control scheme can be found in [93].

All the components in the circuit are viewed as either current or voltage sources under EZM's modeling principle. After proper classification and selection, the voltage/current relation of these components can be found using equation (3.14)-(3.22) and the antisymmetry property proved in the previous chapter. When voltage/current relation is found, the simulation process of every individual component is decoupled into two interleaved process: advancing system variable according to component's characteristics and taking into account the reponse of system network. EZM does not have any specific requirement on how the component is modeled. As long as its characteristics can be described by voltage/current equations, it will fit in EZM's modeling process seamlessly. For example, the usual model of motor in [106] is a current (or flux) as state variable, voltage as stimulating source model, thus it will be modeled as current source in EZM and using the network response voltage to update its states. There is no specific restriction on its internal equations.

Another alteration of the EZM model that should be noticed is the resistive load added between the SG and the transformer. It is a common configuration that can be found in many models developed by various simulation softwares. Some softwares provide the explanation: for example, Matlab/Simulink® explains it in this way: electrical machines cannot be connected to an inductive network unless a parasitic resistive or capacitive element is connected at machine terminals to avoid numerical oscillations [112]. However, this can be explained in another way from the point view of EZM modeling. It is known that inductive branches should be viewed as current sources under the EZM modeling principle, which is true for both SG and transformer windings. However, current source branches should not be connected in series to avoid circuit contention. The simplest way to resolve this contention is to add a branch between them that can be treated as voltage source, which is exactly what the resistive load is used for (approximate 5% of the machine nominal power is sufficient).

The MEA on board multi-domain multi-machine model is developed and implemented on Xilinx® Virtex xcvu9p FPGA core for real-time emulation. The system contains 100 machine drive modules and each has five state variables. These sub-modules can be configured to interface pneumatic, hydraulic or mechanical loads. Since the whole system is expressed in state-space form and the eigenvalue bounds are identified, it is convenient to solve it numerically. This thesis adopts the classical 4th order Runge-Kutta (RK4) method working at 1 μs time-step as the numerical solver. Because of the explicit nature of RK4, the computation can be

conducted in fully parallel manner. That is, the update of every state variable is solely based on history state information, thus can be completed synchronously and independently [82], a mechanism that is highly suitable for parallel hardware emulation on FPGA.

The FPGA implementation is accomplished using VHDL language in Vivado® software. The hardware resource utilization for a 100 machine multi-domain multi-machine system is summarized in Table 6.1.

Table 6.1: Hardware utilization of the multi-domain multi-machine model

Resource	LUT	FF	BRAM	DSP
Utilization	1021656 (86.42%)	433812 (18.34%)	92.5 (4.29%)	6286 (91.95%)

6.4 Real-Time Simulation Validation Results

Several test scenarios are carried out to validate the fidelity of the constructed EZM based MEA model in this section. The reference results are obtained from commercial simulation softwares. In specific, when the model is a circuit network, it will be solved by PSCAD/EMTDC®; when the model is a state variable model, it will be solved by Matlab/Simulink® and the switching transients are provided by SaberRD®. Obviously, the multi-domain model can not execute in real-time using these softwares. Not only because of the computation efficiency, but also that they can not communicate with each other smoothly while they are working. Therefore, PSCAD/EMTDC® runs first and the results are stored in a file. Matlab/Simulink® then reads this file as an input and gives the state variable results.

6.4.1 Normal Operation Test Scenarios

Two test scenarios under normal working operation are presented in this subsection.

6.4.1.1 Abrupt Load Change of WIPS

WIPS load is one of the major loads in the 230 V AC bus. The WIPS is not always working under full load and when there is an abrupt load change, it will have

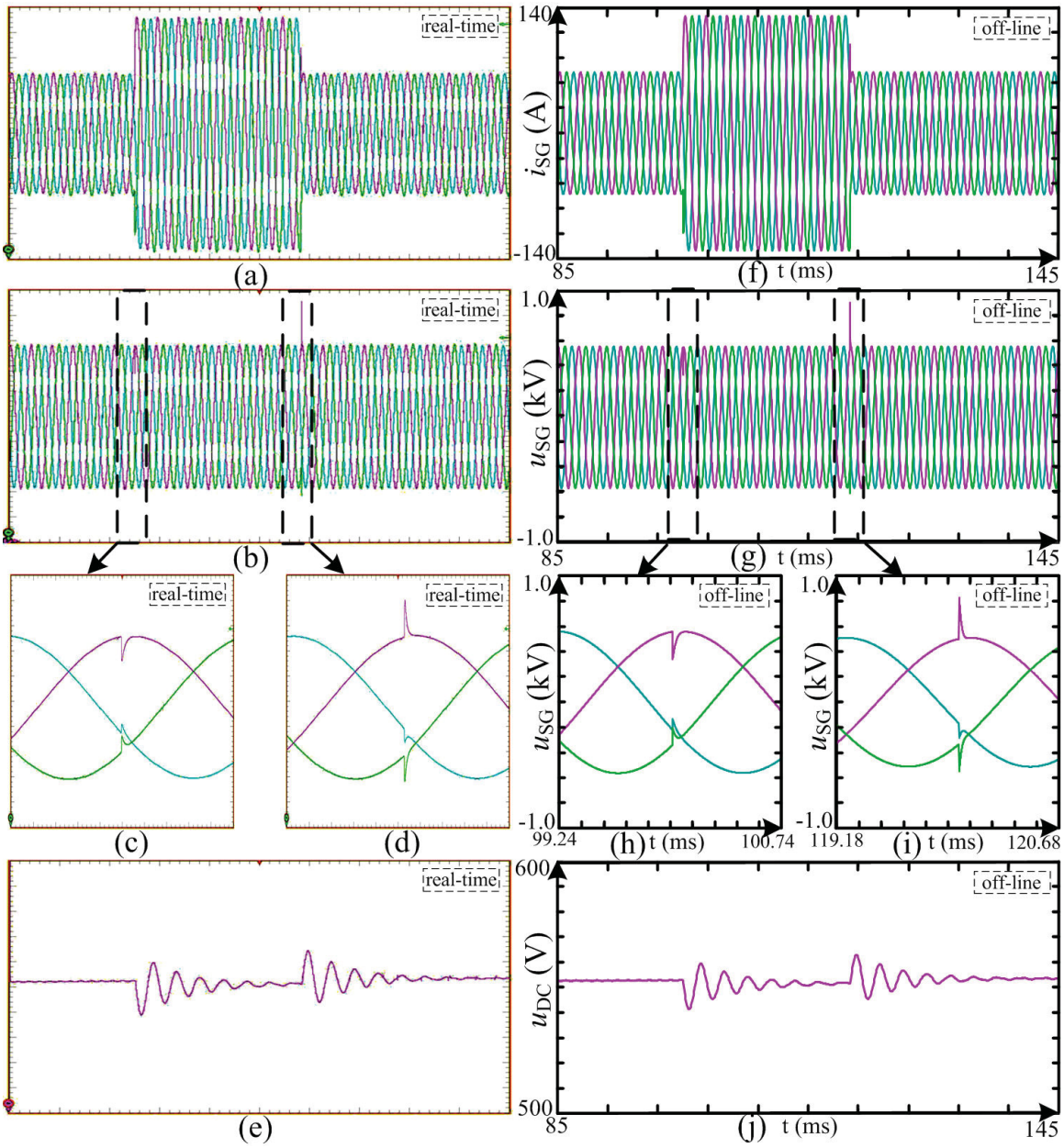

Figure 6.3: Transient waveforms under WIPS abrupt load change. (a) Generator line currents i_{SG} from EZM, y-axis: 28 A/div, x-axis: 6 ms/div. (b) Generator line-line voltages u_{SG} from EZM, y-axis: 200 V/div, x-axis: 6 ms/div. (c)-(d) Magnified waveforms of (b), y-axis: 200 V/div, x-axis: 150 μs/div. (e) DC bus voltage u_{DC} from EZM. y-axis: 10 V/div, y-offset: 550 V, x-axis: 6 ms/div. (f)-(j) Counterparts of (a)-(e) from PSCAD/EMTDC® with the same axis scale.

significant influence on AC and DC bus. Fig. 6.3 presents the transient waveforms when the AC bus1 load changes from 33.12 kW to 63.96 kW at t=0.1 s and changes back at t=0.12 s because of WIPS load fluctuation. Both the AC and DC bus have sensed the load change and voltage transients are induced.

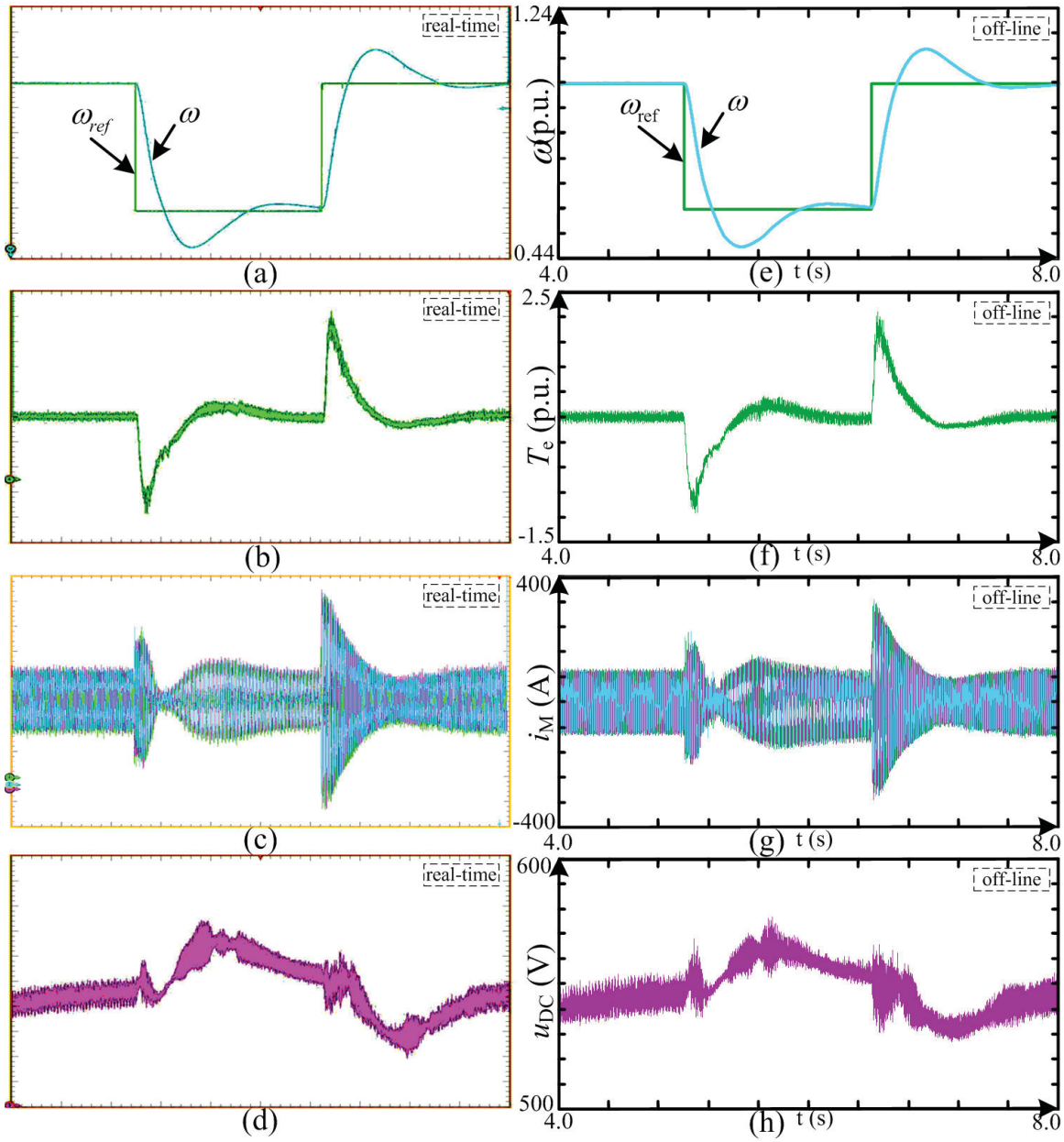

Figure 6.4: Transient waveforms of PMSM speed regulation. (a) Speed command ω_{ref} and motor speed ω from EZM, y-axis: 0.08 p.u./div, y-offset: 0.84 p.u., x-axis: 400 ms/div. (b) Motor torque T_{e} from EZM, y-axis: 0.4 p.u./div, y-offset: 0.5 p.u., x-axis: 400 ms/div. (c) Motor currents i_{M} from EZM, y-axis: 80 A/div, x-axis: 400 ms/div. (d) DC bus voltage u_{DC} from EZM. y-axis: 10 V/div, y-offset: 550 V, x-axis: 400 ms/div. (e)-(h) Counterparts of (a)-(d) from PSCAD/EMTDC® with the same axis scale.

6.4.1.2 PMSM Speed Regulation Transients

PMSM is utilized mainly for environment control, which helps to keep the temperature and air pressure in the aircraft cabin within reasonable range. For a better

control precision and fuel saving purpose, closed-loop speed regulation of PMSM is necessary. Fig. 6.4 presents the waveforms when the speed command ω_{ref} of PMSM jumps from 1.0 p.u. to 0.6 p.u. at t=5.0 s and increases back to 1.0 p.u. at t=6.5 s (the load torque applied to PMSM is 0.5 p.u.). It can be noticed that the speed, torque as well as motor currents have experienced obvious transients and stabilized in about 1.5 s. The DC bus voltage is also affected by the motor transients but within reasonable range. Because of the power electronic DC/AC converter, the DC bus voltage have abundant high-frequency components. The results from EZM and PSCAD/EMTDC® have very high consistency.

6.4.2 Fault Operation Test Scenarios

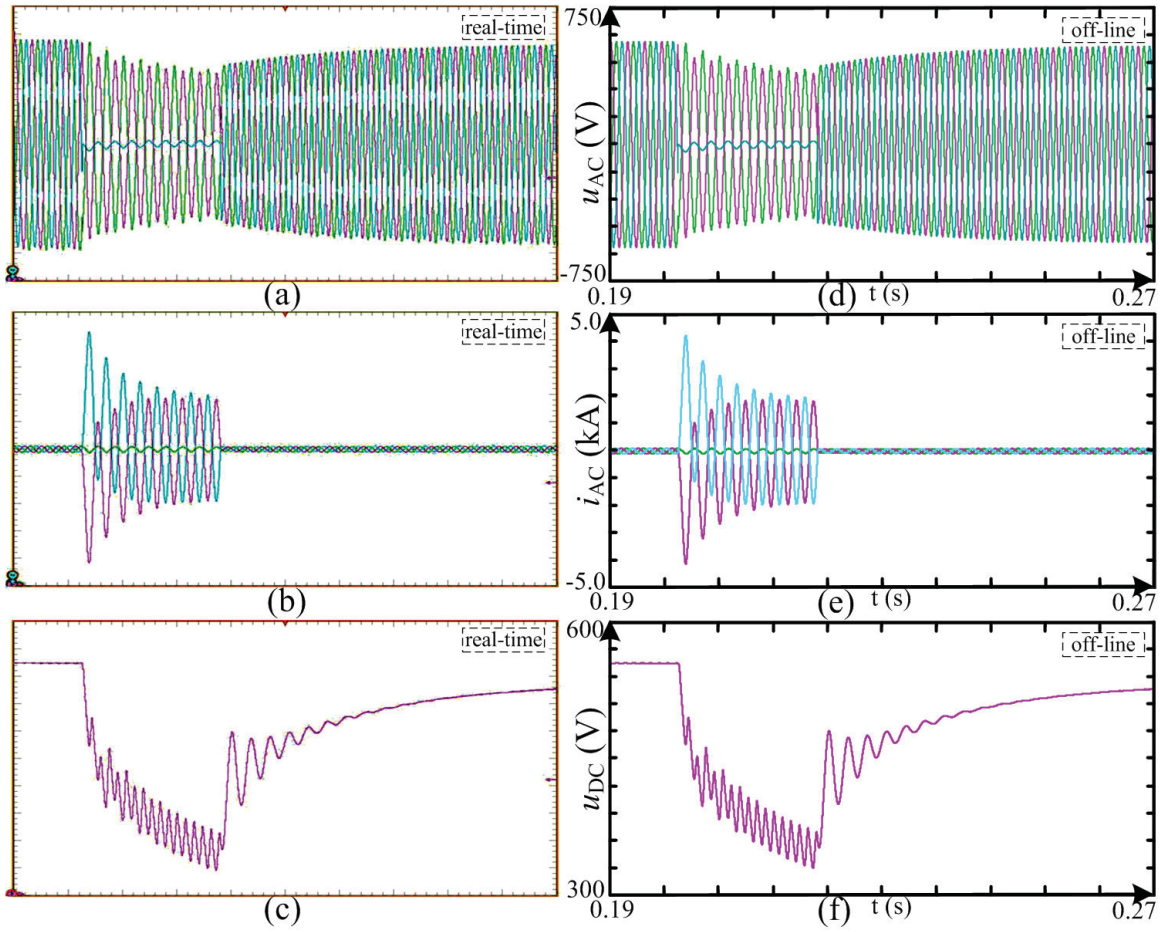

Figure 6.5: Transient waveforms of AC bus line-line fault. (a) AC bus line-line voltages u_{AC} from EZM, y-axis: 150 V/div, x-axis: 8 ms/div. (b) AC bus line currents i_{AC} from EZM, y-axis: 1000 A/div, x-axis: 8 ms/div. (c) DC bus voltage u_{DC} from EZM. y-axis: 30 V/div, y-offset: 450 V, x-axis: 8 ms/div. (d)-(f) Counterparts of (a)-(c) from PSCAD/EMTDC® with the same axis scale.

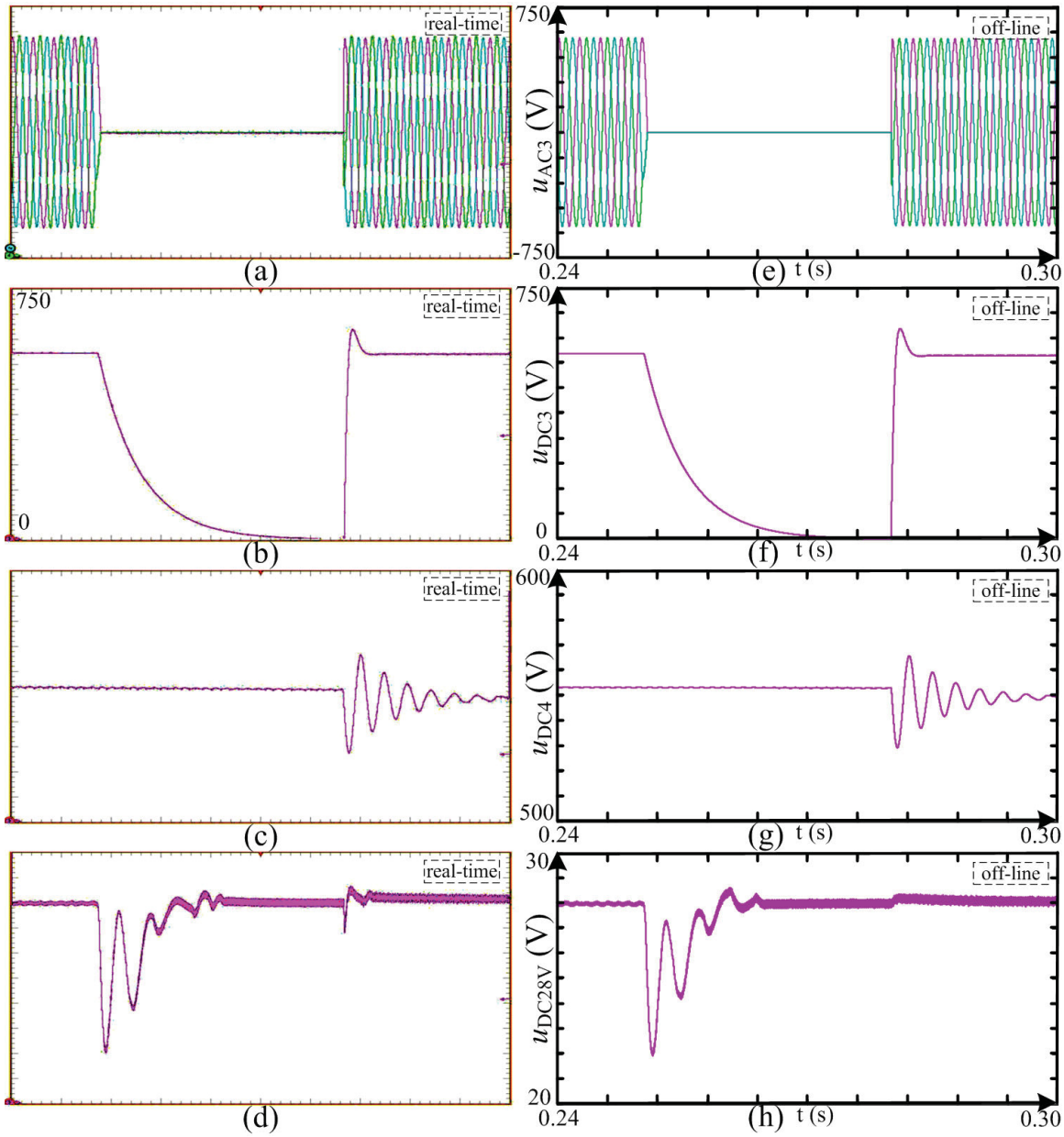

Figure 6.6: Transient waveforms of SG loss fault. (a) AC bus 3 line-line voltages u_{AC3} from EZM, y-axis: 150 V/div, x-axis: 6 ms/div. (b) DC bus 3 voltage u_{DC3} from EZM, y-axis: 75 V/div, y-offset: 375 V, x-axis: 6 ms/div. (c) DC bus 4 voltage u_{DC4} from EZM, y-axis: 10 V/div, y-offset: 550 V, x-axis: 6 ms/div. (d) DC 28 V bus voltage u_{DC28V} from EZM, y-axis: 1 V/div, y-offset: 25 V, x-axis: 6 ms/div. (e)-(f) Counterparts of (a)-(d) from PSCAD/EMTDC® with the same axis scale.

The safety of aircraft can not be overemphasized in the aviation industry. This requires the MEA microgrid to have very high reliability. It should have the ability to get through or recover from fault condition. Two test scenarios under fault conditions are presented in this subsection.

6.4.2.1 Line-line Fault of AC Bus

AC bus is crucial to the aircraft power system as it is the link that connects the power sources and loads. Fig. 6.5 presents the transient waveforms of AC bus voltages and currents as well as DC bus voltage when there is a phase A-B line-line fault at t=0.2 s and cleared at t=0.22 s. The AC system comes to asymmetry operating condition and the DC bus voltage drops during fault. When the fault is cleared, the AC system comes back to normal mode and DC bus voltage also recovers. This demonstrates that the MEA power system has the ability to get through fault.

6.4.2.2 Loss of SG

The four load zones work independently under normal condition because of variable frequency of individual AC bus (320-800 Hz). However, when one generator encounters a failure and is disconnected from the AC bus, the power management center should transfer the corresponding load to another AC bus. Fig. 6.6 presents the transient waveforms when SG3 is disconnected from AC bus 3 at t=0.25 s and the power management center transfers load zone 3 to AC bus 4 at t=0.28 s. As can be seen that DC bus 3 voltage drops to zero during failure but backs to normal value after AC voltages recover. In the meantime, DC bus 4 voltage is also affected by the load transfer but stabilized shortly. As comparison, the DC 28 V bus is essential to the avionics and is equipped with energy storage compensation DC/DC converter. When faced with the same AC power source loss condition, the DC 28 V bus voltage does not drop to zero and recovers very quickly because of the compensating energy from battery.

The above simulation waveforms can be used to check the validity of MEA microgrid. This real-time simulation model is suitable for hardware-in-the-loop testing to make sure all the transients meet some specific industrial or military standards like MIL-STD-704F.

6.4.3 Multi-Domain Multi-Machine System Test Scenarios

In the following case-study, a 100-minute flight is simulated in real-time, where the pneumatic, hydraulic and mechanical aspect characteristics from E-ECS, EHSA and EMA along with their corresponding electric performance waveforms are exhibited. Its validity is also corroborated by an off-line simulation of the same system performed on Matlab/Simulink®.

6.4.3.1 Electric & Pneumatic Characteristics from E-ECS

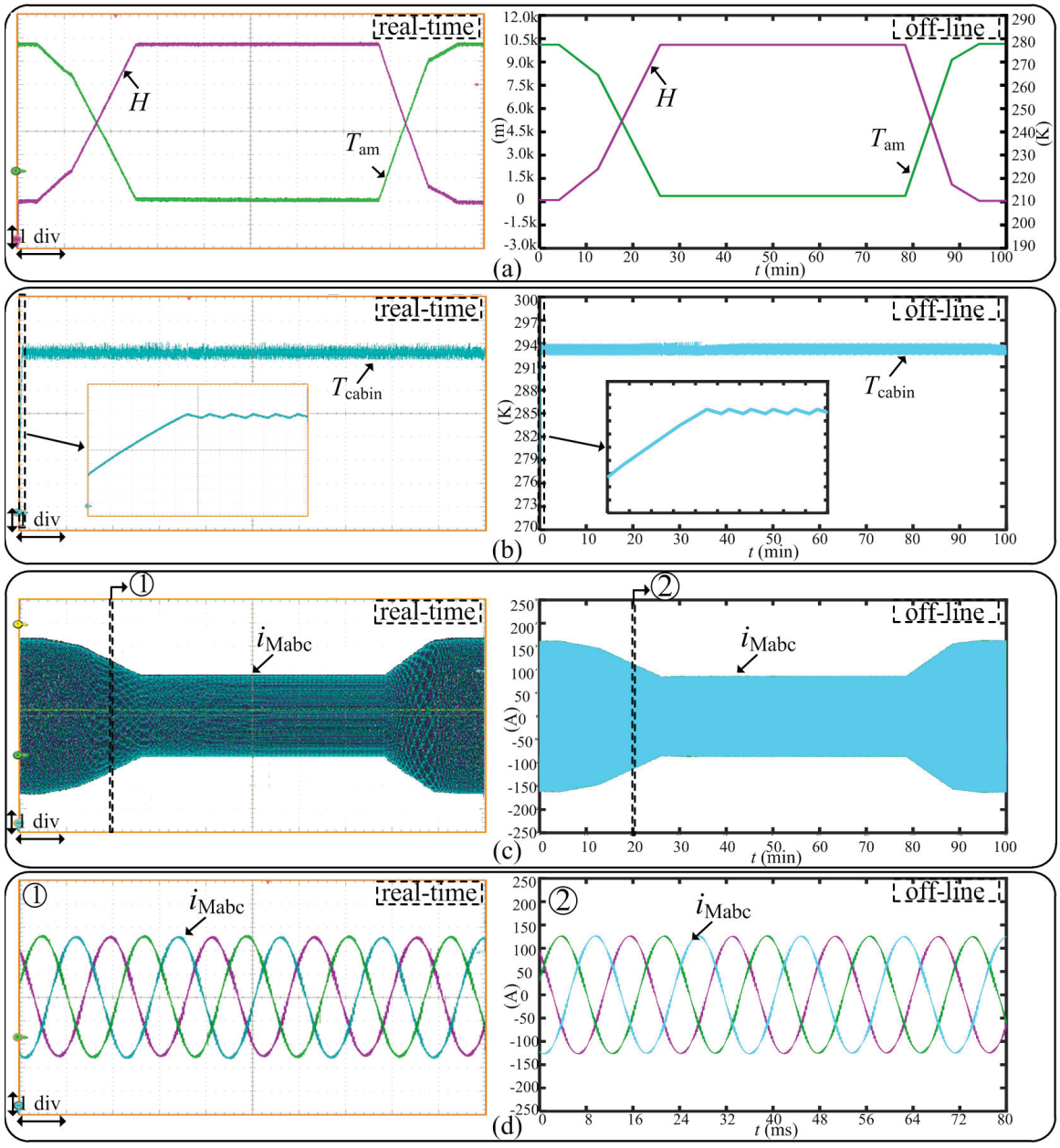

Figure 6.7: Electric & Pneumatic characteristics waveforms from E-ECS. (a) Aircraft altitude H: 1.5 km/div; atmosphere temperature T_{am}: 10 K/div; time-scale: 10 min/div. (b) Aircraft cabin temperature T_{cabin}: 3 K/div; time-scale: 10 min/div. (c) Three-phase machine currents i_{Mabc}: 50 A/div. time-scale: 10 min/div. (d) Magnified machine currents in the window shown in (c): i_{Mabc}: 50 A/div; time-scale: 8 ms/div.

Fig. 6.7 shows the performance waveforms from the E-ECS during the 100-minute flight. As can be seen that, the cabin temperature remains almost constant (20 °C) once the E-ECS starts working. However, the atmosphere temperature

changes with the flight mission (altitude) profile. As a result, the three-phase machine currents also changes. It is believed that the lower atmosphere temperature will reduce the pneumatic power required by the ECS because the cabin generally needs cooling rather than heating most of the flight time [113], which also coincides with the emulation outputs. To make a clear illustration, a short period of three-phase machine currents are also exhibited in Fig. 6.7.

6.4.3.2 Electric & Hydraulic Characteristics from EHSA

Fig. 6.8 shows the response waveforms from EHSA when there is a step command on machine velocity from 0 to 3600 rpm at t=0.5 s and back to 0 at t=1.5 s. Machine currents are stimulated during this period to generate electric torque so as to push the hydraulic cylinder piston. Also, it can be observed that there is an obvious overshoot in the differential pressure and actuator speed when the system is initially started, which is a commonly witnessed feature in hydraulic system to overcome the static friction of the actuator rod [10]. The detailed transients of the overshoot are displayed in Fig. 6.8(d) and (h) to demonstrate the model's high fidelity.

6.4.3.3 Electric & Mechanical Characteristics from EMA

Fig. 6.9 exhibits the step response of the EMA system, during which the command value of elevator position δ_{Eref} jumps from 0 to 1.0 p.u. at t=0.1 s and from 1.0 to -1.0 p.u. at t=3.0 s. The responding elevator position δ_{E} and resulting mechanical response of angle of attack α are illustrated in Fig. 6.9(a). The corresponding detailed machine performance curves (three-phase currents i_{Mabc}, rotor speed ω and torque T_{e}) are shown in Fig. 6.9(b)$\sim$(c). As an important feature of EMA system, Fig. 6.9(d)$\sim$(e) also depict i_{Mabc} waveforms during start-up process. The actuator is initially held in position by the electric brake, and the motor must be powered before the brake is released to prevent runaway [114]. Thus, there is a period of time the machine keeps stand-still and nearly full DC currents are induced so that high torque can be generated. Once the brake is released and the machine begin to rotate, the three-phase currents become sinusoidal. Fig. 6.9(f)$\sim$(g) exhibit the switching transients of power electronic devices as detailed device-level converter models are incorporated in the electrical part system. The target switching device employed in the model is Infineon FZ400R12KE4 IGBT. Turn-on and turn-off transients of IGBT are displayed and the characteristic values $t_{\mathrm{d(on)}}$, t_{r}, $t_{\mathrm{d(off)}}$, t_{f} are very close to those given in the data-sheet. It has to mention that the efficiency

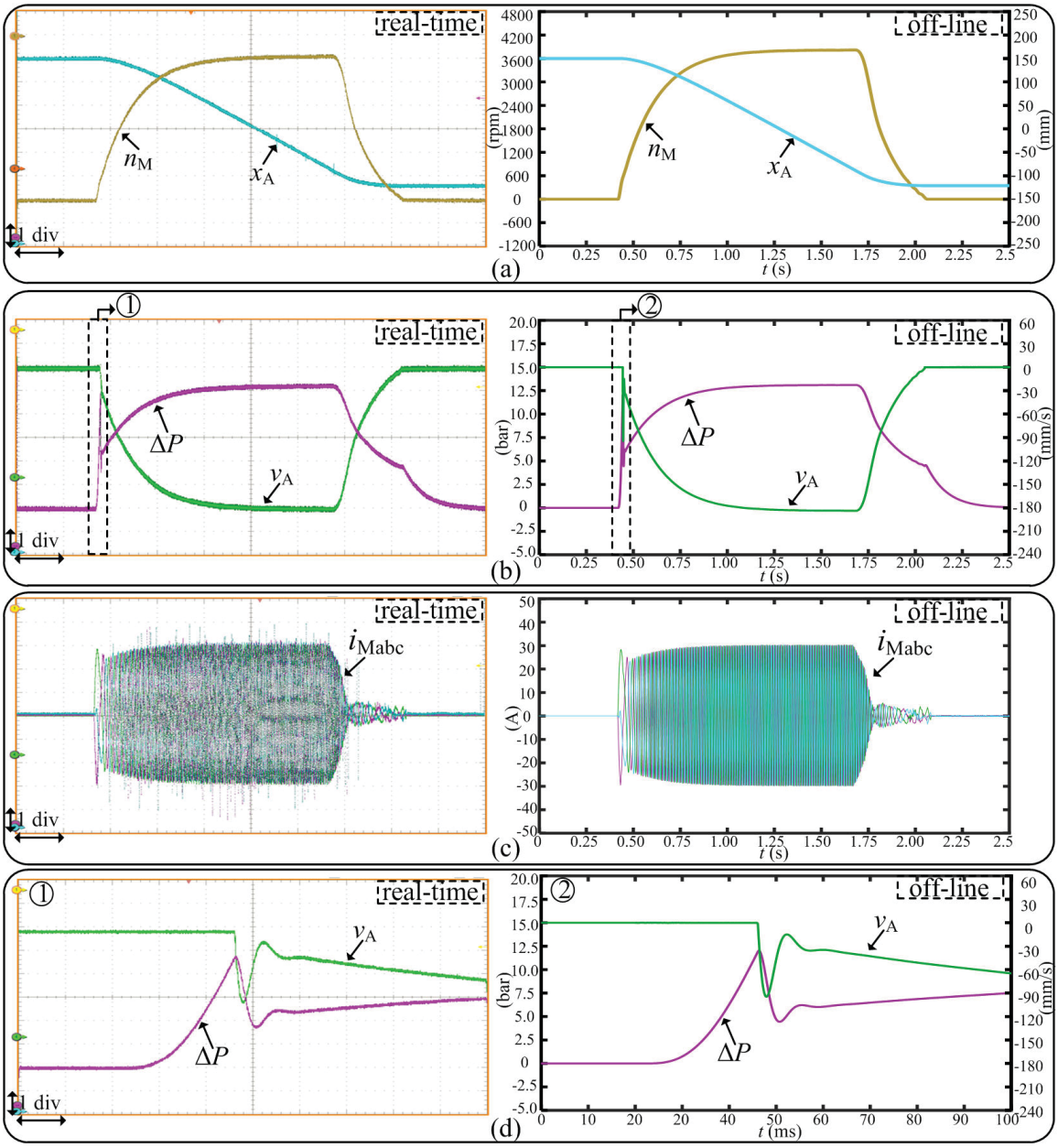

Figure 6.8: Electric & Hydraulic characteristics waveforms from EHSA. (a) Machine rotating speed n_M: 600 rpm/div; actuator position x_A: 50 mm/div; time-scale: 0.25 s/div. (b) Cylinder differential pressure ΔP: 2.5 bar/div; actuator speed x_A: 30 mm/s/div; time-scale: 0.25 s/div. (c) Three-phase machine currents i_{Mabc}: 10 A/div; time-scale: 0.25 s/div. (d) Magnified ΔP (2.5 bar/div) and x_A (30 mm/s/div) in the window shown in (b); time-scale: 10 ms/div.

performance of the FPGA model and commercial software model vary greatly. To accomplish the same task in Fig. 6.9, PSCAD/EMTDC® consumes 355.9 s, almost 60 times slower than the FPGA model, which only uses 6.0 s in real-time execution.

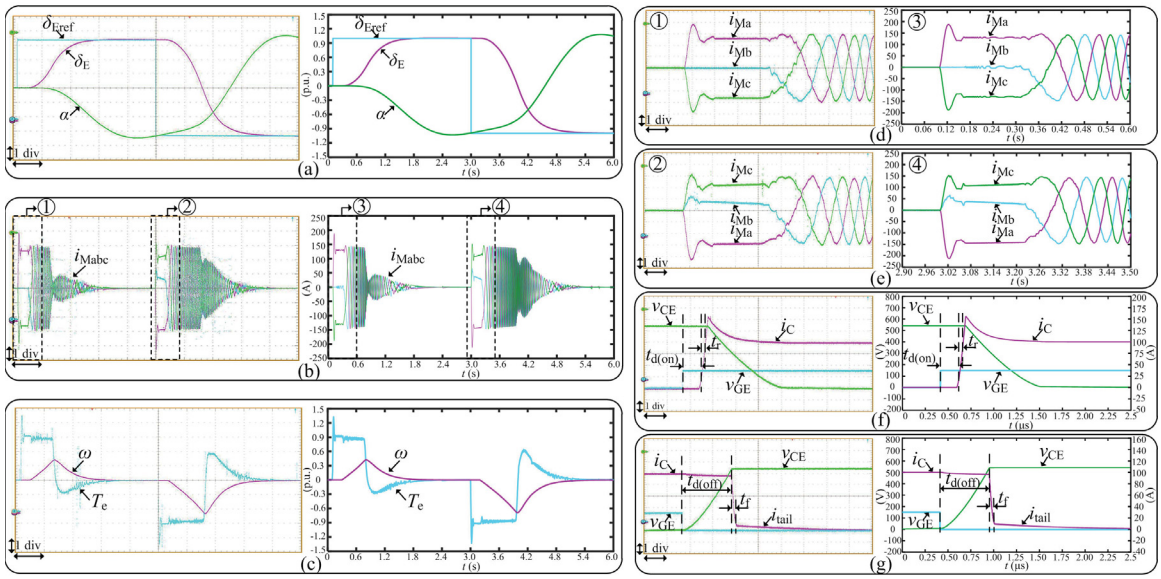

Figure 6.9: Step response of the EMA system (left: EZM model; right: commercial software models). (a) Command of elevator position δ_{Eref}, responding elevator position δ_{E} and angle of attack α, y-axis: 0.3 p.u./div, x-axis: 0.6 s/div. (b) Machine three-phase currents i_{Mabc}, y-axis: 50 A/div, x-axis: 0.6 s/div. (c) Machine rotor speed ω and torque T_{e}, y-axis: 0.3 p.u./div, x-axis: 0.6 s/div. (d)∼(e) Machine start-up currents i_{Mabc}, y-axis: 50 A/div, x-axis: 0.06 s/div. (f)∼(g) Switching transients of power electronic devices, y-axis: 100 V/div for voltage, 25 A/div for current, x-axis: 0.25 μs/div.

6.4.3.4 Electric & Thermal Characteristics from EMA

Fig. 6.10 illustrates the performance waveforms of EMA system under thermal test. The command signal δ_{Eref} given to the system is a 0.1 Hz triangle signal whose upper and lower peak are 1.0 and -1.0 p.u. respectively, which means the elevator is excited to swing back and forth to its maximum displacement position repeatedly. The ambient and cooling liquid temperatures are assumed to be 25 °C. The thermal test is conducted in four stages: (1) from 0∼60 min, the load torque applied to the machine is 0.5 p.u.; (2) from 60∼120 min, load torque increases to 0.9 p.u.; (3) from 120∼180 min, the system is in the rest and (4) from 180∼300 min, the load torque becomes 0.7 p.u.. Fig. 6.10(a) depicts the machine currents during the four stages and Fig. 6.10(b)∼(c) are the corresponding dynamic temperature of stator winding ϑ_{SW} and permanent magnet ϑ_{PM}, respectively. Snapshot of machine test currents in one period in stage (1), (2) and (4) are also given in Fig. 6.10(d)∼(f). As can be seen that the larger the load torque is, the higher the temperature will be. The most serious situation occurs in stage (2) during which ϑ_{SW} becomes nearly 90 °C and ϑ_{PM} even climbs to over 100 °C. Special attention should be paid to avoid

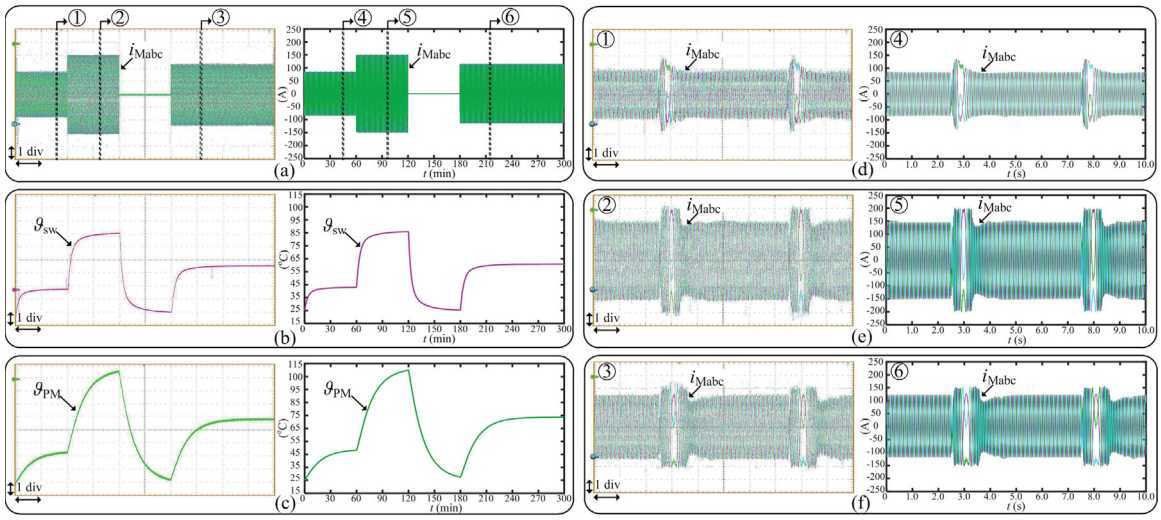

Figure 6.10: Thermal test waveforms (left: EZM model; right: commercial software models). (a) Machine three-phase currents i_{Mabc}, y-axis: 50 A/div, x-axis: 30 min/div. (b) Stator winding temperature ϑ_{SW}, y-axis: 10 °C/div, x-axis: 30 min/div. (c) Permanent magnet temperature ϑ_{PM}, y-axis: 10 °C/div, x-axis: 30 min/div. (d)∼(f) Snapshot of machine test currents, y-axis: 50 A/div, x-axis: 1.0 s/div.

winding failure or demagnetization. Thus the system is put in rest in stage (3) to let the machine components cool down. The temperature finally stabilize in stage (4) with a safe margin from failure.

The above three test scenarios demonstrate that the real-time hardware model emulated on FPGA has the ability to accommodate multi-domain characteristics while in a multi-machine environment. The results match the off-line simulation results very well and could be a useful tool for hardware-in-the-loop test and design of MEA power system.

6.5 Summary

This chapter presented simulation results of the real-time EZM based comprehensive MEA model. Electric, pneumatic, hydraulic, mechanical and thermal parts of the MEA system are modeled and simulated in real-time on FPGA board using EZM. The results are compared with commercial software outputs and very high consistency are achieved under several test scenarios, which demonstrate that EZM is able to accommodate different domain models very well. The constructed MEA model could be a good HIL test-bench for MEA design and research.

7
Conclusions and Future Work

More electric aircraft is a complex system that needs efforts from many engineers and researchers. It is also a huge project that involves many advanced technologies. Comprehensive modeling and real-time simulation of MEA is helpful for the on-going development of the involved technology. This task requires many aspects of the MEA characteristics to be incorporated and modeled properly. During the constructing process of a comprehensive MEA model, many modeling methods are considered. However, they either suffer from computational inefficiency problem or inconvenient modeling procedures for real-time simulation. Those inconvenience inspired the work in this thesis. A comprehensive model of MEA with some advanced features is desirable for both industrial engineers and academic researchers. This model should be easy to construct and fast in computation. If possible, it should be able to accommodate the existed MEA part models to save modeling effort.

The original idea comes from the attempt to model nonlinearities in power electronic circuit using the conventional Norton analysis method. In this method's modeling mechanism, every component in the circuit is transformed into an equivalent resistor in parallel with a companion current source. This method then use the node voltages as the unknown variables to construct equations based on Kirchhoff's Current Law (KCL). By solving these equations, the node voltages along with branch currents can be found. However, when applying this mechanism into modeling the nonlinearities, there is no rule to determine how large the equiva-

lent resistor should be. By trying different choices for the equivalent resistors, it is found that when their values are set to be 1, the voltage/current matrix equation used to solve the companion current sources for nonlinearities becomes a diagonal time-varying matrix equation and this property can be leveraged to expedite the solving process.

On further investigation of the above idea, it was found that much effort in solving the nonlinearities' companion current sources is redundant because the voltage/current values of the nonlinearities are already known (predicted). Solving these companion current sources is simply trying to make the solution of the node voltage equations in Norton analysis method coincide with the known values. Since the eventual goal of circuit simulation is to find the voltage/current value of every branch, there is no need to take extra effort to make them fit for the Norton analysis form. Therefore, it is the voltage/current relation in the circuit that matters for the simulation computation since every branch in the circuit is either a voltage or current source. They can not be both voltage and current source, otherwise they might violate KCL or Kirchhoff's Voltage Law (KVL).

Later study on this idea uncovered that the branch voltage/current relation in the circuit can be described by an antisymmetric matrix and it is the reason why the voltage/current matrix equation used to solve the companion current sources is diagonal time-varying matrix when all the equivalent resistors' value are 1. More importantly, this idea can be used to prove the antisymmetric property of branch voltage/current in the circuit.

Based on the aforementioned antisymmetric voltage/current relation, a new circuit simulation method was conceived that all the branches in the circuit are viewed as either voltage or current sources and the simulation computation is divided into two interleaved processes: advancing system variables according to components' characteristics and taking into account the network response. That's the basic modeling rule of EZM.

A common question that may arise is that how does EZM manage to decouple the computation of every branch? By studying the relation of EZM and state-space method, it is found that these two modeling methods are equivalent in mathematic description of circuit in continuous domain and they can be mutually transformed. The difference lies on the implementation of integration method in discrete domain. The EZM model always use history information for numerical update of system variables so that each system variable does not rely on each other in computation. That's the property of explicit numerical integration method and it is this

property makes it very suitable for parallel computation. The state-space model, on the other hand, can be integrated using either explicit or implicit method. If explicit method is used, then it is also suitable for parallel computation. If implicit method is used, then system variables rely on each other in computation. Some sequential or iterative algorithms have to be utilized and parallel computation is hard to achieve.

Although explicit integration methods are perfect fit for parallel computation, they usually have relative small numerical stability regions in complex plain. It is required that all the eigenvalues of the system times time-step locate within the stability region before the explicit method is used. The key of successful implementation of EZM then becomes identifying the maximum value of the eigenvalues. That's the reason why this thesis makes much effort analyzing the upper bounds of eigenvalues of the MEA power system.

The process of identifying the maximum eigenvalues of a general circuit is in no way easy, especially for complex systems like the MEA power system. Even though there are some mathematic theorems available that could help, many of these theorems are valid only when all the eigenvalues are real, like the Laguerre-Samuelson's inequality. The exploring process of eigenvalue distribution for a matrix that has complex eigenvalues is generally deemed difficult in mathematics. This thesis has done some preliminary works along this research path. For example, the eigenvalue distribution of a modular assembly system connected by a common bus is analyzed and some interesting conclusions are found. However, more works following this analysis path are required to make it more complete. The following sections summarize the main conclusions and possible directions for future works.

7.1 Conclusions of the Thesis

The main conclusions of this thesis can be summarized as follows:

- A new approach for modeling generalized nonlinearities in power electronics circuit simulation is presented. This approach complies with the modeling rule of Norton analysis method so it is convenient to be incorporated into the existed simulation softwares. The nonlinearities are represented by an equivalent resistor in parallel with a companion current source and the resistor value is set to be 1. The matrix equation used to solve the companion

current sources is formed and it is found that the matrix has time-varying part only on its diagonal.

- Three methods that can be used to solve the diagonal time-varying matrix equation are proposed: precomputed inversion or factorization; modified Gaussian elimination; updating inverse using the Sherman-Morrison formula. These three methods can be applied to solve small, medium and large size problems according to their strengths and features. Two test cases on MMC and NPC circuit shows that this nonlinearity modeling approach is able to yield almost the same results as with commercial softwares while be more than ten times faster in computation time on the same hardware.

- A circuit lemma indicating the voltage/current relation of a general circuit is presented in this thesis. It turns out that the voltage and current relations are related by antisymmetric property of the corresponding relation matrix when the circuit components are properly classified as voltage or current sources. This circuit lemma can be proved mathematically by applying the same nonlinearity modeling idea aforementioned to all the components in the circuit.

- To avoid singularity of the voltage relation in the antisymmetric matrix, the branches that are selected as voltage source should form a spanning tree of the circuit topology.

- Utilizing the antisymmetric property of voltage/current relation, the computation of system variables can be divided into two interleaved processes: advancing system variables according to components' characteristics and taking into account the network response. In this way, the processing of circuit topology and components' characteristics are decoupled and that is the core of EZM modeling methodology.

- The state-space method and EZM are two different ways to model circuit. The state-space method uses differential equations to describe circuit while EZM uses both differential and algebra equations to describe circuit. The state-space model can be obtained from EZM model by annihilating algebra equations in DAEs.

- The utilization of EZM implies the implementation of explicit method for numerical integration. This property makes EZM very suitable for parallel computation because the update of all system variables can be conducted

separately and concurrently. Due to the relatively small stability region of explicit method, the simulation time-step for EZM should always be selected to make all eigenvalues of the system times that time-step locate within the stability region of the employed explicit method.

- The eigenvalues of high-frequency-low-loss circuit are all pure imaginary and their upper bound can be identified by the Laguerre-Samuelson's inequality.

- The degenerate circuit can be transformed into non-degenerate circuit by proper manipulation of circuit structure using the antisymmetric property of voltage/current relation in the circuit.

- The eigenvalues of multi-machine drive system linked by a common DC bus is analyzed. It is found that the upper bound of real part is the same with upper bound of real part among all individual modules. It generally does not grow with the number of modules. However, the upper bound of imaginary part is function of module number. The more modules connected in the system, the larger the imaginary part upper bound will be, which creates more stringent requirement for time-step selection.

7.2 Directions for Future Work

The following topics could be possible directions for future work:

- With the evolving process of power electronic and power system technology, the MEA power system will become more and more complex. More modules and functions on aircraft will be powered by electric energy. It is required that these new modules and functions can be properly modeled, thus new mathematic models should be developed and validated.

- Eigenvalue identification is extremely important for EZM as it is an inevitable process in application of EZM. In most cases, both the real part and imaginary part should be identified because electric system usually has oscillating phenomenon in it. New mathematic theories need to be investigated and applied to analyze the eigenvalue distribution.

- System parameter uncertainty is a common problem in engineering practice. It may arise from inaccurate measurement, changes of working condition

or inadequate modeling precision, etc. How eigenvalue will change with variations of system parameters is worth further studying.

- The numerical stability regions of classic explicit methods are usually relative small in the complex plain. Efforts can be made to design new explicit numerical integration method with larger stability region. In order to attain high computational efficiency, the method should contain as less sub-stages as possible and it is preferable that these sub-stages can run completely or partially in parallel.

- It is known that the MEA on-board power system contains fast transient parts (like the power electronic switching transient) and inertial parts (like the thermal system), thus the multi-rate schemes could be applied to solve the system model. However, it is still unknown how the multi-rate schemes will affect the numerical stability of the solver.

- As a simulation model of practical MEA system, it is always desirable that the simulation results can be validated by experiments so that its accuracy can be continually improved by experimental feedbacks. It is also desirable that the simulation model not only be able to reflect the system behavior under known test scenarios, but also can be used for some advanced functions such as fault prediction and prevention.

- As the size of MEA power system keeps growing, the hardware resource utilization for MEA simulation model will increase accordingly. Hardware implementation on FPGA is good choice but other appealing options have also emerged, such as the graphic processing unit (GPU). Different computation architecture requires different programing fashion and needs test results validation. Continuing work can be conducted on comparison and validation of MEA model implemented on different computation architectures.

Bibliography

[1] P. Wheeler and S. Bozhko, "The more electric aircraft: Technology and challenges," *IEEE Electrific. Mag.*, vol. 2, no. 4, pp. 6–12, Dec. 2014.

[2] A. Smith, T. Childs and R. Chen, "Study into electrically shaft driven air cycle machines," *in Proc. 1st Int. Conf. on Advances in Aerosp. Struc., Syst. & Tech.*, Croydon, London, 2018.

[3] B. Sarlioglu and C. T. Morris, "More electric aircraft: Review, challenges, and opportunities for commercial transport aircraft," *" IEEE Trans. Transp. Electrification,* vol. 1, no. 1, pp. 54–64, Jun. 2015.

[4] M. Sinnett, "787 No-Bleed Systems: Saving Fuel and Enhancing Operational Efficiencies," *Aeromagazine,* vol. 4, 2007.

[5] B. Šulc and J. A. Jan, "Non-linear modeling and control of hydraulic actuators," *Acta Polytechnica*, vol. 42, no. 3, pp. 41–47, 2002.

[6] R. Galluzzi, N. Amati, and A. Tonoli, "Modeling and characterization of rotary electro-hydrostatic actuators," *Journal of Vibration and Acoustics*, vol. 138, no. 1. Feb. 2016.

[7] R. Kang, Z. Jiao, S. Wu, Y. Shang, and J. Mare, "The nonlinear accuracy model of electro-hydrostatic actuator," *in Proc. 2008 IEEE Conf. Robotics, Automation & Mechatronics*, Chengdu, China, 2008, pp. 107–111.

[8] W. Lee, S. Li, D. Han, B. Sarlioglu, T. A. Minav, and M. Pietola, "A review of integrated motor drive and wide-bandgap power electronics for high-performance electro-hydrostatic actuators," *IEEE Trans. Transp. Electrific.*, vol. 4, no. 3, pp. 684–693, Sep. 2018.

[9] S. Habibi and A. Goldenberg, "Design of a new high-performance electrohydraulic actuator," *IEEE/ASME Trans. Mechatronics*, vol. 5, no. 2, pp. 158–164, June 2000.

[10] D. Belloli, F. Previdi, S. M. Savaresi, A. Cologni, and M. Zappella, "Modeling and identification of an electro-hydrostatic actuator," *in Proc. 5th IFAC Symposium on Mechatronic Sys.*, Cambridge, MA, 2010, pp. 620-625.

[11] A. Garcia, I. Cusido, J.A. Rosero, J.A. Ortega, and L. Romeral, "Reliable electro-mechanical actuators in aircraft," *IEEE Aerosp. Electron. Syst. Mag.*, vol. 23, no. 8, pp. 19–25, Aug. 2008.

[12] S. Zhu, T. Cox, Z. Xu, C. Gerada, and C. Li, "Design considerations of fault-tolerant electromechanical actuator systems for more electric aircraft (MEA)," *in Proc. 2018 IEEE Energy Conversion Congress and Exposition (ECCE),* Portland, OR, USA, 2018, pp. 4607–4613.

[13] M. Todeschi, "Airbus-EMAs for flight controls actuation system–An important step achieved in 2011," *SAE, Tech. Paper*, Warrendale, PA, USA, 2011-01-2732, 2011.

[14] L. Romeral, J.A. Rosero, A. G. Espinosa, J. Cusido, and J.A. Ortega, "Electrical monitoring for fault detection in an EMA," *IEEE Aerosp. Electron. Syst. Mag.*, vol. 25, no. 3, pp. 4–9, May 2010.

[15] X. Guillaud et al., "Applications of real-time simulation technologies in power and energy systems," *IEEE Power Energy Technol. Syst. J.,* vol. 2, no. 3, pp. 103–115, Sep. 2015.

[16] M. D. O. Faruque et al., "Real-time simulation technologies for power systems design, testing, and analysis," *IEEE Power Energy Technol. Syst. J.,* vol. 2, no. 2, pp. 63–73, Jun. 2015.

[17] H. W. Dommel, "Digital computer solution of electromagnetic transients in single-and multiphase networks," *IEEE Trans. App. Syst.,* vol. PAS-88, no. 4, pp. 388-399, Apr. 1969.

[18] C-W. Ho, A. Ruehli and P. Brennan, "The modified nodal approach to network analysis," *IEEE Trans. Circuits Syst.,* vol. 22, no. 6, pp. 504-509, Jun 1975.

[19] K. Strunz and E. Carlson "Nested fast and simultaneous solution for time-domain simulation of integrative power-electric and electronic systems," *IEEE Trans. Power Delivery,* vol. 22, no. 1, pp. 277-287, Jan. 2007.

[20] M. A. Elizondo, F. K. Tuffner, and K. P. Schneider, "Simulation of inrush dynamics for unbalanced distribution systems using dynamic-phasor models," *IEEE Trans. Power Syst.,* vol. 32, no. 1, pp. 633-642, Jan. 2016.

[21] L. O. Chua and P. M. Lin, *Computer Aided Analysis of Electronic Circuits: Algorithms and Computational Techniques,* Englewood Cliffs, CA: Prentice-Hall, 1975.

[22] L. A. Grégoire, H. F. Blanchette, J. Bélanger and K. Al-Haddad, "A stability and accuracy validation method for multirate digital simulation," *IEEE Trans. Ind. Inf.,* vol. 13, no. 2, pp. 512-519, April 2017.

[23] L. A. Dessaint, K. Al-Haddad, H. Le-Huy, G. Sybille, and P. Brunelle, "A power system simulation tool based on Simulink," *IEEE Trans. Ind. Electron.,* vol. 46, pp. 1252-1254, Dec. 1999.

[24] A. Davoudi, J. Jatskevich, and T. De Rybel, "Numerical state-space average-value modeling of PWM DC-DC converters operating in DCM and CCM," *IEEE Trans. Power Electron.,* vol. 21, no. 4, pp. 1003-1012, Jul. 2006.

[25] J. A. R., Macias, A. G Exposito, and A. B Soler, "A comparison of techniques for state-space transient analysis of transmission lines," *IEEE Trans. on Power Delivery,* vol. 20, Part 1, pp. 894 – 903, April 2005.

[26] H. F. Blanchette, T. Ould-Bachir, and J. P. David, "A state-space modeling approach for the FPGA-based real-time simulation of high switching frequency power converters," *IEEE Trans. Ind. Electron.,* vol. 59, no. 12, pp. 4555–4567, Dec. 2012.

[27] *EMTDC User's Guide Version 4.2.0.,* Manitoba HVDC Research Center, Winnipeg, Canada, 2005.

[28] *Simulink User's Guide (R2016a),* The MathWorks, Inc., Natick, MA, US, 2016.

[29] J. E. Schutt-Aine, "Latency insertion method (LIM) for the fast transient simulation of large networks," *IEEE Trans. Circuits Syst. I: Fundam. Theory Appl.,* vol. 48, no. 1, pp. 81-89, Jan. 2001.

[30] A. Benigni, A. Monti and R. A. Dougal, "Latency-based approach to the simulation of large power electronics systems," *IEEE Trans. Power Electron.,* vol. 29, no. 6, pp. 3201-3213, June 2014.

[31] S. N. Lalgudi, M. Swaminathan, and Y. Kretchmer, "On-chip power-grid simulation using latency insertion method," *IEEE Trans. Circuits Syst. I, Reg. Papers,* vol. 55, no. 3, pp. 914–931, Apr. 2008.

[32] S. Y. R. Hui, K. K. Fung and C. Christopoulos, "Decoupled simulation of multi-stage power electronic systems using transmission-line links," in *Rec. IEEE Power Electronics Specialists Conf.,* Toledo, Spain, 1992, pp. 1324-1330.

[33] S. Y. R. Hui and K. K. Fung, "Fast decoupled simulation of large power electronic systems using new two-port companion link models," *IEEE Trans. Power Electron.,* vol. 12, no. 3, pp. 462–473, May 1997.

[34] U. N. Gnanarathna, A. M. Gole and R. P. Jayasinghe, "Efficient modeling of modular multilevel HVDC converters (MMC) on electromagnetic transient simulation programs," *IEEE Trans. Power Delivery,* vol. 26, no. 1, pp. 316-324, Jan. 2011.

[35] H. W. Dommel, *Electro-Magnetic Transients Program (EMTP) Theory Book,* Vancouver, BC, Canada: Microtran Power System Analysis Corporation, 1996.

[36] T. Zhao, Q. Li and J. Qian, "Investigation on digital algorithm for on-line monitoring and diagnostics of metal oxide surge arrester based on an accurate model," *IEEE Trans. Power Delivery,* vol. 20, no. 2, pp. 751-756, April 2005.

[37] M. Armstrong, J. R. Marti, L. R. Linares and P. Kundur, "Multilevel MATE for efficient simultaneous solution of control systems and nonlinearities in the OVNI simulator," *IEEE Trans. Power Syst.,* vol. 21, no. 3, pp. 1250-1259, Aug. 2006.

[38] W. Wang, Z. Shen and V. Dinavahi, "Physics-Based Device-Level Power Electronic Circuit Hardware Emulation on FPGA," *IEEE Trans. Ind. Inform.,* vol. 10, no. 4, pp. 2166-2179, Nov. 2014.

[39] T. Noda and T. Kikuma, "A robust and efficient iterative scheme for the EMT simulations of nonlinear circuits," *IEEE Trans. Power Delivery,* vol. 26, no. 2, pp. 1030-1038, April 2011.

[40] Y. Chen and V. Dinavahi, "An iterative real-time nonlinear electromagnetic transient solver on FPGA," *IEEE Trans. Ind. Electron.,* vol. 58, no. 6, pp. 2547-2555, June 2011.

[41] F. Bizzarri, A. Brambilla, G. S. Gajani and S. Banerjee, "Simulation of real world circuits: extending conventional analysis methods to circuits described by heterogeneous languages," *IEEE Circuits Syst. Mag.,* vol. 14, no. 4, pp. 51-70, Fourthquarter 2014.

[42] A. Myaing and V. Dinavahi, "FPGA-based real-time emulation of power electronic systems with detailed representation of device characteristics," *IEEE Trans. Ind. Electron.,* vol. 58, no. 1, pp. 358-368, Jan. 2011.

[43] A. M. Gole, R. W. Menzies, H. M. Turanli and D. A. Woodford, "Improved interfacing of electrical machine models to electromagnetic transients programs," *IEEE Trans. Power App. Syst.,* vol. PAS-103, no. 9, pp. 2446-2451, Sept. 1984.

[44] W. Eberle, Z. Zhang, Y. F. Liu and P. C. Sen, "A practical switching loss model for buck voltage regulators," *IEEE Trans. Ind. Electron.,* vol. 24, no. 3, pp. 700-713, March 2009.

[45] L. Qu and P. L. Chapman, "Extraction of low-order non-linear inductor models from a high-order physics-based representation," *IEEE Trans. Ind. Electron.,* vol. 21, no. 3, pp. 813-817, May 2006.

[46] K. Strunz and E. Carlson, "Nested fast and simultaneous solution for time-domain simulation of integrative power-electric and electronic systems," *IEEE Trans. Power Delivery,* vol. 22, no. 1, pp. 277-287, Jan. 2007.

[47] F. Vasca, L. Iannelli, M. K. Camlibel and R. Frasca, "A new perspective for modeling power electronics converters: complementarity framework," *IEEE Trans. Ind. Electron.,* vol. 24, no. 2, pp. 456-468, Feb. 2009.

[48] Z. Shen and V. Dinavahi, "Real-time device-level transient electrothermal model for modular multilevel converter on FPGA," *IEEE Trans. Power Electron.,* vol. 31, no. 9, pp. 6155-6168, Sept. 2016.

[49] B. Gustavsen, "Wideband transformer modeling including core nonlinear effects," *IEEE Trans. Power Delivery,* vol. 31, no. 1, pp. 219-227, Feb. 2016.

[50] S. Y. R. Hui and S. Morrall, "Generalized associated discrete circuit model for switching devices," in *IEE Proc.: Sci. Meas. Technol.,* vol. 141, no. 1, pp. 57-64, Jan. 1994.

[51] Q. Mu, J. Liang, X. Zhou, Y. Li and X. Zhang, "Improved ADC model of voltage-source converters in DC grids," *IEEE Trans. Power Electron.*, vol. 29, no. 11, pp. 5738-5748, Nov. 2014.

[52] P. Pejović and D. Maksimović, "A new algorithm for simulation of power electronic systems using piecewise-linear device models," *IEEE Trans. Power Electron.*, vol. 10, no. 3, pp. 340-348, May, 1995.

[53] C. Wong, "EMTP modeling of IGBT dynamic performance for power dissipation estimation," *IEEE Trans. Ind. Appl.*, vol. 33, no. 1, pp. 64-71, Jan./Feb. 1997.

[54] W. W. Hager, "Updating the inverse of a matrix," *SIAM Review,* vol. 31, no. 2, pp. 221-239, 1989.

[55] B. Li, R. Yang, D. Xu, G. Wang, W. Wang and D. Xu, "Analysis of the phase-shifted carrier modulation for modular multilevel converters," *IEEE Trans. Power Electron.*, vol. 30, no. 1, pp. 297-310, Jan. 2015.

[56] D. Shu, V. Dinavahi, X. Xie and Q. Jiang, "Shifted frequency modeling of hybrid modular multilevel converters for simulation of MTDC grid," *IEEE Trans. Power Delivery,* vol. PP, no. 99, pp. 1-1, Sep. 2017.

[57] M. Hagiwara and H. Akagi, "Control and experiment of pulsewidth-modulated modular multilevel converters," *IEEE Trans. Power Electron.*, vol. 24, no. 7, pp. 1737-1746, July 2009.

[58] Z. Huang, K. Sun and Y. Mei, "A specific analysis model of three-level NPC inverter fed adjustable speed drive system with high accuracy," in *Proc. 17th IEEE Int. Conf. Electrical Machines and Systems (ICEMS),* Hangzhou, China, 2014, pp. 914-919.

[59] S. Busquets Monge, S. Somavilla, J. Bordonau and D. Boroyevich, "Capacitor voltage balance for the neutral-point-clamped converter using the virtual space vector concept with optimized spectral performance," *IEEE Trans. Power Electron.*, vol. 22, no. 4, pp. 1128-1135, July 2007.

[60] *Saber User Guide, Version V-2004.06-SP1,* Synopsys, Inc., Mountain View, CA, USA, 2004.

[61] R. B. Bapat, *Graphs and Matrices,* 2nd ed., London, UK: Springer-Verlag London, 2014.

[62] W. H. Hayt Jr., J. E. Kemmerly, and S. M. Durbin, *Engineering Circuit Analysis,* 6th ed., Boston, Mass. : McGraw-Hill, 2002.

[63] E. S. Kuh and R. A. Rohrer, "The state-variable approach to networkanalysis," *Proc. IEEE,* vol. 53, pp. 672–686, 1965.

[64] W. K. Durfee, M. B. Wall, D. Rowell, and F. K. Abbott, "Interactive software for dynamic system modeling using linear graphic," *IEEE Control Syst. Mag.,* vol. 11, no. 4, pp. 60–66, June 1991.

[65] T. Martínez-Marín, "State-space formulation for circuit analysis," *IEEE Trans. Educ.,* vol. 53, no. 3, pp. 497–503, Aug. 2010.

[66] J. Sun and L. Xing, "Parameterization of three-phase electric machine models for EMI simulation," *IEEE Trans. Power Electron.*, vol. 29, no. 1, pp. 36–41, Jan. 2014.

[67] A. Subramanian and U. Govindarajan, "Analysis and mitigation of EMI in DC-DC converters using QR interaction," *IET Circuits Devices Syst.*, vol. 11, no. 4, pp. 371–380, Jan. 2017.

[68] Z. Duan, D. Zhang, T. Fan, and X. Wen, "Prediction of conducted EMI in three phase inverters by simulation method," in *Proc. IEEE Transp. Electrific. Conf. & Expo, Asia-Pacific*, Harbin, China, 2017.

[69] J. Lai, X. Huang, E. Pepa, S. Chen, and T. W. Nehl, "Inverter EMI modeling and simulation methodologies," *IEEE Trans. Ind. Electron.*, vol. 53, no. 3, pp. 736–744, June 2006.

[70] R. S. Esfandiari, *Numerical Methods for Engineers and Scientists Using MATLAB®,* Boca Raton, FL: CRC Press, 2013.

[71] P. Maffezzoni, "A versatile time-domain approach to simulate oscillators in RF circuits," *IEEE Trans. Circuits Sys. I, Reg. Papers*, vol. 56, no. 3, pp. 594–603, Mar. 2009.

[72] N. Watson and J. Arrillaga, *Power Systems Electromagnetic Transients Simulation,* Milton Keynes, UK: Lighting Source UK Ltd, 2007.

[73] E. Fehlberg, "Low-order classical Runge-Kutta formulas with step size control and their application to some heat transfer problems," *National Aeronautics and Space Administration Technical Report R-315*,1969.

[74] R. Biswas, *Parallel Computational Fluid Dynamics: Recent Advances and Future Directions,* Lancaster, PA: DEStech Publications, Inc., 2009.

[75] J. D. Skufca, "Analysis still matters: a surprising instance of failure of Runge-Kutta-Felberg ODE solvers," *SIAM REVIEW,* vol. 46, no. 4, pp. 729–737, 2004.

[76] M. L. Heldwein, L. Dalessandro, and J. K. Kolar, "The three-phase common-mode inductor: modeling and design issues," *IEEE Trans. Ind. Electron.*, vol. 58, no. 8, pp. 3264–3274, Aug. 2011.

[77] W. Tan, C. Cuellar, X. Margueron, and N. Idir, "A high frequency equivalent circuit and parameter extraction procedure for common mode choke in the EMI filter," *IEEE Trans. Power Electron.*, vol. 28, no. 3, pp. 1157–1166, Mar. 2013.

[78] I. F. Kovačević, T. Friedli, A. M. Muesing, and J. K. Kolar, "3-D electromagnetic modeling of EMI input filters," *IEEE Trans. Ind. Electron.*, vol. 61, no. 1, pp. 231–242, Jan. 2014.

[79] M. Illia, and G. Griepentrog, "Finite element method based electromagnetic modeling of three-phase EMI filters," in *Proc.* 2016 IEEE 2nd Annual Southern Power Electron. Conf. (SPEC), Auckland, New Zealand, 2016, pp. 1–6.

[80] Z. Yu, J. He, R. Zeng, H. Rao, X, Li, Q. Wang, B. Zhang, and S. Chen, "Simulation analysis on conducted EMD caused by valves in ±800 kV UHVDC converter station," *IEEE Trans. Electromagn. Compat.*, vol. 51, no. 2, pp. 236–244, May 2009.

[81] B. Wunsch, I. Stevanović, and S. Skibin, "Length-scalable multiconductor aable modeling for EMI simulations in power electronics," *IEEE Trans. Power Electron.*, vol. 32, no. 3, pp. 1908–1916, Mar. 2017.

[82] W. H. Press, S. A. Teukolsky, W. T. Vetterling, and B. P. Flannery, *Numerical Recipes: The Art of Scientific Computing,* 3rd ed., Cambridge UK: Cambridge University Press, 2007.

[83] S. T. Jensen and G. P. H. Styan, "Some comments and a bibliography on the laguerre-samuelson inequality with extensions and applications in statistics and matrix theory," *Analytic and Geometric Inequalities and Applications.* pp. 151–181, 1999.

[84] D. L. Skaar, "Using the superposition method to formulate the state variable matrix for linear networks," *IEEE Trans. Educ.*, vol. 44, no. 4, pp. 311–314, Nov. 2001.

[85] D. Kalman, "A matrix proof of newton's identities," *Mathematics Magazine*, vol. 73, no. 4, pp. 313–315, Oct. 2000.

[86] H. Wolkowicz and G. P. H. Styan, "Bounds for eigenvalues using traces," Linear Algebra Appl., no. 29, pp. 471–506, Feb. 1980.

[87] H. Akagi, H. Hasegawa, and T. Doumoto, "Design and performance of a passive EMI filter for use with a voltage-source PWM inverter having sinusoidal output voltage and zero common-mode voltage," *IEEE Trans. Power Electron.*, vol. 19, no. 4, pp. 1069–1076, Jul. 2004.

[88] The Mathworks, "Choose a Solver," 2019. [online]. Available: https://www.mathworks.com/help/simulink/ug/types-of-solvers.html

[89] J. E. McNamara, "Electrically driven environmental control system," *IEEE Trans. Aerosp. Electron. Syst.*, vol. AES-20, no. 3, pp. 257–260, May 1984.

[90] R. V. Díaz, "Analysis of an electric environmental control system to reduce the energy consumption of fixed-wing and rotary-wing aircraft," M.S. thesis, Sch. of Eng., Cranfield Univ., Cranfield, UK, 2011. Accessed on: Oct. 14, 2019. [Online]. Available: https://dspace.lib.cranfield.ac.uk/handle/1826/7422

[91] H. Devadurgam, S. Rajagopal, and R. C. Munjulury, "Analytical design and estimation of conventional and electrical aircraft environmental control systems," *engrXiv*, vol. 11, Mar. 2019.

[92] G. Carsten and C. Udo, "Control of an electro-hydrostatic actuation system for the nose landing gear of an all electric aircraft," *in Proc. Recent Advances in Aerosp. Actuation Sys. & Compon. 2004*, Toulouse, France, 2004.

[93] A. Trentin, P. Zanchetta, P. Wheeler, and J. Clare, "Power flow analysis in electro-mechanical actuators for civil aircraft," *IET Electric Power Appl.*, vol. 5, no. 1, pp. 48–58, Jan. 2011.

[94] M. Mazzoleni, Y. Maccarana, F. Previdi, G. Pispola, M. Nardi, F. Perni, and S. Toro, "Development of a reliable electro-mechanical actuator for primary control surfaces in small aircrafts," *in Proc. IEEE Int. Conf. Adv. Intell. Mechatronics (AIM)*, Munich, Germany, 2017, pp. 1142-1147.

[95] N. S. Nise, *Control Systems Engineering,* Hoboken, New Jersey: John Wiley & Sons, 2010.

[96] L. Wang, J. Jatskevich, V. Dinavahi, H. W. Dommel, J. A. Martinez, K. Strunz, M. Rioual, G. W. Chang, and R. Iravani, "Methods of interfacing rotating machine models in transient simulation programs," *IEEE Trans. Power Del.*, vol. 25, no. 2, pp. 891–903, April 2010.

[97] K. J. Åström and C. Canudas-de-Wit, "Revisiting the LuGre friction model," *IEEE Control Syst. Mag.*, vol. 28, no. 6, pp. 101–114, Dec. 2008.

[98] D. McLean, *Automatic Flight Control Systems*, Englewood Cliffs, New Jersey: Prentice Hall Inc., 1990.

[99] D. A. Caughey, Introduction to Aircraft Stability and Control, 2011. Accessed on: Oct. 14, 2019. [Online]. Available: https://courses.cit.cornell.edu/mae5070/Caughey_2011_04.pdf

[100] T. I. Fossen, "Mathematic Models for Control of Aircraft and Satellites," 3rd ed., Trondheim: Norwegian University of Science and Technology, 2013.

[101] G. D. Demetriades, H. Z. de la Parra, E. Andersson, and H. Olsson, "A real-time thermal model of a permanent-magnet synchronous motor," *IEEE Trans. Power Electron.*, vol. 25, no. 2, pp. 463–474, Feb. 2010.

[102] N. Arbab, W. Wang, C. Lin, J. Hearron, and B. Fahimi, "Thermal modeling and analysis of a double-stator switched reluctance motor," *IEEE Trans. Energy Convers.*, vol. 30, no. 3, pp. 1209–1217, Sept. 2015.

[103] O. Wallscheid and J. Böcker, "Global identification of a low-order lumped-parameter thermal network for permanent magnet synchronous motors," *IEEE Trans. Energy Convers.*, vol. 31, no. 1, pp. 354–365, March 2016.

[104] A. Boglietti, A. Cavagnino, D. Staton, M. Shanel, M. Mueller, and C. Mejuto, "Evolution and modern approaches for thermal analysis of electrical machines," *IEEE Trans. Ind. Electron.*, vol. 56, no. 3, pp. 871–882, March 2009.

[105] E. Ganev, "Selecting the best electric machines for electrical power-generation systems: High-performance solutions for aerospace More electric architectures," *IEEE Electrific. Mag.*, vol. 2, no. 4, pp. 13–22, Dec. 2014.

[106] P. C. Krause, O. Wasynczuk, and S. D. Sudhoff, *Analysis of Electric Machinery and Drive Systems,* Piscataway, N.J. : Wiley-IEEE Press, 2002.

[107] C. A. Eschenbach and C. R. Johnson, "Sign patterns that require real, nonreal or pure imaginary eigenvalues," *Linear and Multilinear Algebra*, vol. 29, pp. 299-311, 1991.

[108] H. Wielandt, "On the eigenvalues of $\mathbf{A} + \mathbf{B}$ and $\mathbf{AB}$," *Journal of Research of the National Bureau of Standards – B. Mathematical Sciences*, vol.77B, No. 1&2, pp. 61-63, Jan.-June, 1972.

[109] P. F. Zachlin and M. E. Hochstenbach, "On the numerical range of a matrix," *Linear and Multilinear Algebra*, vol. 56, no. 1-2, pp. 185-225.

[110] H. WoIkowicz and G. P. H. Styan, "Bounds for eigenvalues using traces," *Linear Algebra and Its Applications*, vol. 29, pp. 471-506, 1980.

[111] T. Yang, S. Bozhko, and G. Asher, "Functional modeling of symmetrical multipulse autotransformer rectifier units for aerospace applications," *IEEE Trans. Power Electron.,* vol. 30, no. 9, pp. 4704–4713, Sep. 2015.

[112] The Mathworks, "Simulating Discretized Electrical Systems," 2018. [online]. Available: https://www.mathworks.com/help/physmod/sps/powersys/ug/simulating-discretized-electrical-systems.html

[113] A. Pollok, "Modelling and control of aircraft environmental control systems," Ph.D. dissertation, Dept. of Elec. Infor. & Bioingegneria, Polytechnic Univ. Milan, Milan, Italy, 2017. Accessed on: Oct. 14, 2019. [Online]. Available: https://elib.dlr.de/119309/1/thesis.pdf

[114] J. W. Bennett, B. C. Mecrow, A. G. Jack, and D. J. Atkinson, "A prototype electrical actuator for aircraft flaps," *IEEE Trans. Ind. Appl.*, vol. 46, no. 3, pp. 915–921, May/June 2010

A

A.1 Parameters of the five-level MMC in chapter 2

Parameter	Value
No. of SMs per Arm	4
Rated DC-link Voltage	6 kV
Arm Inductance	3 mH
SM Capacitance	1900 μF
Carrier Frequency	2000 Hz
Reference Frequency	50 Hz
Load Inductance	6 mH
Load Resistance	30 Ω

A.2 Parameters of the three-level NPC and PMSM in chapter 2

Parameter		Value
NPC	Rated DC Bus Voltage	3 kV
	DC source resistor (R_{sc})	0.01 Ω
	DC Bus Capacitor (C_1, C_2)	10 mF
	Carrier Frequency	1800 Hz
PMSM	Rated MVA	3.65 MVA
	Rated Voltage (L-L)	4 kV
	Rated Frequency	60 Hz
	Stator Winding Resistance	0.011 p.u.
	Stator Leakage Reactance	0.064 p.u.
	d-axis Reactance (X_{d})	0.689 p.u.
	q-axis Reactance (X_1)	0.689 p.u.
	d-axis Damper Winding Resistance (R_{kd})	0.055 p.u.
	d-axis Damper Winding Reactance (X_{kd})	0.62 p.u.
	q-axis Damper Winding Resistance (R_{kq})	0.183 p.u.
	q-axis Damper Winding Reactance (X_{kq})	1.175 p.u.
	Magnetic Strength (R_{kq})	1.0 p.u.
	Inertia Constant (H)	1 s
	Friction Factor (B)	0.0005
	Load Torque (T_{L})	0.5 p.u.

B

B.1 Multi-Domain System Parameters in Chapter 5

Electrical part parameters: SG capacity: 250 kVA; AC bus voltage: 230 V; DC bus voltage: $\pm$270 V; Switching frequency of inverter: 12 kHz; PMSM rated power: 60 kW; PMSM rated voltage: 300 V.

Mechanical part parameters: Aircraft speed: 980 km/h; Aircraft altitude: 35 000 ft; Aircraft mass: 184 000 lbs.

Thermal part parameters: C_{SY}: 5.59$\times 10^3$ J/K; C_{SW}: 2.62$\times 10^3$ J/K; C_{ST}: 2.91$\times 10^3$ J/K; C_{PM}: 1.08$\times$ 10^4 J/K; $R_{\mathrm{SY,SW}}$: 0.289 K/W; $R_{\mathrm{SY,ST}}$: 0.013 K/W; $R_{\mathrm{SW,ST}}$: 0.019 K/W; $R_{\mathrm{C,SY,0}}$: 0.017 K/W; $R_{\mathrm{ST,PM,0}}$: 0.599 K/W; $R_{\mathrm{PMY,A,0}}$: 2.451 K/W; other parameters can be found in [103].